EUROPEAN ORGANISATION FOR NUCLEAR RESEARCH (CERN)
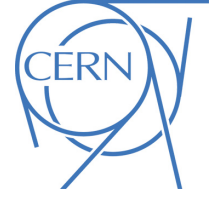
Measurements of $\pi^{\pm}$, $K^{\pm}$, p and $\bar{p}$ spectra in ^{40}Ar+^{45}Sc collisions at 13A to 150A GeV/c

The NA61/SHINE Collaboration

The NA61/SHINE experiment at the CERN Super Proton Synchrotron studies the onset of deconfinement in strongly interacting matter through a beam energy scan of particle production in collisions of nuclei of varied sizes. This paper presents results on inclusive double-differential spectra, transverse momentum and rapidity distributions and mean multiplicities of $\pi^{\pm}$, $K^{\pm}$, p and $\bar{p}$ produced in ^{40}Ar+^{45}Sc collisions at beam momenta of 13A, 19A, 30A, 40A, 75A and 150A GeV/c. The analysis uses the 10% most central collisions, where the observed forward energy defines centrality. The energy dependence of the $K^{\pm}/\pi^{\pm}$ ratios as well as of inverse slope parameters of the $K^{\pm}$ transverse mass distributions are placed in between those found in inelastic p+p and central Pb+Pb collisions. The results obtained here establish a system-size dependence of hadron production properties that so far cannot be explained either within statistical (SMES, HRG) or dynamical (EPOS, UrQMD, PHSD, SMASH) models.

Contents

The NA61/SHINE Collaboration

H. Adhikary [13], P. Adrich [15], K.K. Allison [26], N. Amin [5], E.V. Andronov [22], T. Antićić [3], I.-C. Arsene [12], M. Bajda [16], Y. Balkova [18], M. Baszczyk [17], D. Battaglia [25], A. Bazgir [13], S. Bhosale [14], M. Bielewicz [15], A. Blondel [4], M. Bogomilov [2], Y. Bondar [13], N. Bostan [25], A. Brandin [22], W. Bryliński [21], J. Brzychczyk [16], M. Buryakov [22], A.F. Camino [28], M. Ćirković [23], M. Csanád [8], J. Cybowska [21], T. Czopowicz [13], C. Dalmazzone [4], N. Davis [14], A. Dmitriev [22], P. von Doetinchem [27], W. Dominik [19], P. Dorosz [17], J. Dumarchez [4], R. Engel [5], G.A. Feofilov [22], L. Fields [25], Z. Fodor [7,20], M. Friend [9], M. Gaździcki [13,6], O. Golosov [22], V. Golovatyuk [22], M. Golubeva [22], K. Grebieszkow [21], F. Guber [22], S.N. Igolkin [22], S. Ilieva [2], A. Ivashkin [22], A. Izvestnyy [22], K. Kadija [3], N. Kargin [22], N. Karpushkin [22], E. Kashirin [22], M. Kiełbowicz [14], V.A. Kireyeu [22], H. Kitagawa [10], R. Kolesnikov [22], D. Kolev [2], Y. Koshio [10], V.N. Kovalenko [22], S. Kowalski [18], B. Kozłowski [21], A. Krasnoperov [22], W. Kucewicz [17], M. Kuchowicz [20], M. Kuich [19], A. Kurepin [22], A. László [7], M. Lewicki [20], G. Lykasov [22], V.V. Lyubushkin [22], M. Maćkowiak-Pawłowska [21], Z. Majka [16], A. Makhnev [22], B. Maksiak [15], A.I. Malakhov [22], A. Marcinek [14], A.D. Marino [26], H.-J. Mathes [5], T. Matulewicz [19], V. Matveev [22], G.L. Melkumov [22], A. Merzlaya [12], Ł. Mik [17], A. Morawiec [16], S. Morozov [22], Y. Nagai [8], T. Nakadaira [9], M. Naskręt [20], S. Nishimori [9], V. Ozvenchuk [14], O. Panova [13], V. Paolone [28], O. Petukhov [22], I. Pidhurskyi [13,6], R. Płaneta [16], P. Podlaski [19], B.A. Popov [22,4], B. Pórfy [7,8], M. Posiadała-Zezula [19], D.S. Prokhorova [22], D. Pszczel [15], S. Puławski [18], J. Puzović [23†], R. Renfordt [18], L. Ren [26], V.Z. Reyna Ortiz [13], D. Röhrich [11], E. Rondio [15], M. Roth [5], Ł. Rozpłochowski [14], B.T. Rumberger [26], M. Rumyantsev [22], A. Rustamov [1,6], M. Rybczynski [13], A. Rybicki [14], K. Sakashita [9], K. Schmidt [18], A.Yu. Seryakov [22], P. Seyboth [13], U.A. Shah [13], Y. Shiraishi [10], A. Shukla [27], M. Słodkowski [21], P. Staszel [16], G. Stefanek [13], J. Stepaniak [15], M. Strikhanov [22], H. Ströbele [6], T. Šuša [3], L. Swiderski [15], J. Szewiński [15], R. Szukiewicz [20], A. Taranenko [22], A. Tefelska [21], D. Tefelski [21], V. Tereshchenko [22], A. Toia [6], R. Tsenov [2], L. Turko [20], T.S. Tveter [12], M. Unger [5], M. Urbaniak [18], F.F. Valiev [22], D. Veberič [5], V.V. Vechernin [22], V. Volkov [22], A. Wickremasinghe [24], K. Wójcik [18], O. Wyszyński [13], A. Zaitsev [22], E.D. Zimmerman [26], A. Zviagina [22], and R. Zwaska [24]

---

† *deceased*

1 National Nuclear Research Center, Baku, Azerbaijan
2 Faculty of Physics, University of Sofia, Sofia, Bulgaria
3 Ruđer Bošković Institute, Zagreb, Croatia
4 LPNHE, University of Paris VI and VII, Paris, France
5 Karlsruhe Institute of Technology, Karlsruhe, Germany
6 University of Frankfurt, Frankfurt, Germany
7 Wigner Research Centre for Physics, Budapest, Hungary
8 Eötvös Loránd University, Budapest, Hungary
9 Institute for Particle and Nuclear Studies, Tsukuba, Japan
10 Okayama University, Japan
11 University of Bergen, Bergen, Norway
12 University of Oslo, Oslo, Norway
13 Jan Kochanowski University, Kielce, Poland
14 Institute of Nuclear Physics, Polish Academy of Sciences, Cracow, Poland
15 National Centre for Nuclear Research, Warsaw, Poland
16 Jagiellonian University, Cracow, Poland
17 AGH - University of Science and Technology, Cracow, Poland
18 University of Silesia, Katowice, Poland

[19] University of Warsaw, Warsaw, Poland

[20] University of Wrocław, Wrocław, Poland

[21] Warsaw University of Technology, Warsaw, Poland

[22] Affiliated with an institution covered by a cooperation agreement with CERN

[23] University of Belgrade, Belgrade, Serbia

[24] Fermilab, Batavia, USA

[25] University of Notre Dame, Notre Dame, USA

[26] University of Colorado, Boulder, USA

[27] University of Hawaii at Manoa, Honolulu, USA

[28] University of Pittsburgh, Pittsburgh, USA

1 Introduction

This paper presents experimental results on inclusive spectra and mean multiplicities of $\pi^{\pm}, K^{\pm}, p$ and $\bar{p}$ produced in the 10% most central ^{40}Ar+^{45}Sc collisions at beam momenta of $13A$, $19A$, $30A$, $40A$, $75A$, and $150A\,\mathrm{GeV}/c$ ($\sqrt{s_{NN}}$ = 5.12, 6.12, 7.62, 8.77, 11.9 and 16.8 GeV). These studies form a part of the strong interactions program of NA61/SHINE [1] at the CERN SPS investigating the properties of the onset of deconfinement and searching for the possible existence of a critical point. The program is mainly motivated by the observed rapid changes in hadron production properties in central Pb+Pb collisions at about $30A\,\mathrm{GeV}/c$ by the NA49 experiment [2, 3]. These findings were interpreted as the onset of deconfinement; they were confirmed by the RHIC beam energy program [4] and their interpretation is supported by the LHC results (see Ref. [5] and references therein).

The goals of the NA61/SHINE strong interaction program are pursued experimentally by a two-dimensional scan in collision energy and size of colliding nuclei. This allows us to systematically explore the phase diagram of strongly interacting matter [1]. In particular, the analysis of the existing data within the framework of statistical models suggests that by increasing collision energy one increases the temperature and decreases the baryon chemical potential of the fireball of strongly interacting matter at kinetic freeze-out [6], whereas by increasing the nuclear mass of the colliding nuclei the temperature decreases [6–9].

Within this program NA61/SHINE recorded data on $p+p$, Be+Be, Ar+Sc, Xe+La, and Pb+Pb collisions during 2009-2018 running. Further high-statistics measurements of Pb+Pb collisions with an upgraded detector started in 2022 [10, 11]. Comprehensive results on particle spectra and multiplicities have already been published for $p+p$ interactions [12–14] and Be+Be collisions [15, 16] at $19A$-$150A\,\mathrm{GeV}/c$ (20-158 GeV/c for $p+p$). For Ar+Sc collisions, only results on π^- production were published up to now [17].

Ar+Sc collisions became crucial for the NA61/SHINE scan program. As the results obtained for the Be+Be system closely resemble inelastic $p+p$ interactions, the collisions of Ar+Sc are the lightest of the studied systems for which a significant increase in the K^+/π^+ ratio was observed. The properties of measured spectra and multiplicities indicate that the Ar+Sc system is on a boundary between light ($p+p$, Be+Be) and heavy (Pb+Pb) systems. The system size dependence established with new Ar+Sc measurements can be understood within neither statistical models [18, 19], nor dynamical ones [20, 21].

The paper is organized as follows: after this introduction, the experiment is briefly presented in Sec. 2. The analysis procedure, as well as statistical and systematic uncertainties, are discussed in Sec. 3. Section 4

presents experimental results and compares them with measurements of NA61/SHINE in inelastic p+p interactions [12–14] and central Be+Be [15, 16] collisions, as well as NA49's results on Pb+Pb, C+C and Si+Si reactions [2, 3]. Section 5 discusses model predictions. A summary in Section 6 closes the paper.

The following variables and definitions are used in this paper. The particle rapidity y is calculated in the collision center of mass system (cms), $y = 0.5 \cdot \ln\left[(E + p_L c)/(E - p_L c)\right]$, assuming proton mass, where E and p_L are the particle energy and longitudinal momentum, respectively. The transverse component of the momentum is denoted as p_T and the transverse mass m_T is defined as $m_T = \sqrt{m^2 + (cp_T)^2}$ where m is the particle mass in GeV. The momentum in the laboratory frame is denoted p and the collision energy per nucleon pair in the center of mass by $\sqrt{s_{NN}}$.

The Ar+Sc collisions are selected by requiring a low value of the forward energy – the energy emitted into the region populated by projectile spectators. These collisions are referred to as *central* collisions and a selection of collisions based on the forward energy is called a *centrality selection*. The term *central* is written in italics throughout this paper to denote the specific event selection procedure based on measurements of the forward energy.

2 Experimental setup

The NA61/SHINE experiment is a multi-purpose facility designed to measure particle production in nucleus-nucleus, hadron-nucleus and p+p interactions [22]. The detector is situated at the CERN Super Proton Synchrotron (SPS) in the H2 beamline of the North experimental area. A schematic diagram of the setup is shown in Fig. 1. The main components of the particle detection system used in the 2015
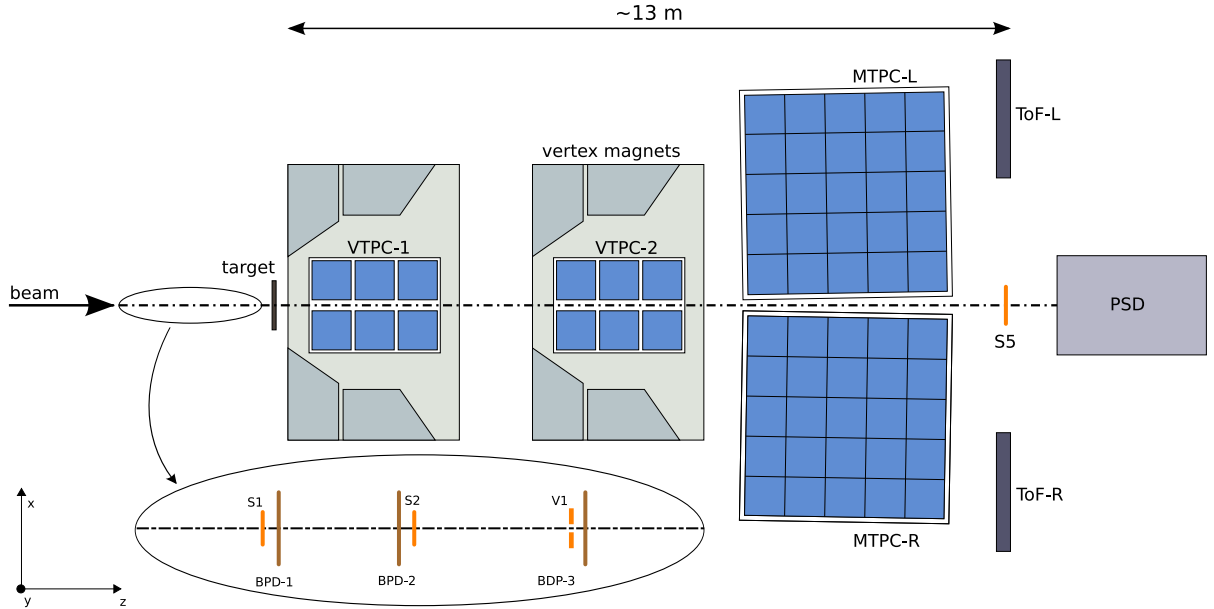

Figure 1: The schematic layout of the NA61/SHINE experiment at the CERN SPS [22] showing the components used for the Ar+Sc energy scan. The beam instrumentation is sketched in the inset. Alignment of the chosen coordinate system as shown in the figure. The nominal beam direction is along the z-axis. The magnetic field bends charged particle trajectories in the *x-z* (horizontal) plane. The drift direction in the TPCs is along the y (vertical) axis.

Ar+Sc data-taking campaign are four large-volume Time Projection Chambers (TPC). Two of them, called Vertex TPCs (VTPC), are located downstream of the target inside superconducting magnets with a maximum combined bending power of 9 Tm. The magnetic field was scaled down in proportion to the beam momentum in order to obtain similar $y - p_T$ acceptance at all beam momenta. The main TPCs (MTPC) and two walls of pixel Time-of-Flight (ToF-L/R) detectors are placed symmetrically on either side of the beamline downstream of the magnets. The TPCs are filled with $Ar:CO_2$ gas mixtures in proportions 90:10 for the VTPCs and 95:5 for the MTPCs. The Projectile Spectator Detector (PSD) is positioned 20.5 m (16.7 m) downstream of the MTPCs at beam momenta of 75A and 150A GeV/c (13A, 19A, 30A, 40A GeV/c), centered in the transverse plane on the deflected position of the beam. A degrader in form of a 5 cm diameter brass cylinder was placed in front of the center of the PSD in order to reduce electronic saturation effects and shower leakage from the downstream side. The length of the cylinder was 10 cm except the 19A GeV/c measurements, when the length was 5 cm. No degrader was used at 13A GeV/c.

Primary beams of fully ionized ^{40}Ar nuclei were extracted from the SPS accelerator at beam momenta of 13A, 19A, 30A, 40A, 75A and 150A GeV/c. Two scintillation counters, S1 and S2, provide beam trigger definition, together with a veto counter V1 with a 1 cm diameter hole, which defines the beam before the target. The S1 counter also provides the timing reference (start time for all counters). Beam particles are selected by the trigger system requiring the coincidence $S1 \wedge S2 \wedge \overline{V1}$. Individual beam particles are precisely measured by the three Beam Position Detectors (BPDs) placed upstream of the target [22]. Collimators in the beam line were adjusted to obtain beam rates of the order of 10^4/s during the 10.4 s spill within a 32.4 s accelerator super cycle.

The target was a stack of six Sc plates of 1 mm thickness and 2 x 2 cm^2 area placed 75 cm upstream of VTPC-1. Mass concentrations of impurities were measured at 0.3 % resulting in an estimated increase of the produced pion multiplicity by less than 0.2 % due to the small admixture of heavier elements [23]. No correction was applied for this negligible contamination. Data were taken with target inserted (93%) and target removed (7%).

Interactions in the target are selected with the trigger system by requiring an incoming Ar ion and a signal below that of beam ions from S5, a small 2 cm diameter scintillation counter placed on the beam trajectory behind the MTPCs. This minimum bias trigger selects inelastic collisions of the beam ion with the target and with matter between the target and S5. In addition, central collisions were selected by requiring an energy signal below a threshold set on the summed signal from the 16 central modules of the PSD, which measure mainly the energy of projectile spectators.. The cut was set to retain only the event triggers with roughly 30% smallest energies in the PSD, which was studied quantitatively in offline analysis. The central event trigger condition thus was $S1 \wedge S2 \wedge \overline{V1} \wedge \overline{S5} \wedge \overline{PSD}$. The statistics of recorded events are summarized in Table 1.

p_{beam} (GeV/c)	$\sqrt{s_{NN}}$ (GeV)	total recorded events	central trigger events (good events only)	0-10% most central after cuts
13A	5.12	$3.9 \cdot 10^6$	$2.95 \cdot 10^6$	$5.22 \cdot 10^5$
19A	6.12	$4.2 \cdot 10^6$	$2.97 \cdot 10^6$	$5.35 \cdot 10^5$
30A	7.62	$5.2 \cdot 10^6$	$4.09 \cdot 10^6$	$9.14 \cdot 10^5$
40A	8.77	$1.0 \cdot 10^7$	$6.36 \cdot 10^6$	$1.28 \cdot 10^6$
75A	11.94	$4.8 \cdot 10^6$	$3.08 \cdot 10^6$	$1.14 \cdot 10^6$
150A	16.83	$3.7 \cdot 10^6$	$1.54 \cdot 10^6$	$5.56 \cdot 10^5$

Table 1: Basic beam properties and the number of events recorded and used in the analysis of 10% most *central* Ar+Sc interactions. Event selection criteria will be discussed in Sec. 3.

3 Analysis procedure

This section starts with a brief overview of the data analysis procedure and the corrections applied to the experimental results. It also defines to which species of particles the final results correspond. A description of the detector calibration and the track and vertex reconstruction procedures can be found in Ref. [12].

The analysis procedure consists of the following steps:

(i) application of event and track selection criteria,

(ii) determination of raw spectra of identified charged hadrons using the selected events and tracks,

(iii) evaluation of corrections to the raw spectra based on experimental data and simulations,

(iv) calculation of the corrected spectra and mean multiplicities,

(v) calculation of statistical and systematic uncertainties.

Corrections for the following biases were evaluated:

(a) contribution from off-target interactions,

(b) losses of in-target interactions due to the event selection criteria,

(c) geometric acceptance,

(d) reconstruction and detector inefficiencies,

(e) losses of tracks due to track selection criteria,

(f) contribution of particles other than *primary* (see below) charged particles produced in Ar+Sc collisions,

(g) losses of primary charged particles due to their decays and secondary interactions.

Correction (a) was found to be negligible ($\mathcal{O}(10^{-4})$) and was therefore not applied.

Corrections (b)-(g) were estimated by data and simulations. MC events were generated with the EPOS1.99 model (version CRMC 1.5.3) [24], passed through detector simulation employing the GEANT 3.21 package [25] and then reconstructed using standard procedures, exactly matching the ones used in the processing of experimental data. The selection of central events in the simulation was based on the number of projectile spectator nucleons available in the EPOS model.

The final results refer to particles produced in *central* Ar+Sc collisions by strong and electromagnetic processes. Such hadrons are referred to as *primary* hadrons. The definition of *central* collisions is given in Sec. 3.1.

3.1 *Central* collisions

A short description of the procedure for defining *central* collisions is given below. For more details, see Refs. [17, 26, 27].

The final results presented in this paper refer to the 10% of Ar+Sc collisions with the lowest value of the forward energy E_F (*central* collisions). The quantity E_F is defined as the sum of energies (measured in the laboratory reference frame) of all particles produced in Ar+Sc collisions via strong and electromagnetic processes in the forward momentum region defined by the acceptance map in Ref. [28]. The final results on *central* collisions, derived using this procedure, allow a precise comparison with model predictions without additional information about the NA61/SHINE setup and used magnetic field. Using this definition, the mean number of wounded nucleons $\langle W \rangle$ was calculated in the Wounded Nucleon Model (WNM) [29] implemented in EPOS [30].
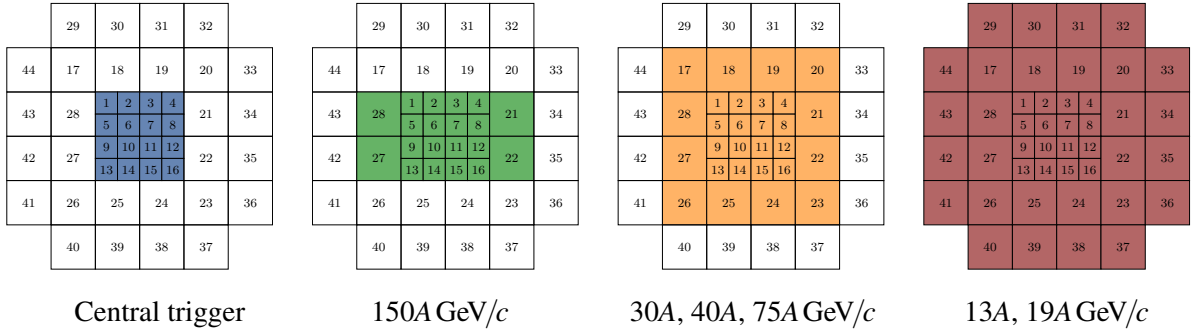

Figure 2: PSD modules used in the online and offline event selection. The central trigger is derived from the energy in the central 16 modules, while the set of modules used to determine the PSD energy E_{PSD} changes with beam momentum.

For data analysis, the event selection was based on the 10% of collisions with the lowest value of the energy E_{PSD} measured by a subset of PSD modules (see Fig. 2) optimized for the sensitivity to projectile spectators. The acceptance in the definition of the forward energy E_F corresponds closely to the acceptance of this subset of PSD modules at all energies [15, 17].

Online event selection by the central hardware trigger used a threshold on the sum of electronic signals from the 16 central modules of the PSD set to accept approx. 30% of the inelastic interactions. Measured

distributions of E_{PSD} for minimum-bias and central trigger selected events, calculated in the offline analysis, are shown in Fig. 3 at beam momenta of 19A and 150A GeV/c. The accepted region corresponding to the 10% of most *central* collisions is indicated by shading. The minimum-bias distribution was obtained using the data from the beam trigger with an offline selection of events by requiring an event vertex in the target region. A properly normalized spectrum for target-removed events was subtracted.
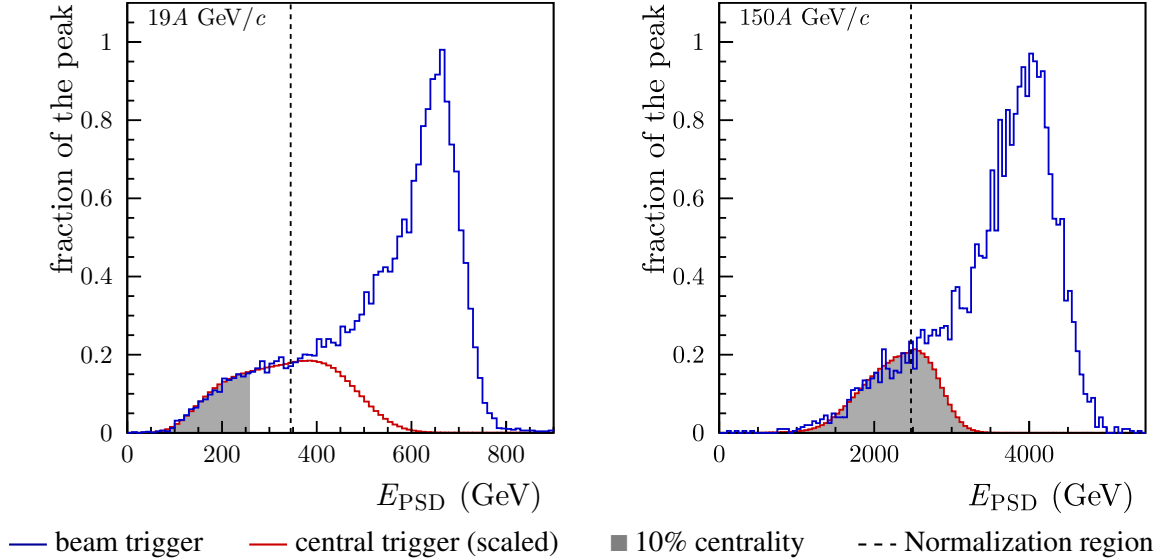

Figure 3: Distributions of the energy E_{PSD} measured by the PSD calorimeter for 19A (left plot) and 150A GeV/c (right plot) beam momentum, for minimum-bias selected (blue histograms) and central trigger selected (red histograms) events. Histograms are normalized to agree in the overlap region (from the beginning of the distribution to the black dashed line). The on-line central trigger was set to accept approximately 30% of most central inelastic events. The shaded area indicates 10% collisions with the smallest E_{PSD}.

The forward energy E_{F} cannot be measured directly. However, both E_{F} and E_{PSD} can be obtained from simulations using the Epos 1.99 (version CRMC 1.5.3) [24, 30, 31] model. A global factor c_{cent} (listed in Table 2) was calculated as the ratio of mean negatively charged pion multiplicities obtained with the two selection procedures in the 10% most *central* events. A possible dependence of the scaling factor on rapidity and transverse momentum was neglected. The resulting factors c_{cent} range between 1.002 and 1.005, corresponding to a correction at least an order of magnitude smaller compared to the systematic uncertainties of the measured particle multiplicities (see Sec. 3.5.2). The correction was therefore not applied and its possible impact was neglected in the final uncertainty calculation.

Finally, the Epos WNM [30] simulation was used to estimate the average number of wounded nucleons $\langle W \rangle$ for the 10% of events with the smallest number of spectator nucleons and with the smallest value of E_{F}. The average impact parameter $\langle b \rangle$ was also obtained for the latter selection. Results are listed in Table 2. Example distributions of W for 19A and 150A GeV/c beam momenta are shown in Fig. 4. These distributions are quite broad and emphasize the importance of proper simulation of the centrality selection when comparing model calculations with the experimental results.
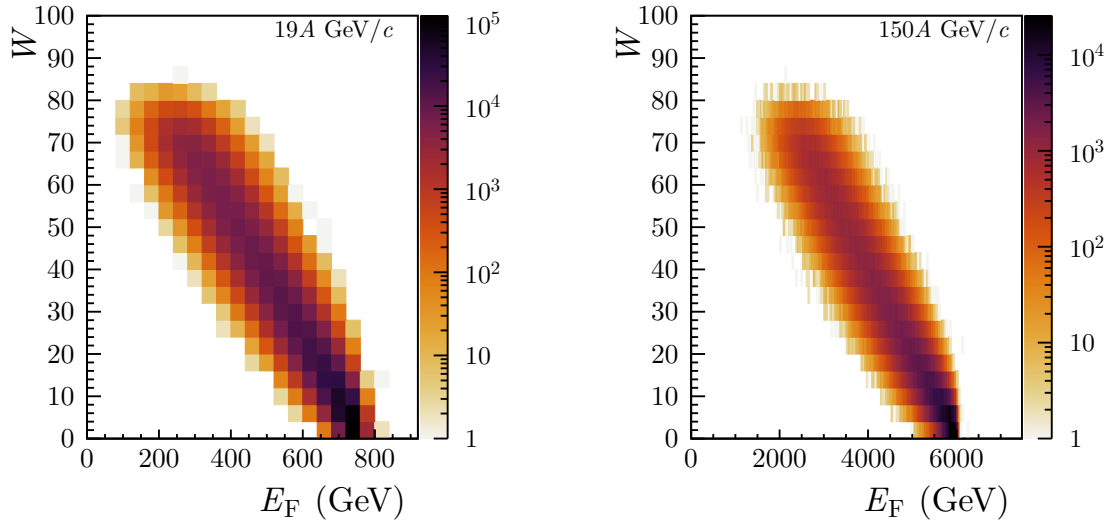
Figure 4: Distributions of number of wounded nucleons as a function of E_F for all inelastic Ar+Sc collisions at $19A$ and $150A$ GeV/c beam momentum calculated from EPOS [30].

p_{beam} [GeV/c]	$13A$	$19A$	$30A$	$40A$	$75A$	$150A$
$\langle W \rangle$ in EPOS WNM	61.4	61.2	60.9	60.9	60.8	61.0
$\langle W \rangle$ in EPOS E_F	61.0	60.8	60.6	60.4	60.3	60.6
$\langle b \rangle$ [fm]	1.82	1.95	2.00	2.09	2.23	2.08
c_{cent}	1.005	1.004	1.002	1.004	1.005	1.003

Table 2: The average number of wounded nucleons $\langle W \rangle$ and the average impact parameter $\langle b \rangle$ in the 10% most *central* Ar+Sc collisions estimated from simulations using EPOS [24, 30, 31]. Results from EPOS WNM are for centrality selection using the smallest number of spectators, whereas the EPOS E_F results are obtained using the forward energy E_F within the acceptance map in Ref. [28]. The last line presents numerical values of the c_{cent} factor for all the beam momenta (see text and Ref. [17] for more details).

3.2 Event and track selection

3.2.1 Event selection

For further analysis, Ar+Sc events were selected using the following criteria:

 (i) no off-time beam particle detected within a time window of ± 4 μs around the trigger particle,

 (ii) no other event trigger detected within a time window of ± 25 μs around the trigger particle,

(iii) beam particle detected in at least three planes out of four of BPD-1 and BPD-2 and in both planes of BPD-3,

(iv) a well-reconstructed interaction vertex with z-coordinate (fitted using the beam trajectory and TPC tracks) not farther away than 10 cm from the center of the Sc target,

 (v) an upper limit on the measured energy E_{PSD} selecting 10% of all inelastic collisions.

The event statistics after applying the selection criteria is summarized in Table 1.

3.2.2 Track selection

To select tracks of primary charged hadrons and to reduce the contamination by particles from secondary interactions and weak decays, the following track selection criteria were applied:

(i) Fitted x component of particle rigidity $q \cdot p$ should be positive. This selection minimizes the angle between the track trajectory and the TPC pad direction for the chosen magnetic field direction, reducing uncertainties of the reconstructed cluster position, energy deposition and track parameters.

(ii) Total number of reconstructed points on the track should be greater than 30, ensuring good resolution of dE/dx measurement.

(iii) Sum of the number of reconstructed points inside the vertex magnets (VTPC-1 and VTPC-2) should be greater than 15, which ensures good accuracy of track momentum fit.

(iv) The distance between the track extrapolated to the interaction plane and the reconstructed vertex (track impact parameter) should be smaller than 4 cm in the horizontal (bending) plane and 2 cm in the vertical (drift) plane.

In the case of dE/dx analysis, an additional criterion was used:

(i) track azimuthal angle ϕ should be within $30°$ with respect to the horizontal plane (x-z).

Similarly, specifically for $tof - dE/dx$ analysis, the following supplementary cuts were implemented:

(i) the extrapolated trajectory (as measured in the TPCs) reaches one of the ToF walls,

(ii) the last measured point on the track is located at least 70 cm upstream of the back wall of MTPCs, and its distance from the fitted track is within 4 cm,

(iii) measured flight time and charge for the pixel are of good quality (as in Refs. [32, 33]).

3.3 Identification techniques

Charged particle identification in NA61/SHINE is based on the ionization energy loss, dE/dx , in the gas of the TPCs and the time of flight, tof, obtained from the ToF-L and ToF-R walls. In the region of the relativistic rise of the ionization at large momenta, the measurement of dE/dx alone allows identification. At lower momenta, the dE/dx bands for different particle species overlap, and an additional measurement of tof is used for unambiguous particle identification. These two methods allow covering most of the relevant space in rapidity and transverse momentum, in particular the mid-rapidity region of K^+ and K^- spectra, which is an important part of the strong interaction program of NA61/SHINE. The acceptance of the two methods is shown in Figs. 5 and 6 for the 10% most *central* Ar+Sc interactions at $40A$ and $150A$ GeV/c, respectively. The figures also display the h^- analysis method [17], which provides large-acceptance measurements of π^- yields. At low beam energies, the $tof - dE/dx$ method extends the identification acceptance, while at the top SPS energy it overlaps with the dE/dx method.
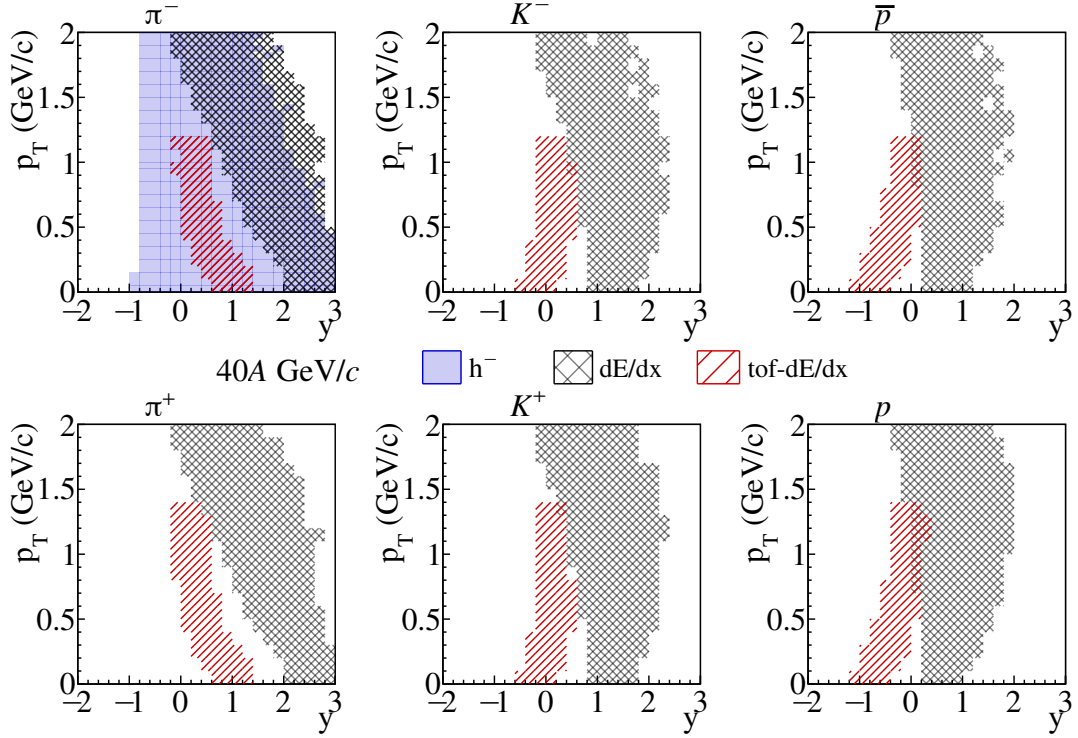
Figure 5: Acceptance of the $tof - dE/dx$ and dE/dx methods for identification of pions, kaons and protons in the 10% most *central* Ar+Sc interactions at $40A\,\mathrm{GeV}/c$. Negatively charged pion yield is also calculated using a so-called h^- method (see Ref. [17]).

3.3.1 Identification based on energy loss measurement dE/dx

Time projection chambers provide measurements of energy loss dE/dx of charged particles in the chamber gas along their trajectories. Simultaneous measurements of dE/dx and p allow extraction of information on particle mass. The mass assignment follows the procedure which was developed for the analysis of $p+p$ reactions as described in Ref. [13]. Values of dE/dx are calculated as the truncated mean (smallest 50%) of ionization energy loss measurements along the track trajectory. As an example, dE/dx measured in Ar+Sc interactions at $150A\,\mathrm{GeV}/c$ is presented in Fig. 7, for positively and negatively charged particles, as a function of momentum.

In the dE/dx method the contributions of $e^+, e^-, \pi^+, \pi^-, K^+, K^-, p, \bar{p}$ and d are obtained by fitting the dE/dx distributions in bins of laboratory momentum p and transverse momentum p_T. The data are divided into 13 logarithmic bins in p in the range 5–100 GeV/c and into linear bins in p_T. Thin binning in p_T is used up to $p_T = 0.6$ GeV/c (bin width 0.05 GeV/c) and wider bins are used above this value (0.1 GeV/c). Due to the crossing of Bethe-Bloch curves at low momenta, the applicability of particle identification based solely on dE/dx measurement is limited to tracks with $p > 5$ GeV/c. Only bins with a total number of selected tracks greater than 100 were used in the further analysis.

The particle yield as a function of dE/dx in each p, p_T bin is fitted by the sum of asymmetric Gaussians with widths $\sigma_{i,l}$ depending on the particle type i and the number of points l measured in the TPCs (the
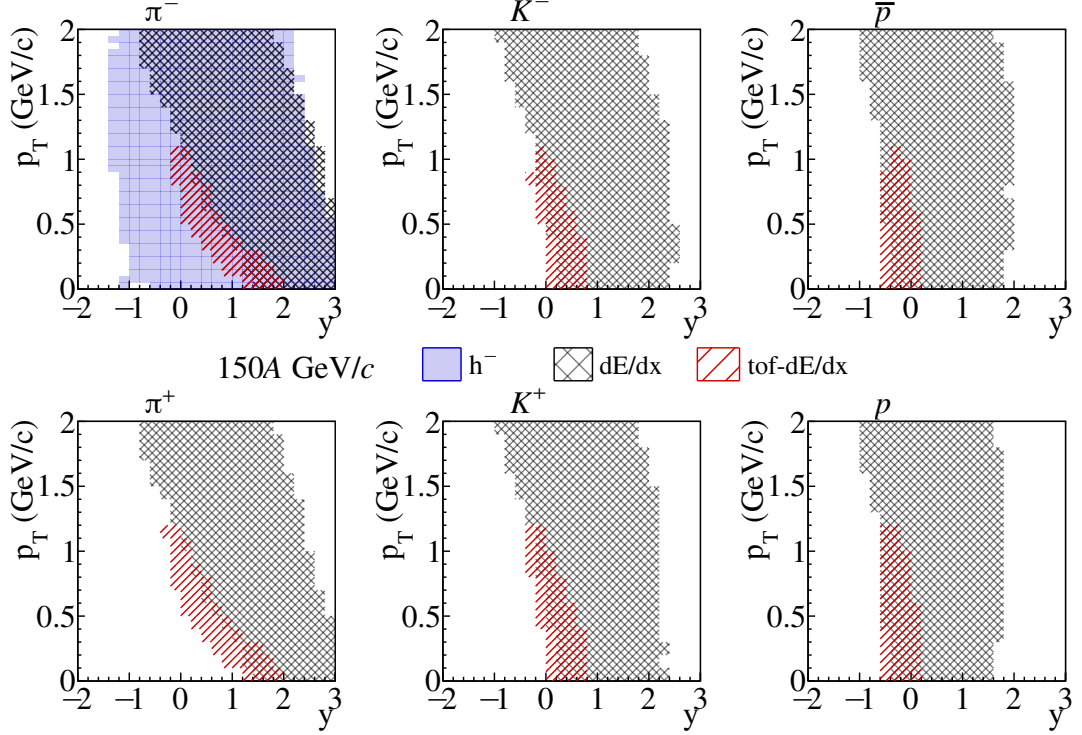
Figure 6: Acceptance of the $tof-dE/dx$ and dE/dx methods for identification of pions, kaons and protons in the 10% most *central* Ar+Sc interactions at $150A\,\mathrm{GeV}/c$. Negatively charged pion yield is also calculated using a so-called h^- method [17].

method is based on previous work described in Refs. [34, 35]):

$$\rho(x) = \sum_{i=\pi^{\pm},\,K^{\pm},p,\bar{p},d,e^{\pm}} N_i \frac{1}{\sum_l n_l} \sum_l \frac{n_l}{\sqrt{2\pi}\sigma_{i,l}} \exp\left[-\frac{1}{2}\left(\frac{x-x_i+\frac{2}{\sqrt{2\pi}}\delta_l\sigma_{i,l}}{(1\pm\delta_l)\,\sigma_{i,l}}\right)^2\right], \qquad (1)$$

where truncated mean energy loss dE/dx is denoted with x, the peak position of the dE/dx distribution for particle type i is expressed as x_i and the expression $2\delta_l\sigma/\sqrt{2\pi}$ accounts for the drift of the peak related to the truncated tail of the cluster charge distribution. The amplitude of the contribution of particles of type i is expressed as N_i and the parameter $\delta_l = \delta_0/l$ accounts for the asymmetry of the distribution. Variable n_l is the number of tracks with the number of points l in the sample and thus the summation over l is in fact a weighted average of Gaussian distributions with variable widths:

$$\sigma_{i,l} = \frac{\sigma_0}{\sqrt{l}}\left(\frac{x_i}{x_\pi}\right)^{\alpha}, \qquad (2)$$

where σ_0, similarly to δ_0 in the previous equation, is assumed to be common for all particle types and α is a universal constant. The details about the fitting procedure can be found in Ref. [36]. Examples of final fits are shown in Fig. 8.
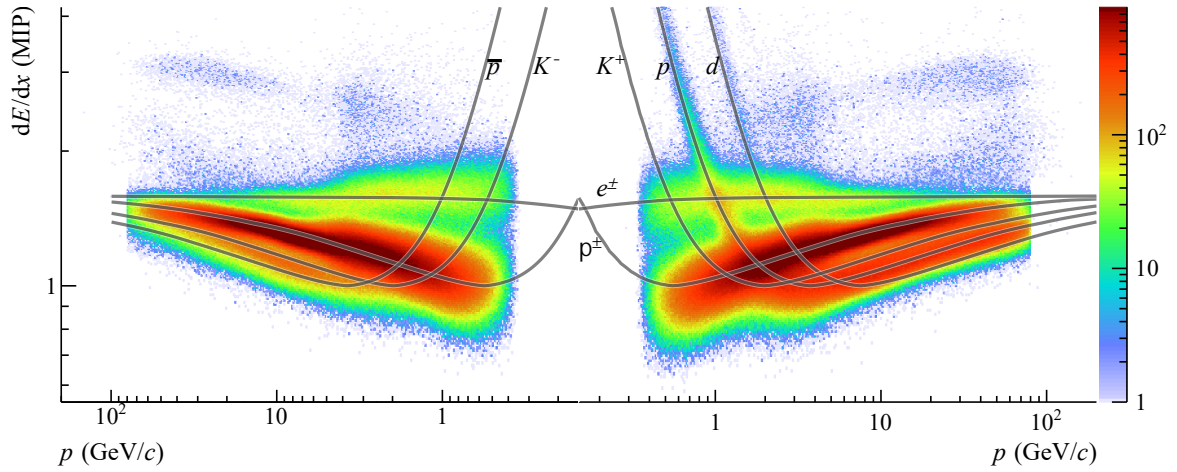
Figure 7: Distribution of charged particles in the $dE/dx - p$ plane. The energy loss (in units of the minimum ionizing particle) in the TPCs is shown for different charged particles produced in Ar+Sc collisions at $150A\,\text{GeV}/c$. Expectations for the dependence of the mean dE/dx on p for the considered particle types are shown by the curves calculated based on the Bethe-Bloch function. The absolute dE/dx scale is precise to 2%.

3.3.2 Identification based on time of flight and energy loss measurements ($tof - dE/dx$)

Identification of π^+, π^-, K^+, K^-, p and $\bar{p}$ at low momenta (0.5-10 GeV/c) is possible when measurement of dE/dx is combined with time-of-flight information tof. Timing signals from the constant-fraction discriminators and signal amplitude information are recorded for each tile of the ToF-L/R walls. The coordinates of the track intersection with the front face are used to match the track to tiles with valid tof hits. The position of the extrapolation point on the scintillator tile is used to correct the measured value of tof for the propagation time of the light signal inside the tile. The distribution of the difference between the corrected tof measurement and the value calculated from the extrapolated track trajectory length with the assumed mass hypothesis can be described well by a Gaussian with a standard deviation of 80 ps for ToF-R and 100 ps for ToF-L. These values represent the tof resolution including all detector effects.

Momentum phase space is subdivided into bins of 1 GeV/c in p and 0.1 GeV/c in p_T. Only bins with more than 1000 entries were used for extracting yields with the $tof - dE/dx$ method.

The square of the particle mass m^2 is obtained from tof, from the momentum p and from the fitted trajectory length l:

$$m^2 = (cp)^2 \left(\frac{c^2\,tof^2}{l^2} - 1 \right) .$$

(3)

For illustration distributions of m^2 versus p are plotted in Fig. 9 for positively (*left*) and negatively (*right*) charged hadrons produced in 10% *central* Ar+Sc interactions at $30A\,\text{GeV}/c$. Bands which correspond to different particle types are visible.

Example distributions of particles in the $m^2 - dE/dx$ plane for the selected Ar+Sc interactions at $30A\,\text{GeV}/c$ are presented in Fig. 10. Simultaneous dE/dx and tof measurements lead to improved separation between different hadron types. In this case, a simple Gaussian parametrization of the dE/dx distribution for a given hadron type can be used.
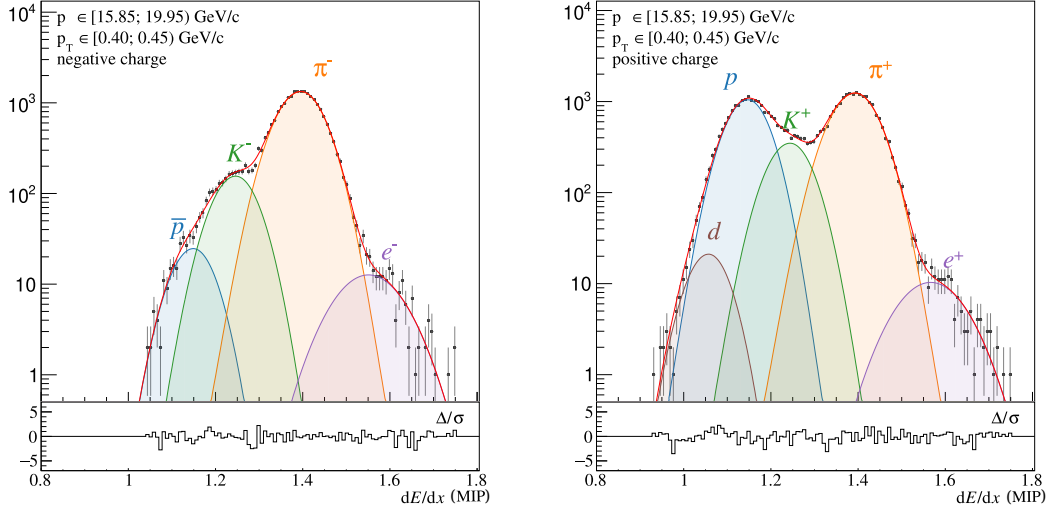
Figure 8: The dE/dx distributions for negatively (*left*) and positively (*right*) charged particles in a selected $p - p_T$ bin produced in *central* Ar+Sc collisions at 75A GeV/c. The fits by a sum of contributions from different particle types are shown by solid lines. The corresponding residuals (the difference between the data and fit divided by the statistical uncertainty of the data) are shown in the bottom plots. The absolute dE/dx scale is precise to 2%.
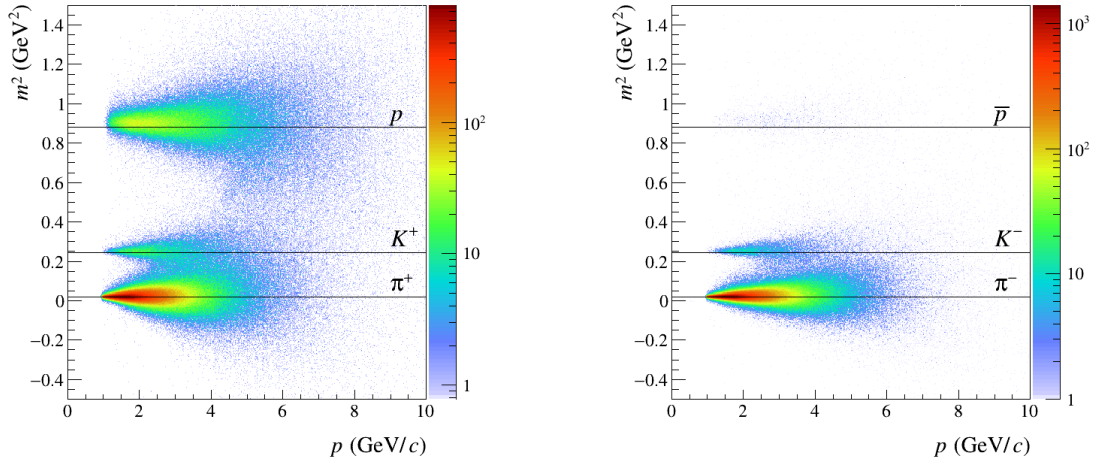

Figure 9: Distribution of particles in the plane laboratory momentum and mass squared derived using time-of-flight measured by ToF-R (*right*) and ToF-L (*left*) produced in *central* Ar+Sc collisions at 30A GeV/c. The lines show the expected mass squared values for different hadron species.

The $tof - dE$/dx identification method proceeds by fitting the two-dimensional distribution of particles in the dE/d$x - m^2$ plane. Fits were performed in the momentum range from 2-10 GeV/c and transverse momentum range 0-1.5 GeV/c. Particles with total momentum less than 2 GeV/c are identified based on m^2 measurement alone, as different species of particles are separated enough. Contamination of electrons to pions identified in such a way is removed with a dedicated dE/dx cut (see Fig. 10 and Ref. [33]). For positively charged particles the fit function included contributions of p, K^+, π^+, and e^+, and for negatively
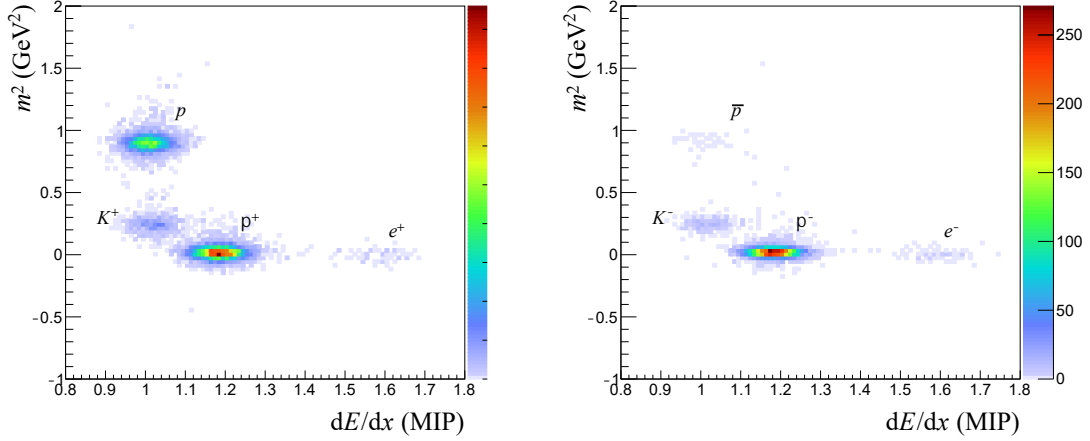
Figure 10: Example distributions of particles in m^2 and dE/dx plane in a single bin ($2\,\text{GeV}/c < p < 3\,\text{GeV}/c$, $0.5\,\text{GeV}/c < p_T < 0.6\,\text{GeV}/c$) for positively (*left*) and negatively (*right*) charged particles measured in *central* Ar+Sc collisions at $30A\,\text{GeV}/c$.

charged particles the corresponding anti-particles were considered. The deuterons are not accounted for in the fits, as they are removed with a cut on measured m^2. The fit function for a given particle type was assumed to be the product of a Gaussian function in dE/dx and a sum of two Gaussian functions in m^2 (in order to properly describe the tails of the m^2 distributions). In order to simplify the notation in the fit formulae, the peak positions of the dE/dx and m^2 Gaussians for particle type j are denoted as x_j and y_j, respectively. The fitted function reads:

$$
\begin{aligned}
\rho(x,y) &= \sum_{j=p,\pi,K,e} \rho_j(x,y) \\
&= \sum_j \frac{N_j}{2\pi\,\sigma_x}\, exp\left[-\frac{(x-x_j)^2}{2\sigma_x^2}\right]\left(\frac{f}{\sigma_{y_1}}\,exp\left[\frac{(y-y_j)^2}{2\sigma_{y_1}^2}\right] + \frac{(1-f)}{\sigma_{y_2}}exp\left[\frac{(y-y_j)^2}{2\sigma_{y_2}^2}\right]\right),
\end{aligned} \tag{4}
$$

where N_j and f are amplitude parameters, x_j, σ_x are means and width of the dE/dx Gaussians and y_j, σ_{y_1}, σ_{y_2} are means and widths of the m^2 Gaussians, respectively. The total number of parameters in Eq. 4 is 16. Imposing the constraint of normalization to the total number of tracks N in the kinematic bin

$$
N = \sum_i N_i \,, \tag{5}
$$

the number of parameters is reduced to 15. Two additional assumptions were adopted:

(i) the fitted amplitudes were required to be greater than or equal to 0,

(ii) $\sigma_{y1} < \sigma_{y2}$ and $f > 0.7$, the "core" distribution dominates the m^2 fit.

An example of the $tof - dE/dx$ fit obtained in a single phase-space bin for positively charged particles in *central* Ar+Sc collisions at $30A\,\text{GeV}/c$ is shown in Fig. 11.

The $tof - dE/dx$ method allows fitting the kaon yield close to mid-rapidity. This is not possible using the dE/dx method alone. Moreover, the kinematic domain in which pion and proton yields can be fitted
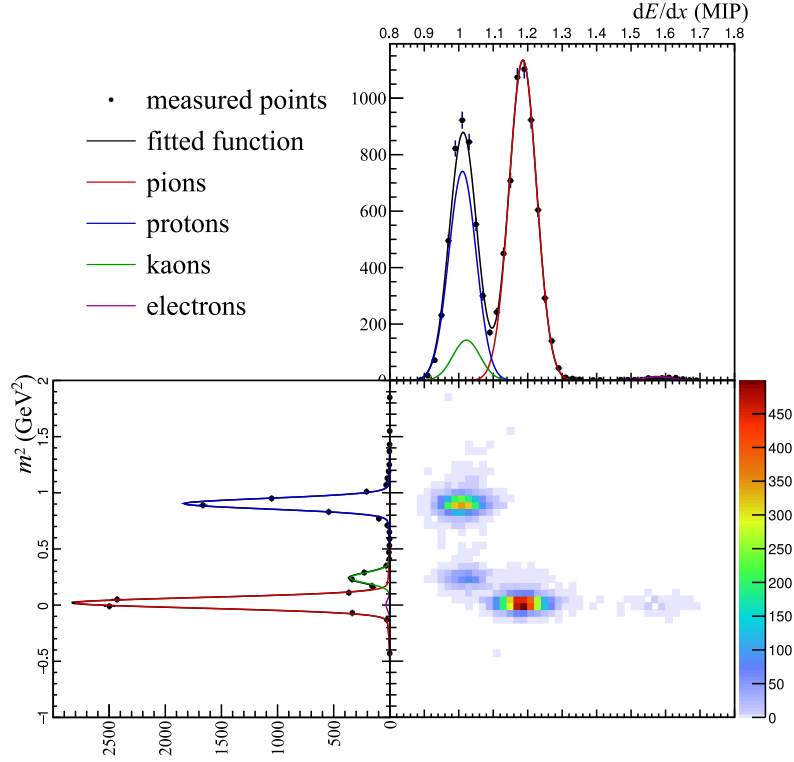
Figure 11: Example of the $tof - dE/dx$ fit (Eq. 4) obtained in a single bin ($2 < p < 3$ GeV/c and $0.5 < p_T < 0.6$ GeV/c) for positively charged particles in *central* Ar+Sc collisions at 30A GeV/c.

is enlarged by the $tof - dE/dx$ analysis. The results from both methods partly overlap at the highest beam momenta. In these regions, the results from both PID methods were combined using standard formulae [37].

3.3.3 Probability method

The 1D (dE/dx) and 2D ($tof - dE/dx$) models fitted to experimental distributions provide information on the contribution of individual particle species to total measured yields in bins of p and p_T. In order to unfold these contributions in the dE/dx method, for each particle trajectory with measured charge q, p, p_T and dE/dx a probability P_i of being a given species can be calculated as:

$$P_i(p, p_T, dE/dx) = \frac{\rho_i^{p,p_T}(dE/dx)}{\sum\limits_{i=\pi,K,p,e,d} \rho_i^{p,p_T}(dE/dx)} \, ,$$

(6)

where ρ_i^{p,p_T} is the probability density according to the model with parameters fitted in a given (p, p_T) bin calculated for dE/dx of the particle.
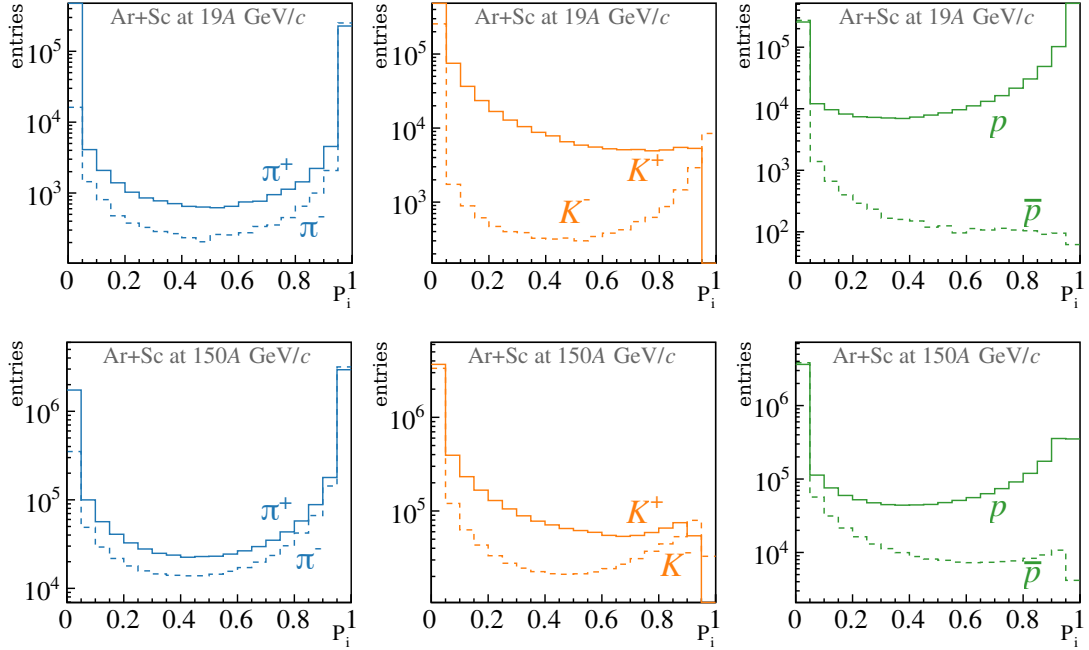
Figure 12: Distribution of probabilities of a track being a pion, kaon, proton for positively (solid lines) and negatively (dashed lines) charged particles from dE/dx measurements in *central* Ar+Sc collisions at $19A$ (*top*) and $150A$ GeV/c (*bottom*).

Similarly, in the $tof - dE/dx$ method (see Eq. 4) for $p > 2$ GeV/c the particle type probability is given by

$$P_i(p, p_T, dE/dx, m^2) = \frac{\rho_i^{p,p_T}(dE/dx, m^2)}{\sum\limits_{i=\pi,K,p,e} \rho_i^{p,p_T}(dE/dx, m^2)} \,, \tag{7}$$

In the case of low-momentum particles ($p < 2$ GeV/c), the assigned probability is either 0 or 1 based on the measured m^2. For illustration, particle type probability distributions for positively and negatively charged particles produced in *central* Ar+Sc collisions at $19A$ and $150A$ GeV/c are presented in Fig. 12 for the dE/dx fits and in Fig. 13 for the $tof - dE/dx$ fits. In the case of perfect particle type identification, the probability distributions in Figs. 12 and 13 will show entries at 0 and 1 only. In the case of incomplete particle identification (overlapping dE/dx or $tof - dE/dx$ distributions) values between these extremes will also be populated.

The probability method allows transforming the fit results performed in (p, p_T) bins to results in (y, p_T) bins. Hence, for the probability method the mean number of identified particles in a given kinematical bin (e.g. (p, p_T)) is given by [38]:

$$n[i]_{dE/dx}^{raw}(y, p_T) = \frac{1}{N_{ev}} \sum_{j=1}^{N_{trk}} P_i(p, p_T, dE/dx) \,, \tag{8}$$

for the dE/dx identification method and:

$$n[i]_{dE/dx,m^2}^{raw}(y, p_T) = \frac{1}{N_{ev}} \sum_{j=1}^{N_{trk}} P_i(p, p_T, dE/dx, m^2) \,, \tag{9}$$
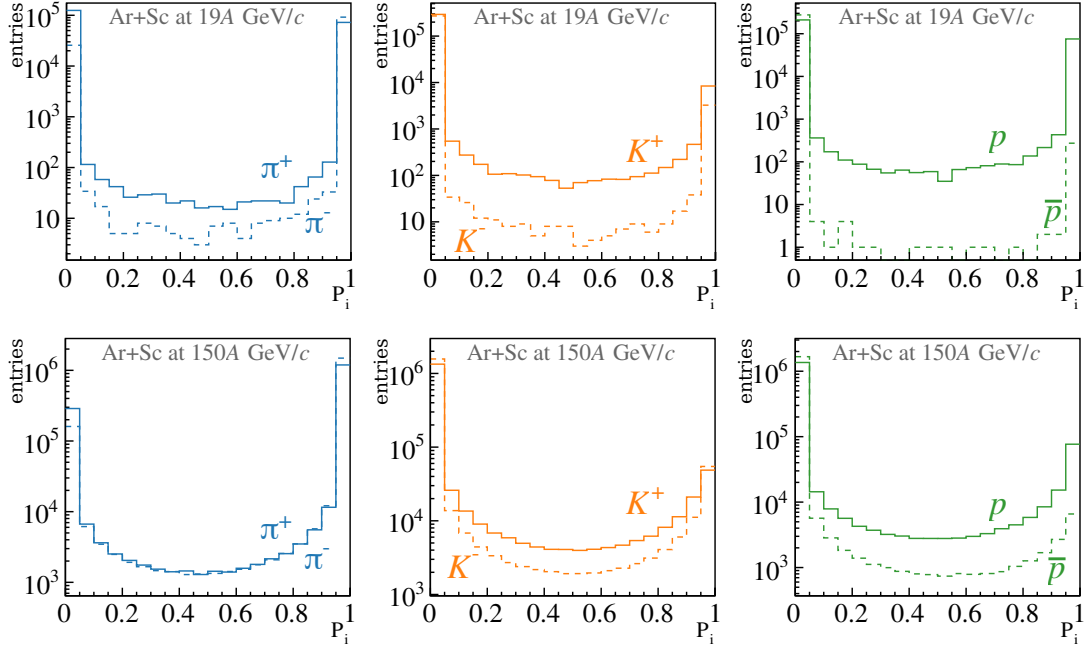
18

Figure 13: Distribution of probabilities of a track being a pion, kaon, proton for positively (solid lines) and negatively (dashed lines) charged particles from $tof - dE/dx$ measurements in *central* Ar+Sc collisions at $19A$ (*top*) and $150A \, \text{GeV}/c$ (*bottom*).

for the $tof - dE/dx$ procedure, where P_i is the probability of particle type i given by Eqs. 6 and 7, j the summation index running over all entries N_{trk} in the bin, N_{ev} is the number of selected events. In the case of the dE/dx analysis, the probabilities P_i were linearly interpolated in the (p, p_T) plane in order to minimize bin-edge effects.

3.4 Corrections and uncertainties

In order to estimate the true number of each type of identified particle produced in Ar+Sc interactions, a set of corrections was applied to the extracted raw results. These were obtained from a simulation of the NA61/SHINE detector followed by event reconstruction using the standard reconstruction chain. Only inelastic Ar+Sc collisions were simulated in the target material. The EPOS1.99 model [24] was selected to generate primary inelastic interactions as it best describes the NA61/SHINE measurements [12]. A GEANT3-based program chain was used to track particles through the spectrometer, generate decays and secondary interactions, and simulate the detector response (for details see Ref. [12]). Simulated events were then processed using the standard NA61/SHINE reconstruction chain. The reconstructed tracks were matched to the simulated particles based on the cluster positions of reconstructed simulated tracks. The selection of *central* events was based on the number of forward spectators. Corrections depend on the particle identification technique (i. e. dE/dx or $tof - dE/dx$). Hadrons that were not produced in the primary interaction can amount to a significant fraction of the selected tracks, thus a special effort was undertaken to evaluate and subtract this contribution. The correction factors were calculated in the same bins of y and p_T as the particle spectra. The magnitude of correction factors reflects the effects of detector acceptance, track selection criteria, and reconstruction efficiency. The generated EPOS events will be

referred to as "MCgen" and the label "MCsel" is given to the events with simulated detector response and reconstructed using standard NA61/SHINE chain with event and track selection criteria matching the ones used in the analysis of the experimental data.

3.4.1 Corrections of the spectra

The total correction for biasing effects listed in Sec. 3 items (b) - (g) (influence of item (a) on the final result was found to be negligible) was calculated in the following way:

$$n[i]^{\text{corrected}} = \left(n[i]^{\text{raw data}} - n[i]^{\text{MCsel decay}}\right) \cdot \frac{n[i]^{\text{MCgen}}}{n[i]^{\text{MCsel primary}}} , \tag{10}$$

where, $n[i]$ stands for the per-event yield in the bin i of the $y - p_T$ histogram of a given particle type, specifically:

$n[i]^{\text{corrected}}$	stands for the corrected yield,
$n[i]^{\text{raw data}}$	stands for the raw data yield,
$n[i]^{\text{MCsel decay}}$	is the contribution of feed-down from weak decays in MCsel,
$n[i]^{\text{MCsel primary}}$	is the contribution of primary particles in MCsel,
$n[i]^{\text{MCgen}}$	is a pure MC simulated yield.

The correction of spectra due to contamination by weak decays $(n[i]^{\text{MCsel decay}})$ is weakly correlated with the primary hadron yields, therefore this contribution is accounted for in an additive way (later referred to as c_{add}). The combined geometrical and efficiency correction is applied as the quotient in the second term of the Equation 10 of the numbers of reconstructed primary tracks and all simulated tracks in a given momentum space bin (later referred to as c_{mult}).

The corrections for the spectra obtained with the $tof - \mathrm{d}E/\mathrm{d}x$ PID method account additionally for the ToF tile efficiency $\varepsilon_{\text{pixel}}(p, p_T)$. It was calculated from the measured data as the probability of observing a valid reconstructed ToF hit if there exists an extrapolated TPC track which intersects with a given ToF tile. The ToF hit was considered valid if the signal satisfied the quality criteria given in Ref. [32].

The ToF pixel efficiency factor $\varepsilon_{\text{pixel}}(p, p_T)$ was used in the MC simulation by weighting each reconstructed MC track passing all event and track selection cuts by the efficiency factor of the corresponding ToF tile. Then, the number of selected MC tracks $n[i]^{\text{MCsel}}$ becomes the sum of weights of those tiles which contribute to bin i:

$$n[i]^{\text{MCsel primary}} = \sum_{j=1}^{N_{\text{trk}}} \varepsilon_{\text{pixel}}^{j}(p, p_T) . \tag{11}$$

Only hits in working tiles, with efficiency higher than 50%, were taken into account in the identification and correction procedures.

The uncertainty of the multiplicative part of the correction was calculated assuming that the "MCsel primary" sample is a subset of the "MCgen" sample and thus has a binomial distribution. The uncertainty of the c_{mult} ratio is thus given by:

$$\sigma_{\text{stat}}(c_{\text{mult}}) = \frac{n[i]^{\text{MCgen}}}{n[i]^{\text{MCsel primary}}} \sqrt{\frac{N[i]^{\text{MCgen}} - N[i]^{\text{MCsel primary}}}{N[i]^{\text{MCgen}} \cdot N[i]^{\text{MCsel primary}}}} , \tag{12}$$

where $N[i]$ is the number of tracks in bin i (not normalized with the number of events, unlike $n[i]$).

The statistical uncertainty of the additive weak-decay feed-down correction (c_{add}) is added to the statistical uncertainty as a quadratic average.

3.4.2 Tuning of feed-down in MC corrections

Another source of contamination of experimental results are the secondary particles originating from weak decays, that are reconstructed as primary ones. Figure 14 shows the contribution of decay products originating from different decay parents and Fig. 15 shows the relative cumulative contribution of weak-decay feed-down to the measured particle spectra. While the yield of weak-decay products is negligibly small in the case of kaons (K^+ and K^-) it is significant in the case of pions (π^+ and π^-) and (anti-)protons which are contaminated by the decay products from K^0_S and (anti-)hyperons. The precise estimate of the feed-down contribution for these particle species is crucial for the correct calculation of spectra and mean multiplicities, as the yields of decaying particles are directly affecting the magnitude of corrections. The
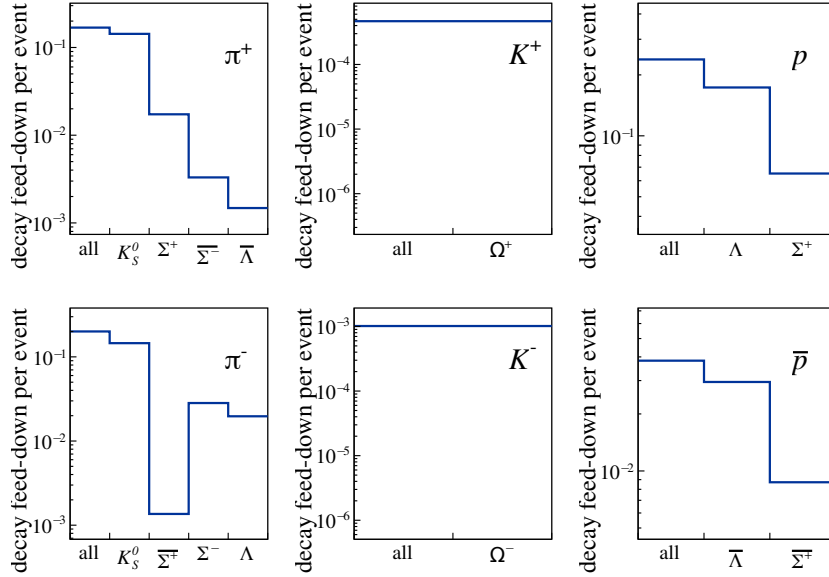

Figure 14: Contribution per event of reconstructed secondary tracks in the fiducial volume of the detector originating from weak decays and erroneously identified as products of primary interaction (based on EPOS at 150A GeV/c).

EPOS model used in the MC simulation does not reproduce the properties of strangeness enhancement in nucleus-nucleus collisions, thus the yields of strange mesons and strange baryons are typically largely underestimated. A procedure for tuning the contribution of weak decays was developed to improve the precision of the calculated corrections. It is based on data-derived quantities: mean multiplicities of particles estimated in measured data are compared with the ones extracted from MC simulation. Thus, using the preliminary results on charged kaon multiplicities from this analysis it is possible to construct an auto-tuning factor for yields of K^0_S:

$$K^0_{S \ (\text{EPOS tuned})} = K^0_{S \ (\text{EPOS})} \times \frac{\langle K^+ \rangle_{data} + \langle K^- \rangle_{data}}{\langle K^+ \rangle_{(\text{EPOS})} + \langle K^- \rangle_{(\text{EPOS})}} \ . \tag{13}$$
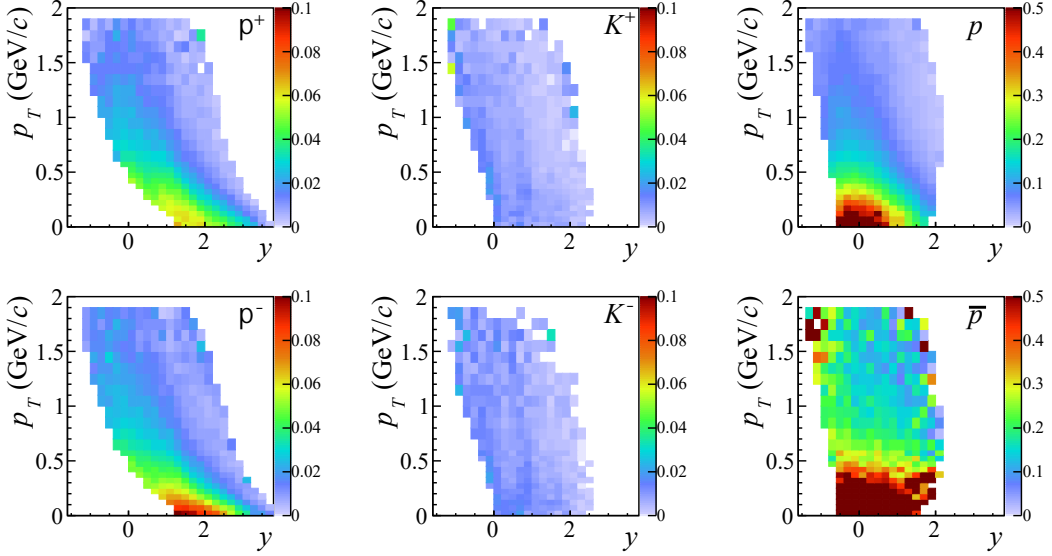
Figure 15: An example of the relative contribution of weak decay products in spectra of hadrons identified with dE/dx method at $150A\,\text{GeV}/c$ plotted in $y - p_T$ plane. The corrections are based on the EPOS model with data-derived tuning (see text for details). The feed-down for π^- and π^+ is typically on the level of 1%-3%, reaching up to 10% in the case of low-p_T π^-. Secondary kaons can only originate from sparsely produced Ω^+ and Ω^-decays, thus the correction is well below 1%. Spectra of protons and anti-protons are heavily influenced by the decays of Λ and Σ^+ ($\bar{\Lambda}$ and $\bar{\Sigma}^+$ for anti-protons) – in these cases, feed-down correction can reach over 50% at low p_T. Similar numbers hold true for all collision energies.

In the absence of measurements of strange (anti-)baryons in Ar+Sc collisions, the best effort is made to estimate their yields using existing data. At SPS collision energies mean multiplicities of Λ baryons are well approximated by the following relation:

$$\langle \Lambda \rangle = \alpha \cdot \left(\langle K^+ \rangle - \langle K^- \rangle \right), \tag{14}$$

where α is usually close to unity. A relevant parametrization of α was extracted from NA49's Pb+Pb data [39] and used to get an approximate estimate of Λ yield in Ar+Sc at each collision energy. Scaling of the yields of Λ and $\Sigma^{\pm}$ are calculated as:

$$\Lambda_{\text{(EPOS tuned)}} = \Lambda_{\text{(EPOS)}} \times \frac{\alpha \cdot \left(\langle K^+ \rangle - \langle K^- \rangle \right)}{\langle \Lambda \rangle_{\text{(EPOS)}}} . \tag{15}$$

Obtained tuning factors are presented in Table 3, showing also the uncertainties assigned to these corrections. Furthermore, the yields of other strange and multi-strange baryons were tuned with the same factors as Λ and $\Sigma^{\pm}$. The imperfect description of rapidity and transverse momentum dependence in the EPOS model is not accounted for in the presented calculation, hence the large values of added uncertainties. In Figs. 17 and 18 the total uncertainty introduced by the contribution of secondary particles is denoted with grey lines.

p_{beam} [GeV/c]	13A	19A	30A	40A	75A	150A	assigned uncertainty
K_S^0 tuning factor	1.339	1.339	1.297	1.371	1.332	1.307	5%
α	0.89	0.89	1.00	1.08	1.12	0.95	5%
$\Lambda, \Sigma^+, \Sigma^-$ tuning factor	1.582	1.582	1.562	1.634	1.522	1.507	10%

Table 3: Multiplicative factors used for tuning the feed-down contribution in the EPOS MC simulation of *central* Ar+Sc collisions.

3.5 Corrected spectra

The final spectra of different types of hadrons produced in Ar+Sc collisions are defined as:

$$\frac{\mathrm{d}^2 n}{\mathrm{d}y\,\mathrm{d}p_T} = \frac{1}{\Delta y \cdot \Delta p_T} n[i]^{\text{corrected}} \;, \tag{16}$$

where Δy and Δp_T are the bin sizes and $n[i]^{\text{corrected}}$ represents the mean multiplicity of given particle type in the i-th bin in y and p_T obtained with either $\mathrm{d}E/\mathrm{d}x$ or $tof - \mathrm{d}E/\mathrm{d}x$ identification method, as introduced in Eq. 10.

The resulting two-dimensional distributions $\frac{\mathrm{d}^2 n}{\mathrm{d}y\,\mathrm{d}p_T}$ of $\pi^-, \pi^+, K^-, K^+, p$ and $\bar{p}$ produced in the 10% most *central* Ar+Sc collisions at different SPS energies are presented in Fig. 16.

3.5.1 Statistical uncertainties

Statistical uncertainties of multiplicities calculated in the $tof - \mathrm{d}E/\mathrm{d}x$ method were derived under the assumption of Poissonian statistics in a single bin and no correlation between the bins. The resulting uncertainty in (p, p_T) bin is given by:

$$\sigma_{stat}^2(n[i]^{\text{raw}}) = \frac{1}{N_{\text{ev}}} \sum_{j=1}^{N_{\text{trk}}} P_i^j(p, p_T, \mathrm{d}E/\mathrm{d}x, m^2)^2 \;. \tag{17}$$

An alternative method, bootstrapping, was used to calculate statistical uncertainties in the case of the $\mathrm{d}E/\mathrm{d}x$ identification technique. One hundred bootstrap samples were generated through random sampling with replacement, performed on the level of events. Each bootstrap sample is injected into the procedure of particle identification and calculation of y-p_T spectra. The errors are then estimated as standard deviations of yields at all bootstrap samples. It was verified that the number of bootstrap samples was large enough and that the distribution of yields resembles the normal distribution, allowing to assign the standard deviation as the statistical error. It was found that bootstrapping and weighted variances (Eq. 17) methods yield similar values of uncertainty.

The contribution to statistical uncertainties from the MC correction factors (discussed in detail in Sec. 3.4) is propagated into final uncertainties using the standard procedure.
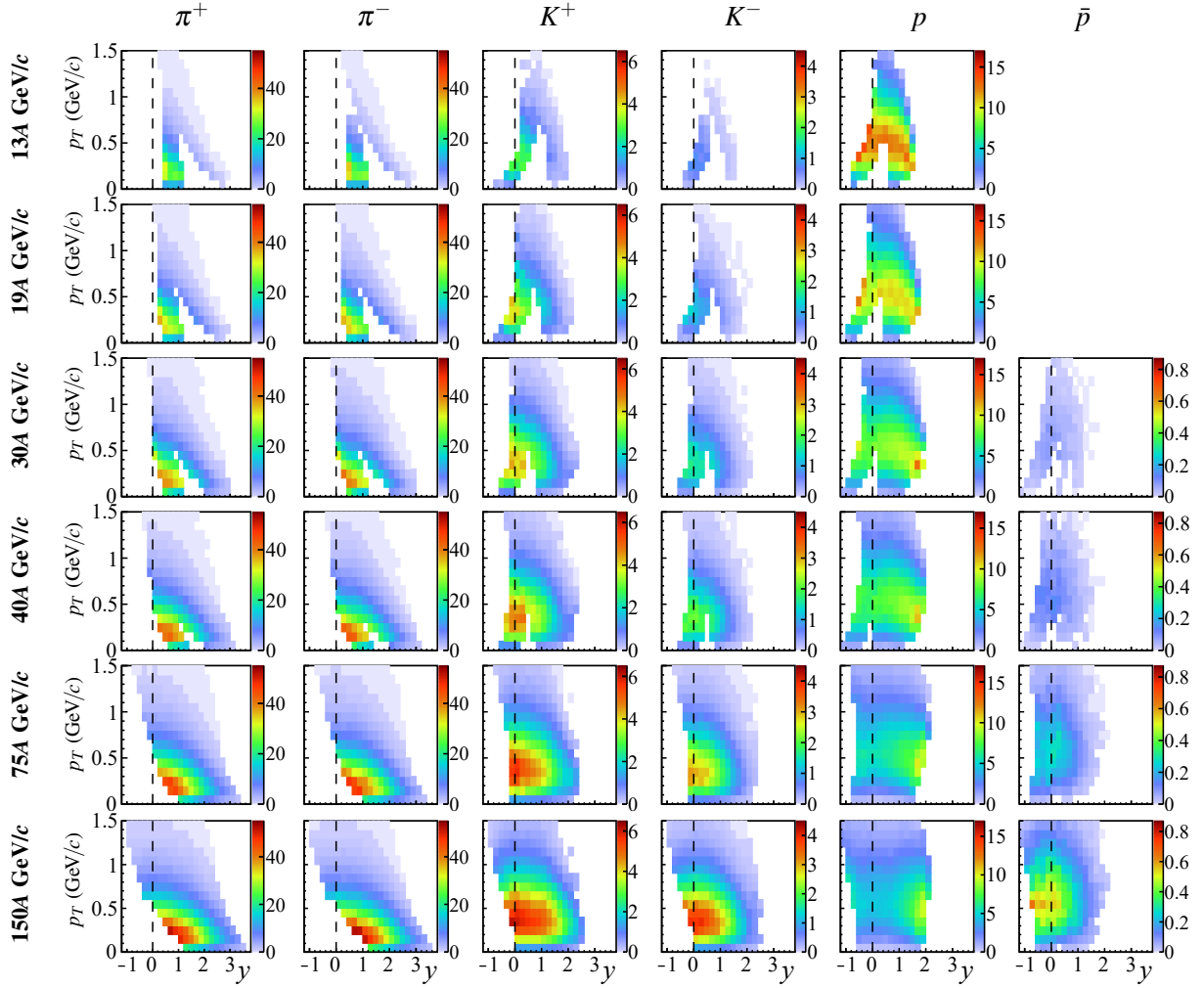
Figure 16: Two-dimensional distributions (y vs. p_T) of double differential yields (Eq. 16) of π^-, π^+, K^-, K^+, p and $\bar{p}$ produced in the 10% most *central* Ar+Sc interactions at 13*A*, 19*A*, 30*A*, 40*A*, 75*A* and 150*A* GeV/*c*.

3.5.2 Systematic uncertainties

The following sources of systematic uncertainties were considered in this study:

(I) **Particle identification** methods utilized in this analysis provide measurements of particle yields through the fits of multi-parameter models. In order to increase stability, some of the parameters need to be fixed. Moreover, it may happen that the fitted variable reaches the imposed limit. Such cases may lead to biases in the estimation of particle yields and therefore were carefully studied.

(a) dE/dx method
In the dE/dx method the fits of peak positions of kaons and protons were found to have the largest influence on particle yields and their ratios, while also having a relatively high variance, in particular in sparsely populated bins. The strategy used in this study (described in Sec. 3.3.1) involved fixing these parameters at pre-fitted values and assuming their independence of transverse momentum. The differences between prefits and results of bin-by-bin fits were

studied and the spread within a single momentum bin was found at approx. 0.2%. Therefore in order to determine a potential bias introduced by fixing relative peak positions, they are varied by $\pm 0.1\%$. Contribution to the biases from other fit parameters was found negligible.

(b) *tof*-dE/dx

Systematic uncertainties were estimated by shifting the mean (x_j and y_j) of the two-dimensional Gaussians (Eq. 4) fitted to the m^2-dE/dx distributions by $\pm 1\%$, which corresponds to typical uncertainty of the fitted parameters. Additional systematic uncertainty arises for the $tof - \mathrm{d}E/\mathrm{d}x$ method from the quality requirements on the signals registered in the ToF pixels. In order to estimate this uncertainty the nominal signal selection thresholds were varied by $\pm 10\%$

(II) **Event selection** criteria based on any measurements downstream of the target may also introduce bias in the results. Uncertainties due to this were estimated through an independent variation of criteria listed below:

(a) Removal of events with off-time particles – the time window in which no off-time beam particle is allowed was varied by $\pm 2\ \mu$s with respect to the default value of 4 μs.

(b) Fitted main vertex position – the range of allowed main vertex z-coordinate was varied by ± 5 cm at both ends.

(III) Track selection:

The contribution to systematic uncertainty from track selection criteria was estimated by varying the following parameters:

(a) The required minimum of the total number of clusters was varied by $+5$ and -5 points.

(b) Similarly, the minimum number of clusters in VTPCs was varied by ± 5 points. Note that both of the cuts on the number of points affect the acceptance of the dE/dx PID method as well, which was also taken into account.

(c) The influence of the selection of azimuthal angle was investigated in the case of dE/dx-only PID by comparing the results obtained for $|\phi| < 30°$ (default value), $|\phi| < 20°$ and $|\phi| < 40°$.

(IV) Feed-down correction:

Uncertainties of weak decays feed-down correction were accounted for as described in Sec. 3.4.2.

The maximal difference of the particle yields in each bin of y and p_T obtained under varied criteria was assigned as the systematic uncertainty. The relative contribution of each of the listed sources to the systematic uncertainties of the final spectra of identified particles is shown in Figs. 17 (dE/dx method) and 18 (*tof*-dE/dx method). The total uncertainty is typically 3–10% for charged pions, charged kaons, and protons, while it exceeds 10% in the case of anti-protons. The relative total uncertainties tend to increase at lower collision energies.
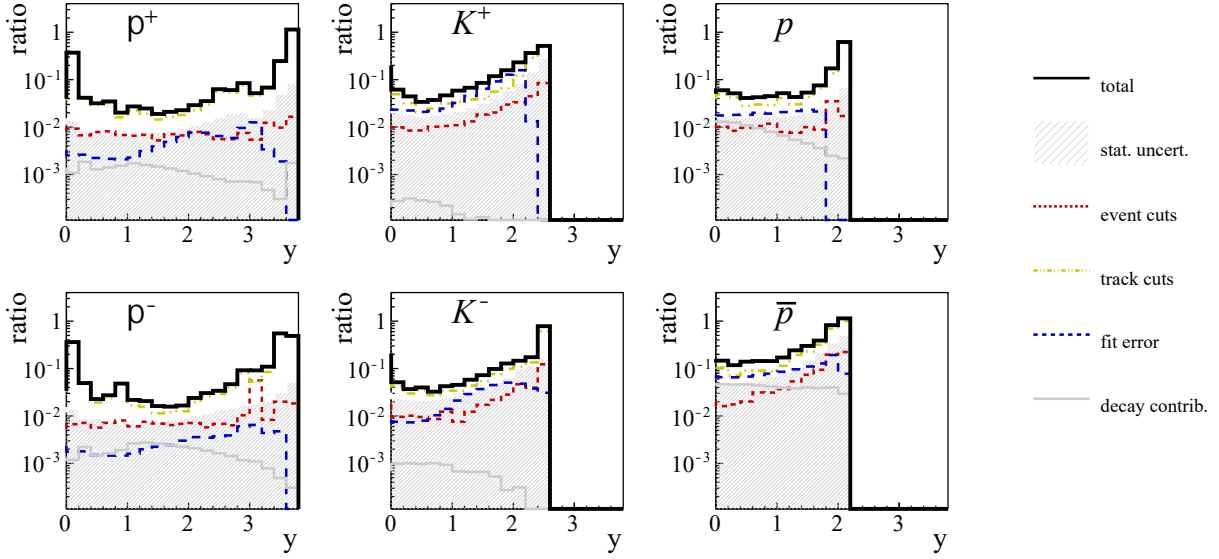
Figure 17: Systematic uncertainty relative to the measured yield of double-differential distributions obtained with dE/dx PID method, integrated in p_T, shown for each identified species in dependence on rapidity y at p_{beam}=150A GeV/c. Different contributions to the total uncertainty are plotted, along with statistical error (shaded area). Large fluctuations seen at low-rapidity uncertainties of pion spectra are due to narrow acceptance in p_T.
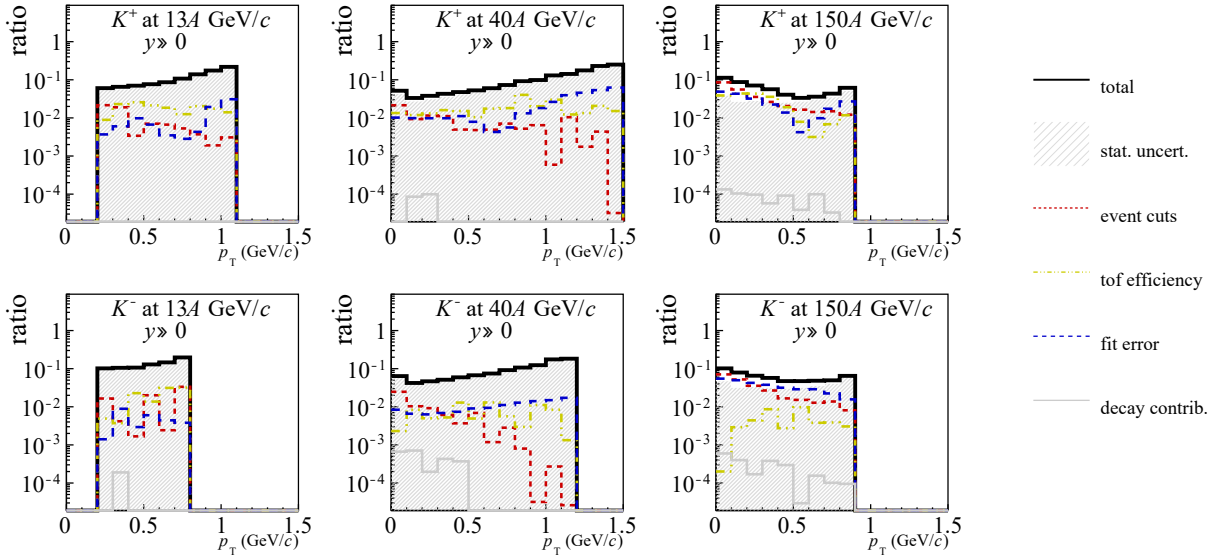

Figure 18: Systematic uncertainty relative to the measured yield of double-differential distributions in y and p_T for charged kaons, obtained with *tof*-dE/dx PID method, shown in dependence on transverse momentum p_T at mid-rapidity for *central* Ar+Sc collisions at p_{beam}=13A, 40A and 150A GeV/c. Different contributions to the total uncertainty are plotted, along with statistical error (shaded area).

4 Results

Figure 16 displays two dimensional distributions $\mathrm{d}^2n/(\mathrm{d}y\,\mathrm{d}p_\mathrm{T})$ of π^-, π^+, K^-, K^+, p and $\bar{p}$ produced in 10% most *central* Ar+Sc collisions at beam momenta of 13A, 19A, 30A, 40A, 75A and 150A GeV/c. The spectra obtained using $\mathrm{d}E/\mathrm{d}x$ and $tof - \mathrm{d}E/\mathrm{d}x$ PID methods were combined to ensure a maximal momentum space coverage. Empty bins in momentum space are caused by insufficient bin entries for the identification methods used in the analysis or the uncertainty of MC correction factors exceeding a certain threshold. The gaps in the acceptance grow with decreasing collision energies, however, reliable measurement of key properties of charged hadron production is still possible even at the lowest beam momentum. In y-p_T bins where both $tof - \mathrm{d}E/\mathrm{d}x$ and $\mathrm{d}E/\mathrm{d}x$ measurements exist, a weighted average is calculated using standard formulae [37].

The transverse momentum spectra of identified hadrons are extrapolated to account for the missing acceptance. Extrapolation of p_T spectra allows for an accurate calculation of rapidity distribution, which in turn is also extrapolated into regions of missing measurements to calculate mean multiplicities. Only the experimental results up to $p_\mathrm{T} <$1.5 GeV/c are considered since the contribution of misidentified particles becomes large at higher values of p_T, which results in a higher systematic uncertainty. The contribution of the extrapolation towards high p_T ($>$1.5 GeV/c) is typically of the order of 1%. At small p_T ($\approx$ 0 − 0.1 GeV/c) the extrapolation or interpolation (when a gap between $tof - \mathrm{d}E/\mathrm{d}x$ and $\mathrm{d}E/\mathrm{d}x$ data exists) ranges from 0 to 20%. The extrapolation methods and their applicability differ for each of the studied particle species and thus are described separately in Secs. 4.1, 4.2 and 4.3.

Subsequently, Sec. 5 reviews presented measurements in terms of collision energy and system size dependence, including also a comparison with relevant models. Presented results are then discussed in the context of the onset of deconfinement and an emerging phenomenon of the onset of QGP fireball.

4.1 Charged pions

4.1.1 Transverse momentum spectra

The measured double differential charged pion spectra in rapidity and transverse momentum at 13A−150 A GeV/c beam momenta are presented in Fig. 16.

In order to account for the regions outside $\mathrm{d}E/\mathrm{d}x$ and $tof - \mathrm{d}E/\mathrm{d}x$ PID acceptance, the p_T distributions in each bin of rapidity were fitted independently in two separate p_T intervals: [0.0,0.6] and [0.6,1.5] GeV/c. Such a procedure was employed due to the influence of radial flow and a large contribution from resonance decays, which is difficult to model reliably. Dividing the p_T range into two subsets allows for an accurate interpolation as well as the extrapolation of the transverse spectra. A simultaneous fit to data from both PID methods is performed using the following formula:

$$f(p_T) = \frac{A \cdot p_T}{T\,(m_\pi + T)} \exp\left(\frac{m_\pi - m_T}{T} \right),\tag{18}$$

where T is the inverse slope parameter, m_π and m_T denote pion's rest and transverse masses respectively and A is a normalization factor, T and A are fit parameters. Example fit results are shown in Fig. 19. The inverse slope parameter T is decreasing from mid-rapidity towards higher values of rapidity.
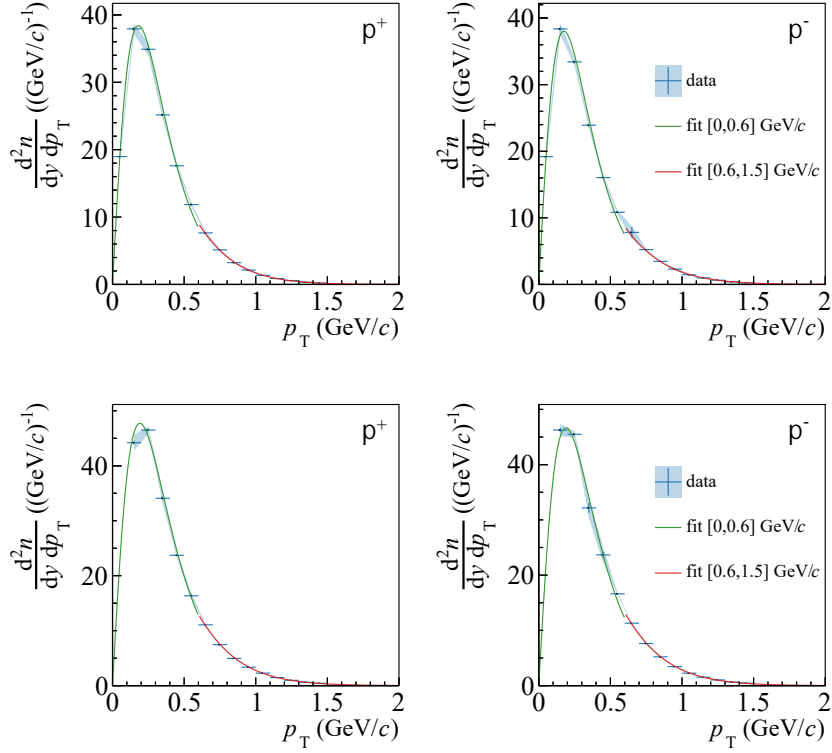
Figure 19: Example fits to charged pion, π^+ (left) and π^- (right), transverse momentum spectra ($p_{\text{beam}} = 30A\,\text{GeV}/c$ and $75A\,\text{GeV}/c$ at $0.6 < y < 0.8$, *top* and *bottom* panels respecitvely). Exponential fits (Eq 18) are performed in two regions separately: $p_T \in [0.0, 0.6]$ and $p_T \in [0.6, 1.5]\,\text{GeV}/c$. The fitted functions are used to extrapolate the yields beyond $p_T = 1.5\,\text{GeV}/c$ and interpolate the yields in case a gap in acceptance appears due to different coverage of PID methods. In rare cases, the yield is extrapolated also in the region of $p_T < 0.1\,\text{GeV}/c$. The vertical bars represent statistical uncertainties and the shaded bands stand for the systematic uncertainties.

4.1.2 Rapidity spectra

The $\mathrm{d}n/\mathrm{d}y$ yields are obtained by integration of the $\mathrm{d}^2n/\mathrm{d}y\,\mathrm{d}p_T$ spectra and the addition of the integral of the fitted functions in the regions of missing acceptance. An additional contribution to the systematic uncertainty of 25% of the extrapolated yield is added to account for a possible bias due to model selection. Figure 20 displays the resulting $\mathrm{d}n/\mathrm{d}y$ distributions for all collision energies. The one-dimensional rapidity spectra are fitted with double-Gaussians with means equidistant from mid-rapidity:

$$f(y) = \frac{A_0\,A_{\text{rel}}}{\sigma_0\sqrt{2\pi}}\,\exp\left(-\frac{(y-y_0)^2}{2\sigma_0^2}\right) \;+\; \frac{A_0}{\sigma_0\sqrt{2\pi}}\,\exp\left(-\frac{(y+y_0)^2}{2\sigma_0^2}\right), \tag{19}$$

where A_0 is the amplitude, A_{rel} is a parameter reflecting the asymmetry between forward and backward rapidity hemispheres, σ_0 is the width of individual peaks and y_0 stands for the displacement of contributing distributions from mid-rapidity. The measured data covers only the region of positive rapidity, thus the parameter A_{rel} is not fitted, but instead taken from the published results of complementary analyses, with the h^- method, described in detail in Ref. [17]. The fit quality is satisfactory for beam momenta from $19A\,\text{GeV}/c$ to $150A\,\text{GeV}/c$. Good agreement of the measured data with the fitted model allows to extrapolate
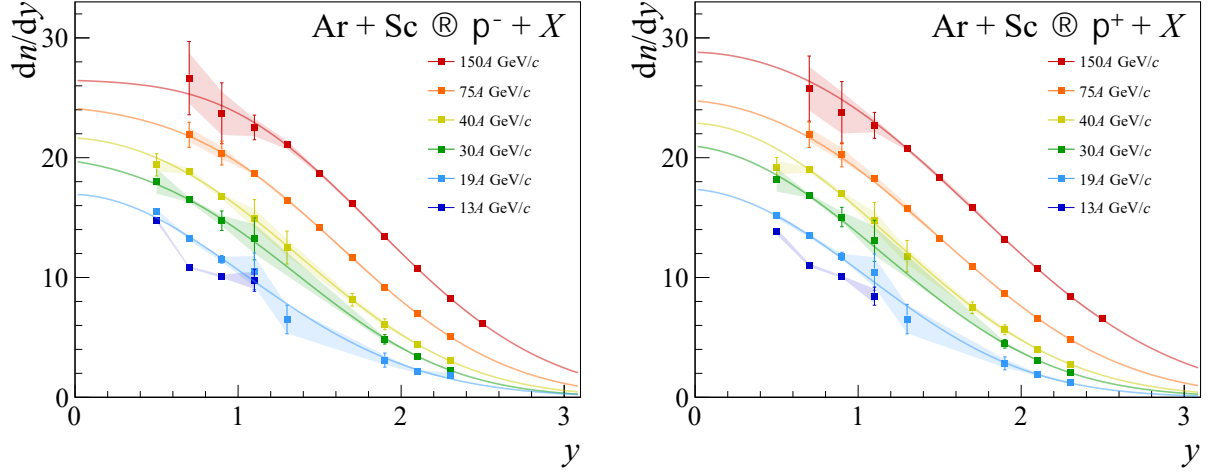
Figure 20: Rapidity spectra of charged pions (π^+ and π^-) measured with dE/dx and tof-dE/dx methods in 10% most *central* Ar+Sc collisions. The line is a sum of two Gaussians, equidistant from mid-rapidity with differing amplitudes (Eq. 19). The statistical uncertainties do not exceed the size of the markers and the systematic uncertainties are shown as shaded bands.

the spectra into the unmeasured region and thus calculation of mean multiplicities of charged pions. In the case of $13A\,\text{GeV}/c$, the extrapolation was not performed, as the measurement covers too small acceptance region. Moreover, the spectrum of negatively charged pions at $13A\,\text{GeV}/c$ shows an unphysical shape and does not agree with the results from the h^- method, thus suggesting a possible bias, not fully accounted for in the estimation of measurement uncertainties. Table 4 displays the mean multiplicity as the integral of the fitted function for beam momenta $19A$–$150A\,\text{GeV}/c$. The statistical uncertainty is calculated as the integral error due to parameter uncertainties and their covariance matrix. The fit accounts for both statistical and systematic uncertainties of measured data, however, an additional systematic uncertainty of 5% is imposed on the data based on the largest discrepancies observed when comparing the fit integrals with parameters fixed at values taken from h^- method [17] against the unconstrained fit.

p_{beam} (GeV/c)	$\langle \pi^+ \rangle$	$\langle \pi^- \rangle$
$19A$	$45.2 \pm 2.2 \pm 2.4$	$45.2 \pm 2.0 \pm 2.4$
$30A$	$59.3 \pm 1.4 \pm 2.9$	$59.8 \pm 1.4 \pm 2.9$
$40A$	$65.9 \pm 1.6 \pm 2.9$	$66.4 \pm 1.7 \pm 2.9$
$75A$	$83.0 \pm 1.3 \pm 3.3$	$84.5 \pm 0.9 \pm 3.3$
$150A$	$107.5 \pm 2.7 \pm 4.6$	$104.3 \pm 3.3 \pm 4.6$

Table 4: Mean multiplicities of π^+ and π^- mesons calculated as the integrals of the fits (Eq. 19) to the measured identified pion spectra in 10% most *central* Ar+Sc collisions at $19A$-$30A\,\text{GeV}/c$. The values are provided with statistical (σ_{stat}) and systematic (σ_{sys}) uncertainties in the form: $\langle \pi \rangle \pm \sigma_{\text{stat}} \pm \sigma_{\text{sys}}$.

The parameters of the function fitted to charged pion rapidity distribution are shown in dependence on beam momentum in Fig. 21. Both the width σ and the distance between the peaks increase with increasing collision energy.

Finally, rapidity spectra of negatively charged pions were compared with the results of h^- analysis [17] for all beam momenta. Comparisons for $30A$ and $150A\,\text{GeV}/c$ are shown in Fig. 22. The results from the h^-

method were obtained for the 0-5% centrality interval and to match the results of this study were scaled by the ratio of numbers of wounded nucleons $N_W^{0\text{-}10\%}/N_W^{0\text{-}5\%}$. The results from the two different analysis methods agree within calculated uncertainties.
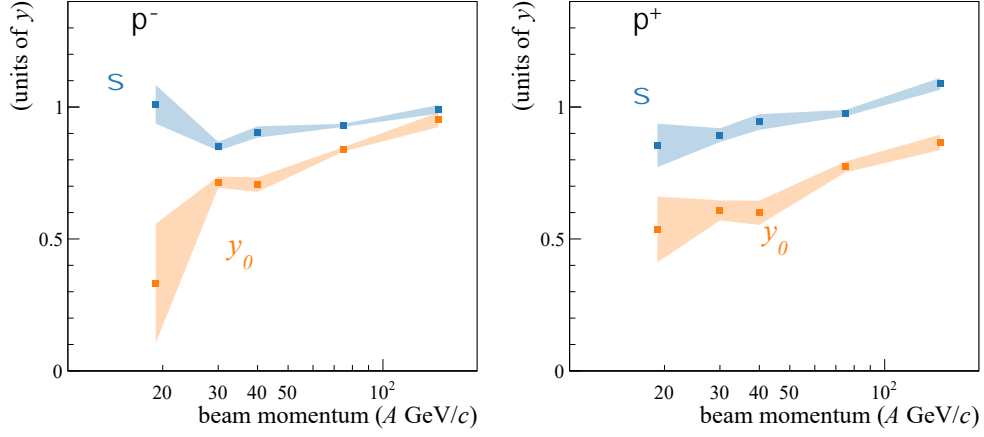

Figure 21: The parameters of double-Gaussian fit (Eq. 19) to charged pion rapidity spectra in 10% most *central* Ar+Sc collisions. The shaded bands illustrate the statistical uncertainties of the fit.
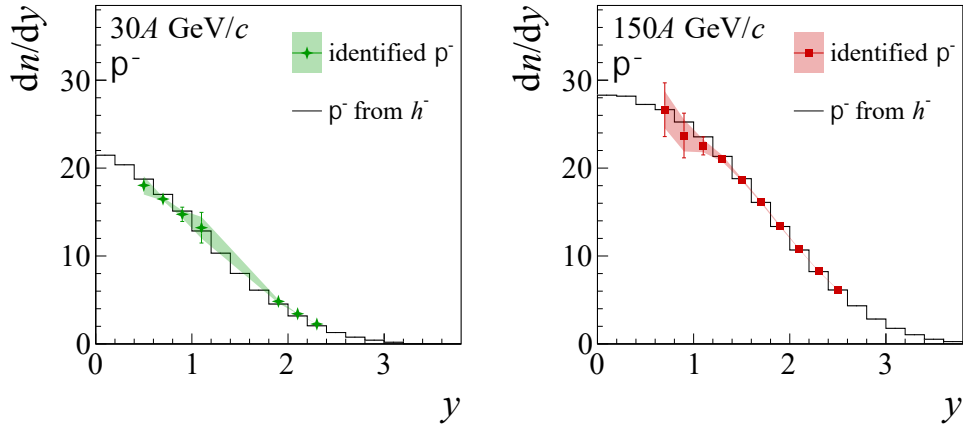

Figure 22: Comparison of rapidity spectra of negatively charged pions measured with dE/dx and tof-dE/dx methods (colored markers) against the results obtained with the h^- method [17] (black line). Both results consider *central* Ar+Sc collisions, and the comparison is displayed for beam momenta of 30A and 150 A GeV/c. The statistical uncertainties do not exceed the size of the markers and the systematic uncertainties are shown as shaded bands.

4.2 Charged kaons

4.2.1 Transverse momentum spectra

Figure 16 illustrates the spectra in rapidity and transverse momentum ($d^2n/(dy\,dp_T)$) of charged kaons identified with dE/dx and $tof - dE/dx$ PID methods at 13A–150A GeV/c. For all six measured beam

momenta, the acceptance covers the region close to mid-rapidity as well as a large part of the spectrum in forward rapidity.
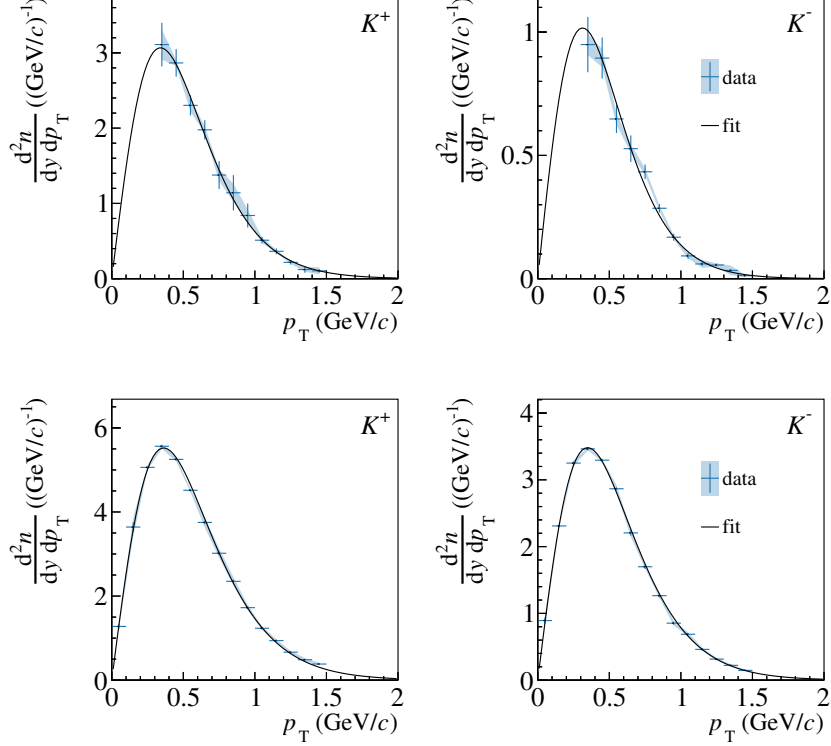
Figure 23: Example fits to charged kaon transverse momentum spectra ($p_{\text{beam}} = 19A\,\text{GeV}/c$ at $0.4 < y < 0.6$ and $p_{\text{beam}} = 150A\,\text{GeV}/c$ at $0.6 < y < 0.8$, *top* and *bottom* panels respectively) obtained for 10% most *central* Ar+Sc collisions. Exponential fits are performed in the range of $p_T \in [0.0, 1.5]$. The fitted functions are used to extrapolate the yields beyond $p_T = 1.5\,\text{GeV}/c$ and interpolate the yields in case a gap in acceptance appears due to different coverage of PID methods. The vertical bars represent statistical uncertainties and the shaded bands stand for the systematic uncertainties.

In order to obtain dn/dy yields, the data is extrapolated in p_T to account for unmeasured regions at high values of p_T and in rare cases at low p_T as well. Kaon spectra are well approximated by single-interval exponential fits. The effects of collective flow bend the spectra up (or down) in the case of lighter (or more massive) particles, while kaon p_T distribution remains approximately exponential. Moreover, the contribution to the spectra from products of weak decays is minimal. The fit formula is analogous to the one used in the fits to the pion spectra (Eq. 18):

$$f(p_T) = \frac{A \cdot p_T}{T(m_K + T)} \exp\left(\frac{m_K - m_T}{T}\right) . \tag{20}$$

The function is fitted in the acceptance region and its integral beyond the acceptance is added to the measured data. Example fits are shown in Fig. 23. The fit of the transverse momentum spectra with Eq. 20 determines the inverse slope parameter T. Figure 24 shows the rapidity dependence of T for each measured beam momentum. It can be observed that at $75A$ and $150A\,\text{GeV}/c$ the fitted values of T are approximately constant up to $y \approx 0.8$, which agrees with observations made in the analysis of Pb+Pb [35, 40] data.
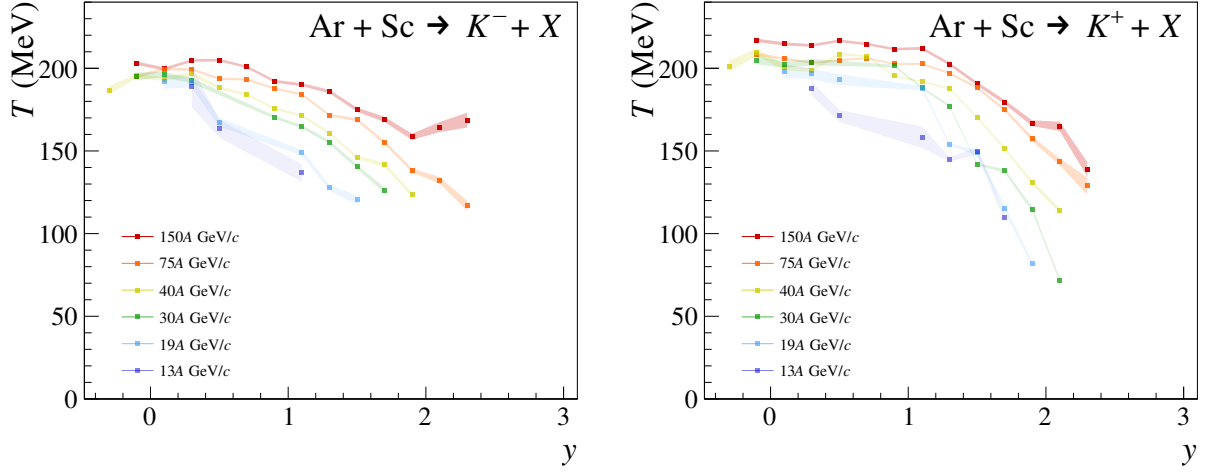
Figure 24: Rapidity dependence of the inverse slope parameter T fitted to charged kaon p_T distribution in 10% most *central* Ar+Sc collisions. The shaded bands represent the total fit uncertainty.

The transverse momentum spectra of charged kaons at mid-rapidity for six beam momenta are presented in Fig. 25. The mid-rapidity is defined as the range from 0.0 to 0.2, with the exception of p_{beam}=13A GeV/c, where due to limited acceptance the mid-rapidity range is taken as from 0.2 to 0.4. The symmetry of the charged kaon spectra with respect to $y = 0$ was verified with available theoretical models to be within 1%. Thus for 13A, 19A and 30A GeV/c the missing points in the low p_T region (see Fig. 16) are complemented with measured reflections of the spectrum with respect to $y = 0$.

The dn/dy yield of charged kaons at mid-rapidity is obtained from the measured spectrum (including points reflected with respect to $y = 0$) and fitted with an exponential function (Eq. 20). The yields of K^+ and K^- calculated with this procedure and values of the inverse slope parameter T resulting from the fit of p_T spectra of $K^\pm$, together with their statistical and systematic uncertainties, are summarized in Table 5. Table 6 summarizes K/π ratios at mid-rapidity. As the analysis presented in this paper does not offer acceptance for charged pions at mid-rapidity, negatively charged pion yields at mid-rapidity were taken from [17], and appropriately scaled to 10% most *central* Ar+Sc events with the use of number on wounded nucleons calculated within EPOS WNM (see Sec. 4.1.2). Based on the agreement of $\pi^\pm$ mean multiplicities well within total uncertainties (Table 4) and very similar y distribution shapes (Fig. 21), it was assumed that the yields of charged pions at mid-rapidity are close enough for the purpose of the K/π ratio calculation.

4.2.2 Rapidity spectra

Rapidity distributions (dn/dy) are obtained through integration of the double differential spectra in p_T at each bin of rapidity and by addition of extrapolated yields in unmeasured regions. An additional contribution to the systematic uncertainty of 25% of the extrapolated yield is added to account for a possible bias due to choice of the fit function. Figure 26 shows the rapidity distribution for each of the analysed collision energies. The spectra are fitted with the sum of two Gaussians placed symmetrically
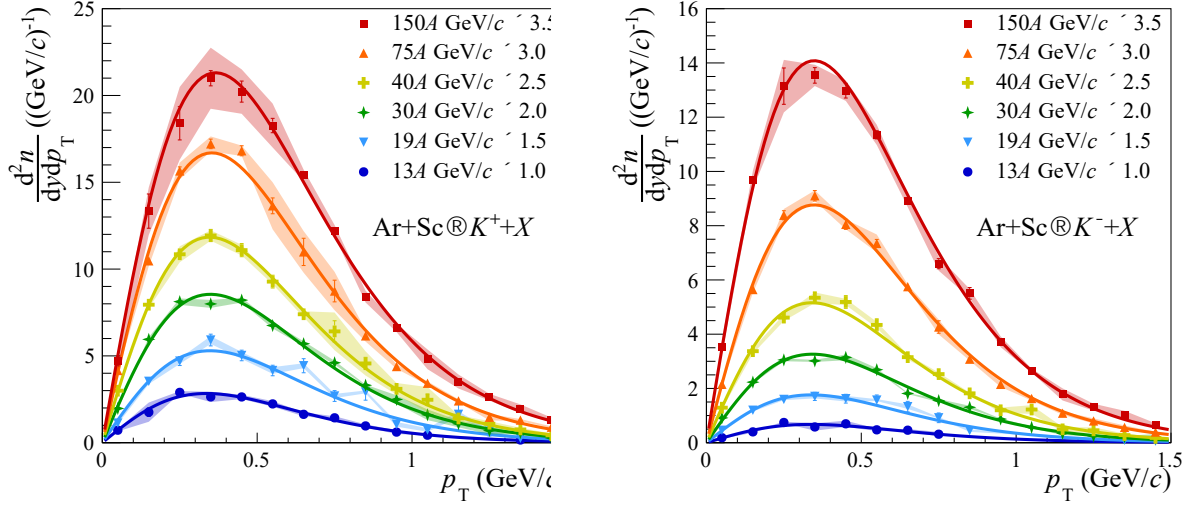
Figure 25: Transverse momentum spectra of K^+ (*left*) and K^- (*right*) at mid-rapidity produced in 10% most *central* Ar+Sc collisions. Error bars show statistical uncertainties, while shaded bands correspond to systematic uncertainties. The lines represent the fitted functions (Eq. 20). The spectra were scaled for better readability.

p_{beam} (GeV/c)	$\left(\frac{dn}{dy}\right)_{y\approx 0}(K^+)$	$\left(\frac{dn}{dy}\right)_{y\approx 0}(K^-)$	$T(K^+)$ (MeV)	$T(K^-)$ (MeV)
13A	$1.885 \pm 0.049 \pm 0.072$	$0.455 \pm 0.025 \pm 0.030$	$189.3 \pm 5.6 \pm 11.3$	$191 \pm 16 \pm 15$
19A	$2.628 \pm 0.082 \pm 0.039$	$0.808 \pm 0.030 \pm 0.025$	$200.3 \pm 5.5 \pm 7.2$	$191.4 \pm 4.6 \pm 3.9$
30A	$2.998 \pm 0.044 \pm 0.034$	$1.116 \pm 0.020 \pm 0.012$	$201.6 \pm 2.8 \pm 12.4$	$195.1 \pm 1.8 \pm 4.0$
40A	$3.300 \pm 0.047 \pm 0.068$	$1.430 \pm 0.021 \pm 0.017$	$198.5 \pm 2.5 \pm 8.4$	$193.4 \pm 1.3 \pm 2.8$
75A	$3.968 \pm 0.041 \pm 0.078$	$2.034 \pm 0.016 \pm 0.021$	$206.0 \pm 0.8 \pm 6.6$	$200.6 \pm 1.0 \pm 2.7$
150A	$4.432 \pm 0.048 \pm 0.108$	$2.780 \pm 0.025 \pm 0.040$	$218.0 \pm 1.2 \pm 11.4$	$200.5 \pm 1.0 \pm 6.6$

Table 5: Numerical values of the K meson yields (dn/dy) and the inverse slope parameter T at mid-rapidity in 10% most *central* Ar+Sc collisions. The values are provided with statistical (σ_{stat}) and systematic (σ_{sys}) uncertainties in the form: $(\cdots) \pm \sigma_{\text{stat}} \pm \sigma_{\text{sys}}$.

with respect to $y = 0$:

$$f_{\text{fit}}(y) = \frac{A}{\sigma_0 \sqrt{2\pi}} \left(\exp\left(-\frac{(y-y_0)^2}{2\sigma_0^2}\right) + \exp\left(-\frac{(y+y_0)^2}{2\sigma_0^2}\right) \right) , \qquad (21)$$

where σ_0, y_0, and A are free fit parameters. In the absence of data in the backward hemisphere, a symmetry of amplitudes in the forward and backward hemispheres is assumed.

Figure 27 shows the properties of the parameters fitted to the rapidity distributions of K^+ and K^- at six beam momenta. A smooth evolution of the fit parameters is observed and both σ_0 and y_0 increase towards higher beam momenta.

To obtain the full phase space (4π) mean kaon multiplicity, the measured $\frac{dn}{dy}$ spectra are supplemented with extrapolated yields by integration of the fitted function (Eq. 21) in the unmeasured region. The mean multiplicities of K^+ and K^- calculated at each beam momentum and their respective ratios to mean multiplicities of charged pions are listed in Table 7.

p_{beam} (GeV/c)	K^+/π^+ at $y\approx0$	K^-/π^- at $y\approx0$
13A	$0.1320 \pm 0.0034 \pm 0.0077$	$0.0319 \pm 0.0018 \pm 0.0032$
19A	$0.1451 \pm 0.0045 \pm 0.0037$	$0.0446 \pm 0.0016 \pm 0.0021$
30A	$0.1397 \pm 0.0021 \pm 0.0027$	$0.0520 \pm 0.0009 \pm 0.0010$
40A	$0.1445 \pm 0.0021 \pm 0.0047$	$0.0626 \pm 0.0009 \pm 0.0013$
75A	$0.1569 \pm 0.0016 \pm 0.0051$	$0.0804 \pm 0.0006 \pm 0.0017$
150A	$0.1566 \pm 0.0017 \pm 0.0061$	$0.0983 \pm 0.0009 \pm 0.0025$

Table 6: Ratios of K^+/π^+ and K^-/π^- yields at mid-rapidity in 10% most *central* Ar+Sc collisions. The values are provided with statistical (σ_{stat}) and systematic (σ_{sys}) uncertainties in the form: $K/\pi \pm \sigma_{\text{stat}} \pm \sigma_{\text{sys}}$. The π^+ and π^- yields at mid-rapidity are both taken as the π^- yield measured with the h^- method [17], scaled appropriately (see text for details).
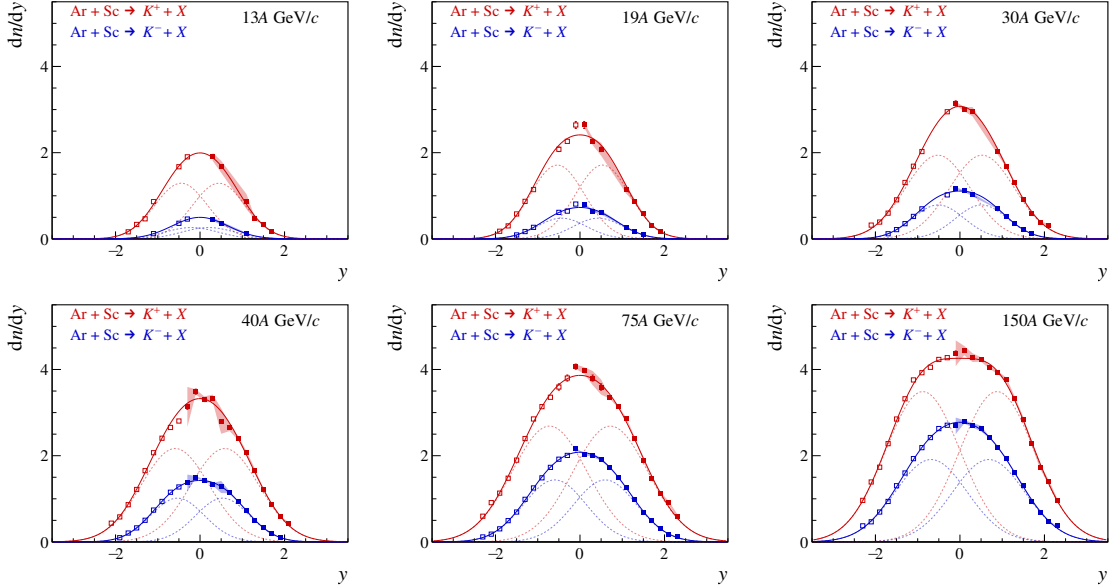
Figure 26: Rapidity distributions of K^+ and K^- in 10% most *central* Ar+Sc collision at 13A–150A GeV/c beam momenta. Data points are plotted along with double-Gaussian fits (Eq. 21). The vertical bars represent statistical uncertainties and the shaded bands stand for the systematic uncertainties. Open markers represent data reflected wrt. $y = 0$.

p_{beam} (GeV/c)	$\langle K^+\rangle$	$\langle K^-\rangle$	$\langle K^+\rangle/\langle \pi^+\rangle$	$\langle K^-\rangle/\langle \pi^-\rangle$
13	$4.03 \pm 0.11 \pm 0.24$	$0.82 \pm 0.03 \pm 0.05$	$0.110 \pm 0.003 \pm 0.021$	$0.022 \pm 0.001 \pm 0.004$
19	$5.48 \pm 0.12 \pm 0.27$	$1.42 \pm 0.06 \pm 0.07$	$0.117 \pm 0.003 \pm 0.012$	$0.030 \pm 0.001 \pm 0.003$
30	$7.48 \pm 0.08 \pm 0.29$	$2.42 \pm 0.04 \pm 0.09$	$0.125 \pm 0.001 \pm 0.011$	$0.040 \pm 0.001 \pm 0.004$
40	$8.77 \pm 0.09 \pm 0.41$	$3.25 \pm 0.04 \pm 0.15$	$0.132 \pm 0.001 \pm 0.012$	$0.049 \pm 0.001 \pm 0.004$
75	$12.01 \pm 0.20 \pm 0.42$	$5.35 \pm 0.04 \pm 0.15$	$0.141 \pm 0.002 \pm 0.011$	$0.063 \pm 0.001 \pm 0.005$
150	$15.52 \pm 0.19 \pm 0.55$	$8.17 \pm 0.07 \pm 0.28$	$0.145 \pm 0.002 \pm 0.017$	$0.076 \pm 0.001 \pm 0.009$

Table 7: Charged kaon mean multiplicities in 10% most *central* Ar+Sc collisions, together with $\langle K^+\rangle/\langle \pi^+\rangle$ and $\langle K^-\rangle/\langle \pi^-\rangle$ ratios. The values are provided with statistical (σ_{stat}) and systematic (σ_{sys}) uncertainties in the form: $(\cdots) \pm \sigma_{\text{stat}} \pm \sigma_{\text{sys}}$.
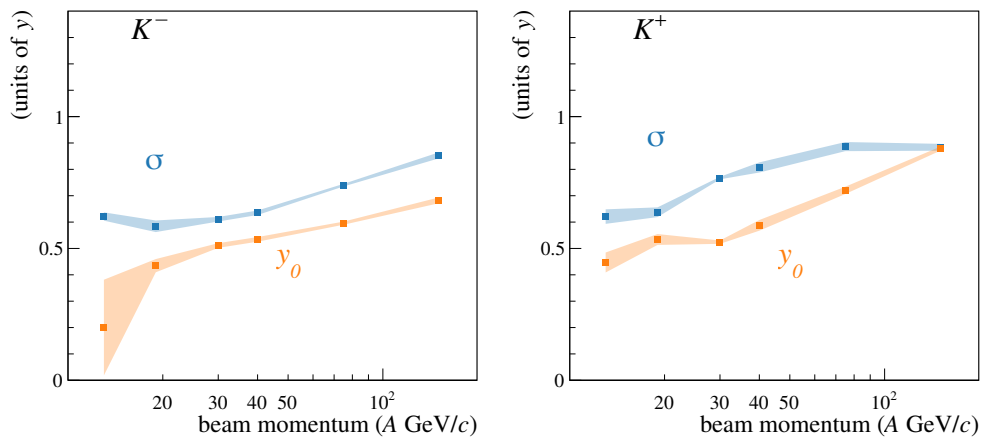
Figure 27: The parameters of the double-Gaussian fit to the charged kaon rapidity spectra in the 10% most *central* Ar+Sc collisions as a function of beam momentum. Both the width (σ_0) and the distance between the peaks (y_0) increase with increasing beam momentum. The shaded bands illustrate fit uncertainties. See text for details and exact fitting model formula. The shaded bands represent the total fit uncertainty.
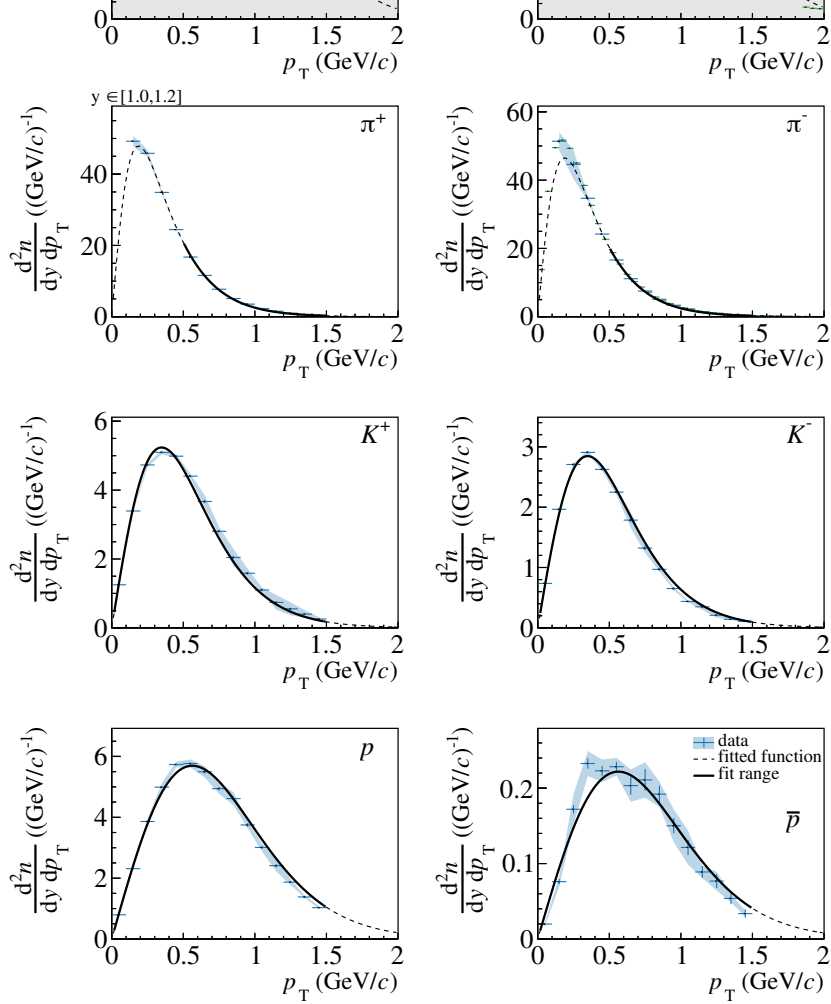
Figure 28: Example fits to transverse momentum spectra of protons and anti-protons in 10% most *central* Ar+Sc collisions (*top*: $p_{beam} = 30A$ GeV/c at $-0.2 < y < 0.0$ and *bottom*: $p_{beam} = 150A$ GeV/c at $1.0 < y < 1.2$). The fitted functions are used to extrapolate the yields beyond $p_T = 1.5$ GeV/c and interpolate the yields in case a gap in acceptance appears due to different coverage of PID methods. Error bars show statistical uncertainties, while shaded bands correspond to systematic uncertainties. The thick solid black line illustrates the region at which the fit was performed and the dashed black line shows the interpolated and extrapolated parts of the spectrum. The vertical bars represent statistical uncertainties and the shaded bands stand for the systematic uncertainties.

Figure 16 illustrates the spectra in rapidity and transverse momentum ($d^2n/(dy\,dp_T)$) of protons and anti-protons at 13A-150A GeV/c and 30A-150A GeV/c, respectively. Similarly as in the case of K mesons, in order to obtain proton and anti-proton dn/dy yields, the data is extrapolated in p_T to account for unmeasured regions of transverse momentum. Due to the effects of radial flow (and possibly other effects), proton spectra cannot be described by an exponential function. Thus, to assure a good description of the measured data, the blastwave model [41] is fitted to p_T spectra of all identified hadrons (p, K^+, π^+ for the positive charge and $\bar{p}$, K^-, π^- for the negative charge). Another advantage of using the blastwave model comes from the additional constraints of the fit from other particle species, which allows for obtaining a reliable fit even with limited acceptance. Example fits are shown in Fig. 28. The dn/dy yield of protons and anti-protons at mid-rapidity is obtained in the same way as described for kaons in the previous section. The resulting yields of p and $\bar{p}$, together with statistical and systematic uncertainties, are summarised in Table 8.

p_{beam} (GeV/c)	$\left(\frac{\mathrm{d}n}{\mathrm{d}y}\right)_{y\approx0}(p)$	$\left(\frac{\mathrm{d}n}{\mathrm{d}y}\right)_{y\approx0}(\bar{p})$
13A	$12.17 \pm 0.15 \pm 0.66$	-
19A	$10.33 \pm 0.14 \pm 0.48$	-
30A	$7.70 \pm 0.07 \pm 0.14$	$0.081 \pm 0.003 \pm 0.022$
40A	$6.84 \pm 0.07 \pm 0.09$	$0.114 \pm 0.004 \pm 0.032$
75A	$5.02 \pm 0.03 \pm 0.12$	$0.251 \pm 0.006 \pm 0.070$
150A	$4.79 \pm 0.04 \pm 0.45$	$0.51 \pm 0.01 \pm 0.14$

Table 8: Numerical values of proton and anti-proton yields (dn/dy) at mid-rapidity in 10% most *central* Ar+Sc collisions. The values are provided with statistical (σ_{stat}) and systematic (σ_{sys}) uncertainties in the form: dn/d$y \pm \sigma_{\text{stat}} \pm \sigma_{\text{sys}}$.

4.3.2 Rapidity spectra

Rapidity distributions are obtained through integration of the double differential spectra in p_{T} at each bin of y and by an addition of extrapolated yields in unmeasured regions. An additional contribution to the systematic uncertainty of 25% of the extrapolated yield is added to account for a possible bias due to the choice of the fit function. Figure 29 shows the proton and antiproton rapidity distributions for each of the analysed collision energies. Contrarily to the well-understood two-Gaussian extrapolation of charged pions and kaons rapidity spectra, a similar procedure cannot be employed here. The shape of proton rapidity distributions changes significantly with beam momentum and the unmeasured regions, containing the maxima, constitute a significant portion of total multiplicity. Thus, the calculation of mean multiplicity was not attempted for protons.

4.3.3 Antiproton mean multiplicities

Mean antiproton multiplicities (4π) were calculated in a similar way as in the case of charged kaons. The measured dn/dy spectra were supplemented for the missing acceptance with integral of the symmetric double Gaussian (Eq. 21) fitted to the data. The assumption of symmetry was necessary due to large uncertainties and limited acceptance of the data in the backward hemisphere. The comparison with models in Sec. 5.5.3 validates this assumption. Figure 30 illustrates both the measured data and the fitted model. The $\bar{p}$ mean multiplicities calculated at each beam momentum are given in Table 9.

p_{beam} (GeV/c)	$\langle\bar{p}\rangle$
30A	$0.119 \pm 0.004 \pm 0.009$
40A	$0.206 \pm 0.008 \pm 0.013$
75A	$0.510 \pm 0.010 \pm 0.026$
150A	$1.090 \pm 0.017 \pm 0.047$

Table 9: Mean multiplicities of antiprotons produced in 10% most *central* Ar+Sc collisions at 30A-150A GeV/c beam momenta. The values are provided with statistical (σ_{stat}) and systematic (σ_{sys}) uncertainties in the form: $\langle\bar{p}\rangle \pm \sigma_{\text{stat}} \pm \sigma_{\text{sys}}$.
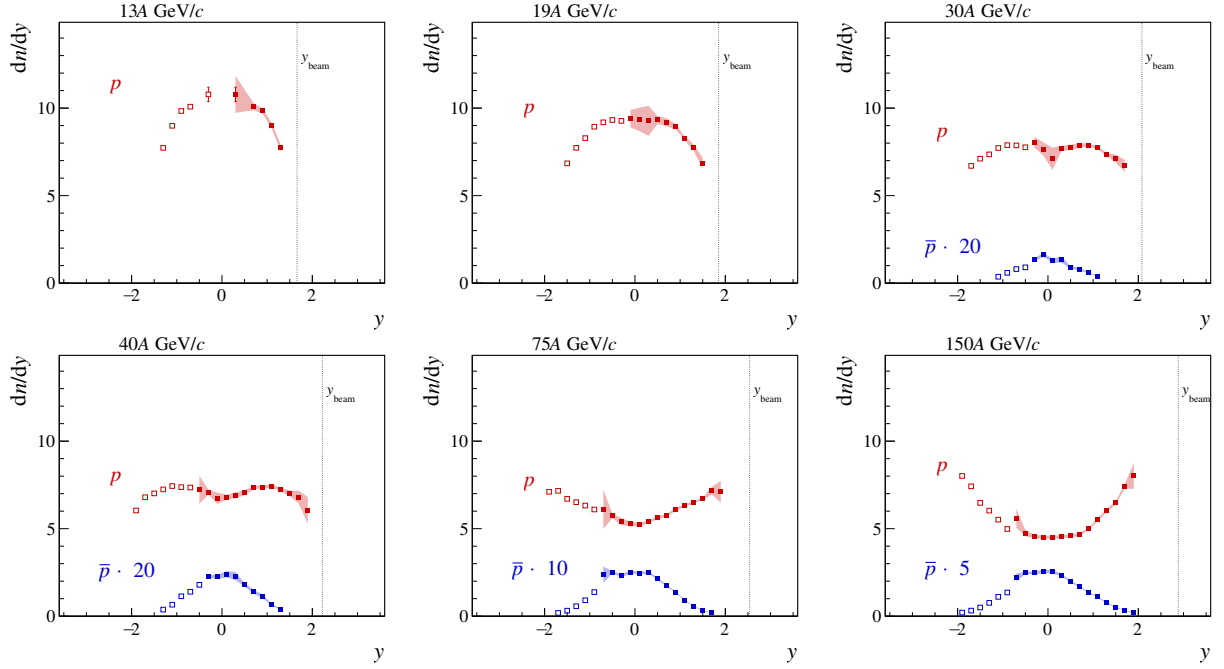
Figure 29: Rapidity spectra of protons and antiprotons produced in 10% most *central* Ar+Sc collisions at 13*A* - 150*A* *GeV*/*c*. No data was plotted for anti-protons produced in collisions at $p_{\text{beam}} = 13A$ and 19*A* GeV/*c* due to large statistical and systematic uncertainties. Error bars show statistical uncertainties, while shaded bands correspond to systematic uncertainties. The open markers represent the data reflected wrt. $y = 0$.
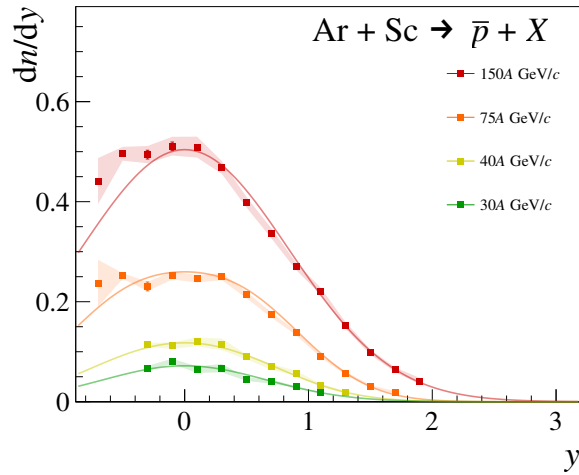

Figure 30: Rapidity distributions of anti-protons measured in 10% most *central* Ar+Sc collisions at 30*A*−150*A* GeV/*c* beam momenta. Data points are plotted along with double-Gaussian fits (Eq. 21). Error bars show statistical uncertainties, while shaded bands correspond to systematic uncertainties.

Similarly as discussed in Sec. 4.2.2, the employed extrapolation procedure results in a systematic uncertainty, that increases with shrinking acceptance towards lower energies. The fraction of measured multiplicity contribution to the total multiplicity varies from over 50% at top SPS collision energy to only ≈10% at 13A GeV/c. This effect, combined with large uncertainties of antiproton dn/dy data prevented the calculation of mean multiplicities at 13A and 19A GeV/c.

5 Collision energy and system size dependence

In this section, the most interesting results on identified hadron production in 10% most *central* Ar+Sc collisions at 13A–150A GeV/c beam momenta are reviewed in the context of signatures of the onset of deconfinement. The energy and system size dependence of hadron production properties are compared with available data on inelastic *p+p* [12–14], *central* Be+Be [15, 16] and *central* Pb+Pb [2, 3] collisions. The remaining world data originate from various experiments at the AGS, SPS, RHIC, and LHC accelerators extracted from Refs. [42–56] and references therein. They concern mostly Pb+Pb and Au+Au collisions.

5.1 K^+ and K^- inverse slope parameter T dependence on collision energy

The simple exponential parametrization of the kaon transverse momentum spectra (Eq. 21) yields values for the inverse slope parameter T, summarized in Table 5. The T values obtained for *central* Ar+Sc collisions at six beam momenta from the CERN SPS energy range as a function of the collision energy ($\sqrt{s_{NN}}$) for positively and negatively charged kaons are presented in Fig. 31. The Ar+Sc values of the T parameter are located slightly below Pb+Pb, yet still significantly higher than Be+Be. The value of the inverse slope parameter within hydrodynamical models is interpreted as a kinetic freeze-out temperature with modifications from transverse flow. In this context, the results presented here may indicate that the kinetic freeze-out temperature and transverse flow in Ar+Sc are closer to Pb+Pb (large system) than Be+Be and *p+p* (small systems).
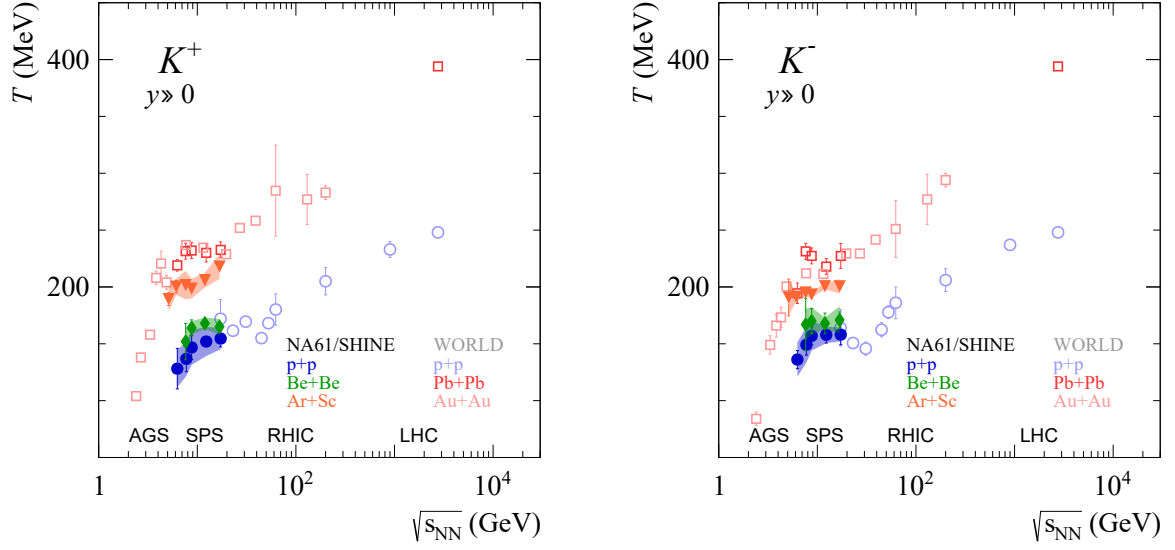
Figure 31: The energy dependence of the inverse slope parameter T of p_T spectra at mid-rapidity of positively (*left*) and negatively (*right*) charged K mesons for central Ar+Sc, Be+Be ([17]), Pb+Pb ([2, 3, 57–59]) and Au+Au ([4, 60–65]) collisions as well as inelastic $p+p$ ([13, 59, 66–68]) interactions. Both statistical (vertical bars) and systematic (shaded bands) uncertainties are shown.

5.2 K/π ratio dependence on collision energy

The characteristic, non-monotonic behavior of the K^+ over π^+ ratio observed in central heavy-ion collisions (see Pb+Pb and Au+Au in Figs. 32 and 33) agrees qualitatively with predictions of SMES [69], in which quarks and gluons are the relevant degrees of freedom in the early stage of the collision at high energies. Within SMES, the sharp peak in the K^+/π^+ ratio (*the horn*) seen at $\sqrt{s_{NN}} \approx 8$ GeV/c is interpreted as an indication of the onset of deconfinement – a beginning of the creation of quark-gluon plasma in the early stage of collision. In the case of intermediate-size systems, however, no such structure is visible, neither at mid-rapidity (Fig. 32) nor in full phase-space (Fig. 33). However, a clear distinction between the two data subsets is visible—$p+p$ and Be+Be results show similar values and collision energy dependence, while the heavy systems of Pb+Pb, Au+Au, and Ar+Sc show much higher K^+/π^+ ratios. Moreover, although Ar+Sc is clearly separated from small systems, its energy dependence does not show the horn seen in Pb+Pb and Au+Au reactions. No available theoretical description agrees with this behavior – neither the models of statistical hadron production in thermal equilibrium nor the microscopic transport models (see discussion in Sec. 5.5).

Figures 32 and 33 display also the energy dependence of K^-/π^- ratio. While the number of s and $\bar{s}$ quarks produced in a collision is equal, their distribution among strange hadrons is heavily affected by the large baryon density, characteristic for ion-ion collisions at SPS energies. The s quarks are distributed predominantly among sparsely produced K^-, $\bar{K}^0$ mesons and Λ baryons, while in the case of $\bar{s}$ quarks, the production of $\bar{\Lambda}$ is heavily suppressed. Thus, the vast majority of $\bar{s}$ quarks are carried out of the collision by K^+ and K^0 mesons, which are produced in similar quantities. Consequently, the K^+ yields are predominantly sensitive to strangeness content, and the K^- production is additionally heavily affected by the baryon density. Therefore, a characteristic maximum close to $\sqrt{s_{NN}} = 8$ GeV, a *horn*, is not expected for the K^-/π^- ratio and all systems studied at SPS energies display an approximately monotonous rise
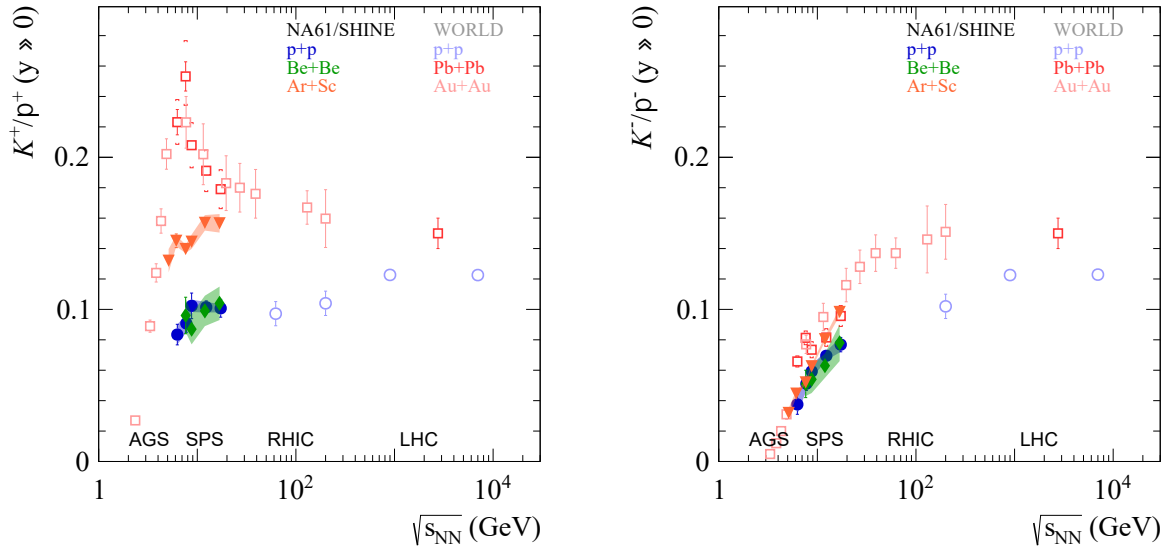
Figure 32: The energy dependence of the K/π ratio at mid-rapidity of positively (*left*) and negatively (*right*) charged particles for central Ar+Sc, Be+Be ([17]), Pb+Pb ([2,3,57–59]) and Au+Au ([4,60–65]) collisions as well as inelastic $p+p$ ([13,59,66–68]) interactions. Both statistical (vertical bars) and systematic (shaded bands) uncertainties are shown.

towards higher collision energies. Similarly to observations made in the previous paragraph, the yields obtained for Ar+Sc interactions closely resemble Pb+Pb data at high collision energies (75A, 150A GeV/c) and at low energies (<40A GeV/c) they are more similar to small systems.
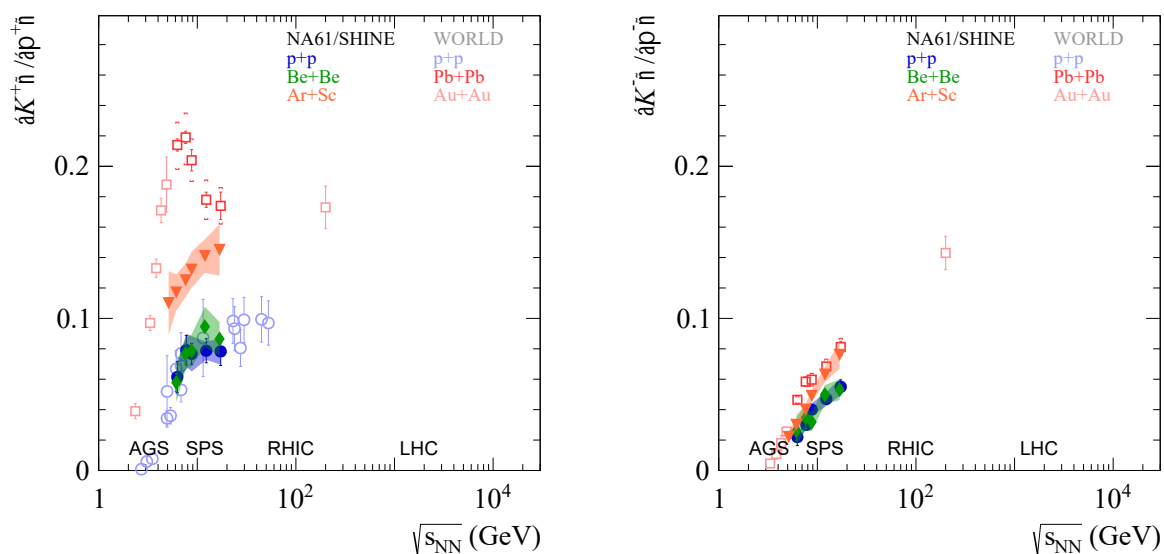
Figure 33: The energy dependence of the $\langle K \rangle / \langle \pi \rangle$ mean multiplicity ratio of positively (*left*) and negatively (*right*) charged particles for central Ar+Sc, Be+Be ([17]), Pb+Pb ([2, 3, 57–59]) and Au+Au ([4, 60–65]) collisions as well as inelastic *p*+*p* ([13, 59, 66–68]) interactions. Both statistical (vertical bars) and systematic (shaded bands) uncertainties are shown.

5.3 Collision energy and system size dependence of proton rapidity spectra

Figure 34 displays proton rapidity spectra in the 10% most *central* Ar+Sc collisions in comparison with reactions of *p*+*p*, Be+Be and Pb+Pb interactions at matching collision energies. At highest collision energies (75A and 150A GeV/c) all reactions show approximately similar shapes of the proton rapidity distribution. At 40A GeV/c an inflection of rapidity spectra is observed in Ar+Sc interactions, which is not the case for small systems. At beam momenta of 150A-158A GeV/c, the spectral shape of Ar+Sc data is similar to results on Pb+Pb collisions, while at 40A GeV/c the Ar+Sc data clearly fit in the overall trend of baryon stopping [70] increasing as a function of system size between Be+Be and Pb+Pb reactions (see Fig. 34). The discussion of proton rapidity spectra in view of phenomenological models is continued in Sec. 5.5.3.

5.4 The onset of QGP fireball

The observed rapid change of hadron production properties that starts when moving from Be+Be to Ar+Sc collisions hints at some non-trivial threshold mechanism. Such system size dependence may be attributed to the beginning of the creation of large clusters of strongly interacting matter – *the onset of QGP fireball* [71]. The similarities of *p*+*p* and Be+Be systems suggest that interactions of these systems could form small non-equilibrium clusters via binary collisions of nucleons, as in the Wounded Nucleon Model [29]. On the other hand, properties of Pb+Pb collisions are well described by statistical and hydrodynamical models, which assume the creation of a collectively evolving fireball in (at least local) thermal equilibrium. Results on Ar+Sc collisions are clearly closer to the Pb+Pb ones than to *p*+*p* and Be+Be measurements, hence *the onset of QGP fireball* may be identified at the system size close to the measured Ar+Sc reaction and may depend on collision energy. Such characteristic system size dependence is seen at multiple
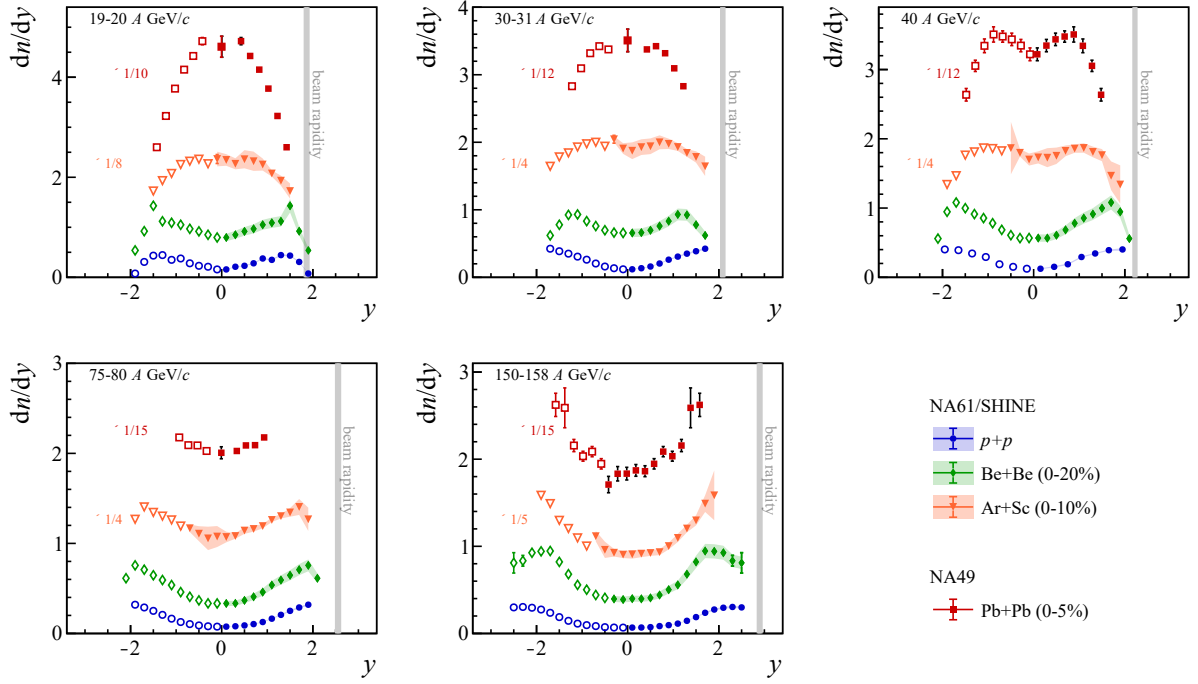
Figure 34: Proton rapidity spectra in 10% most *central* Ar+Sc collisions in comparison with other systems: *p+p*, *central* Be+Be and *central* Pb+Pb at five corresponding collision energies. Full markers denote the experimental points, while open ones plot their reflections with respect to $y = 0$, where there is no corresponding data point. Error bars display statistical uncertainties and shaded bands stand for systematic biases.

measured quantities: mean multiplicities ratios of $\langle K^+\rangle/\langle\pi^+\rangle$ (Fig. 35) and $\langle K^-\rangle/\langle\pi^-\rangle$ (Fig. 37), the ratio of yields at mid-rapidity measurements K^+/π^+ (Fig. 36) and K^-/π^- (Fig. 38), inverse slope parameter T of K^+ (Fig. 39) and K^- (Fig. 40) transverse momentum spectra, and the shapes of proton rapidity spectra (Fig. 34). Additionally, a similar behavior was observed in the studies of mean pion multiplicity per wounded nucleon $\langle\pi\rangle/\langle W\rangle$ published in Ref. [17]. Recent phenomenological interpretations [72] suggest that the diagram of the high-energy nuclear collisions may in fact consist of three main domains in which certain hadron production processes dominate: i) creation, evolution and decay of resonances, ii) formation, evolution and fragmentation of strings, and iii) creation, evolution and hadronization of QGP. Within this picture, the differences observed between the small systems (*p+p*, Be+Be) and Ar+Sc are an interplay of changeovers between these domains. Such interpretation is motivated by comparison with models implementing different hadron production mechanisms, thus this topic is revisited in Sec. 5.5.5.
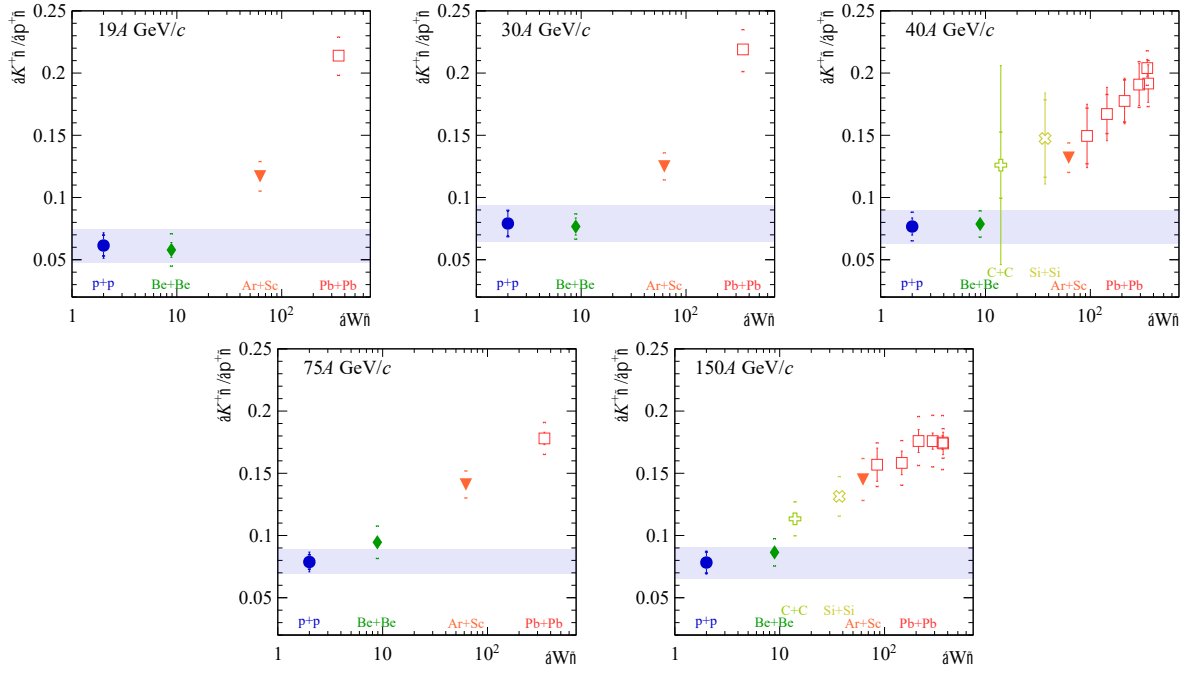
Figure 35: System size dependence of $\langle K^+ \rangle / \langle \pi^+ \rangle$ mean multiplicity ratios measured at 19A-150A GeV/c, showing values for inelastic p+p interactions and central Be+Be, Ar+Sc (this study) and Pb+Pb. Here the system size is represented by the mean number of wounded nucleons ($\langle W \rangle$). Statistical errors are shown as bars and systematic uncertainties are denoted with square braces. The shaded band shows the total uncertainty of the p+p result.
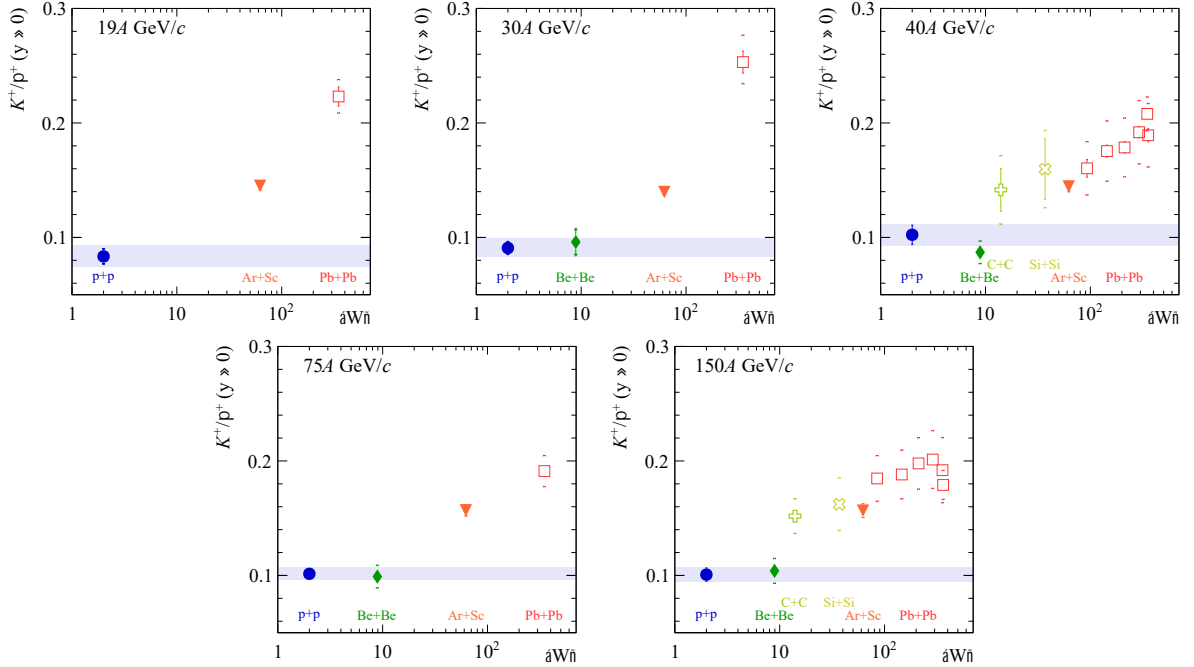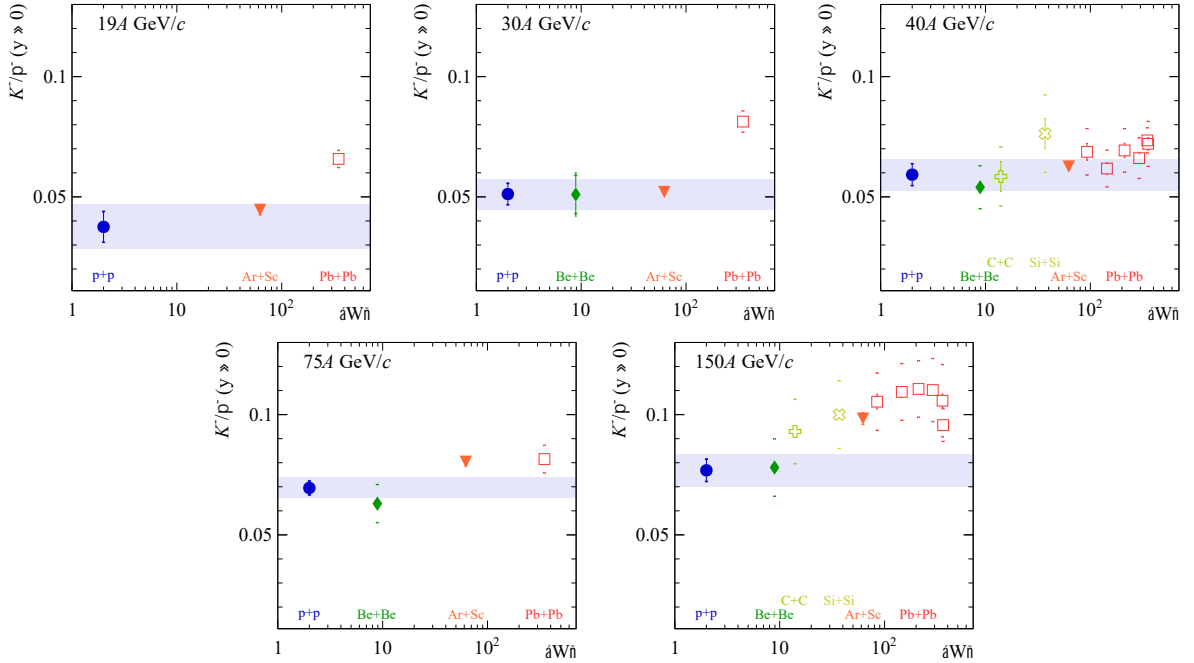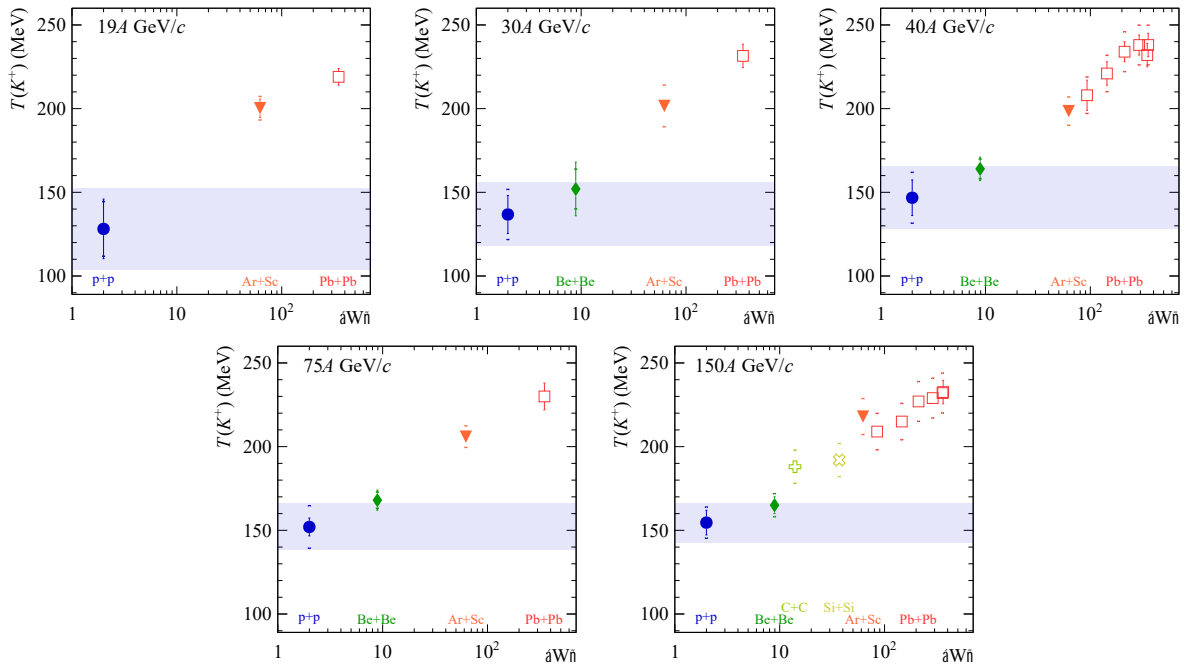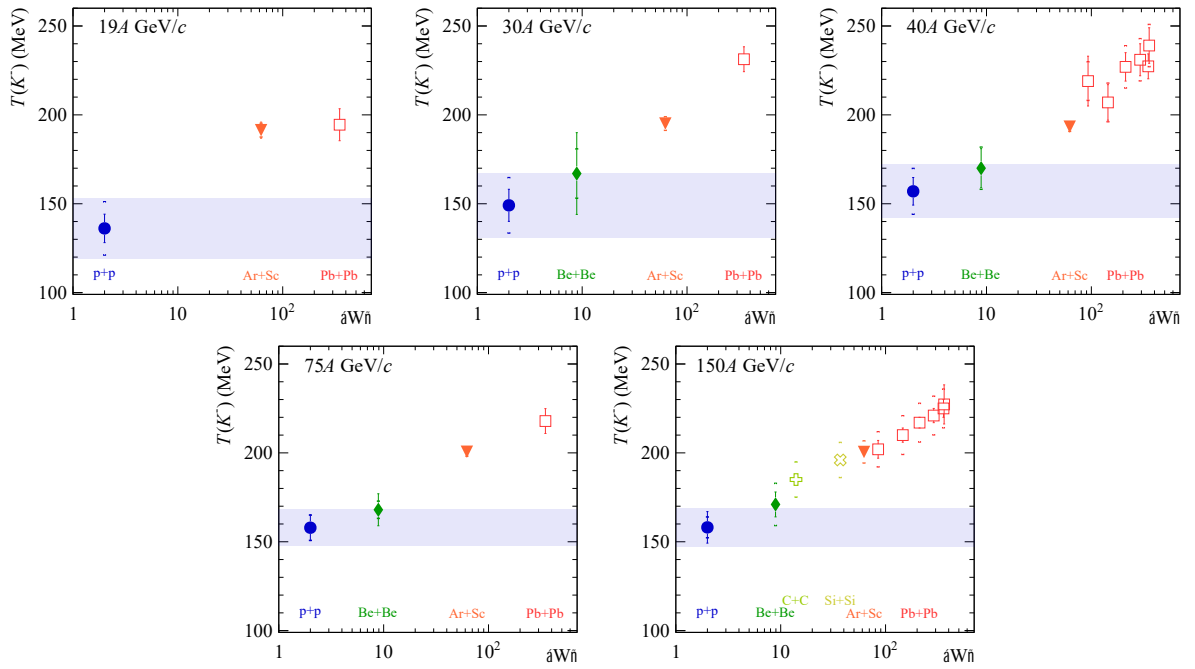

Figure 36: System size dependence of K^+/π^+ ratios at mid-rapidity measured at 19A-150A GeV/c, showing values for inelastic p+p interactions and central Be+Be, Ar+Sc (this study) and Pb+Pb. The system size is represented by the mean number of wounded nucleons ($\langle W \rangle$). Statistical errors are shown as bars and systematic uncertainties are denoted with square braces. The shaded band shows the total uncertainty of the p+p result.
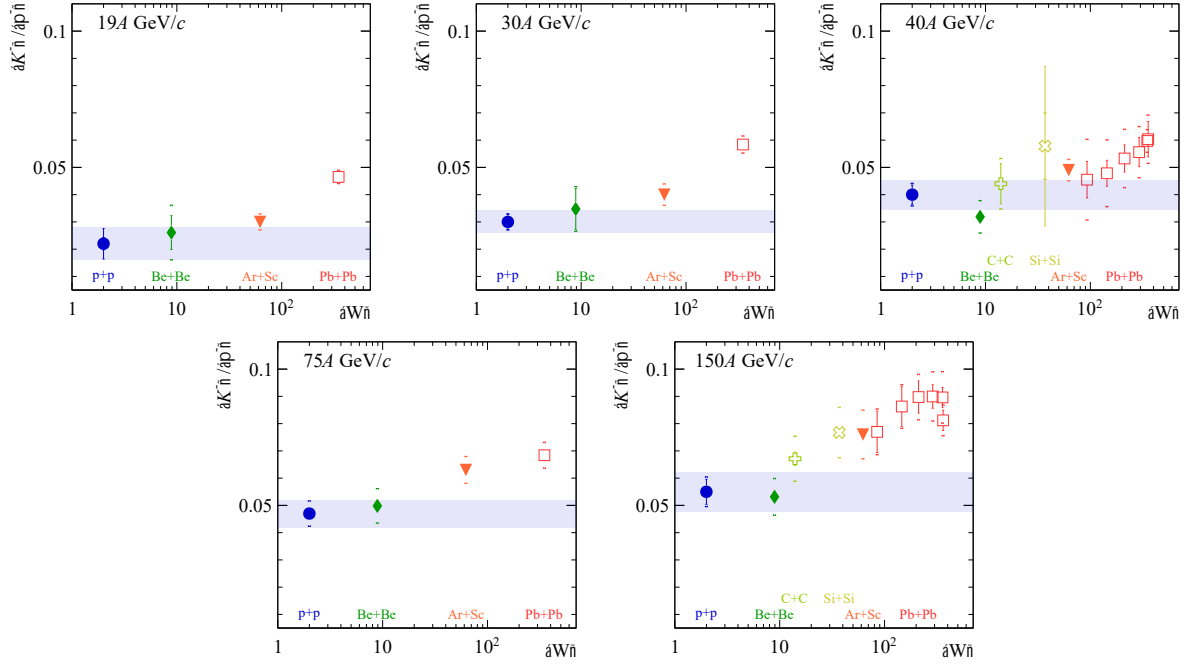
Figure 37: System size dependence of $\langle K^- \rangle / \langle \pi^- \rangle$ mean multiplicity ratios measured at 19A-150A GeV/c, showing values for inelastic p+p interactions and central Be+Be, Ar+Sc (this study) and Pb+Pb. Here the system size is represented by the mean number of wounded nucleons ($\langle W \rangle$). Statistical errors are shown as bars and systematic uncertainties are denoted with square braces. The shaded band shows the total uncertainty of the p+p result.

Figure 38: System size dependence of K^- / π^- ratios at mid-rapidity measured at 19A-150A GeV/c, showing values for inelastic p+p interactions and central Be+Be, Ar+Sc (this study) and Pb+Pb. The system size is represented by the mean number of wounded nucleons ($\langle W \rangle$). Statistical errors are shown as bars and systematic uncertainties are denoted with square braces. The shaded band shows the total uncertainty of the p+p result.

Figure 39: System size dependence of the inverse slope parameter T of K^+ transverse momentum spectra at mid-rapidity measured at $19A$-$150A$ GeV/c, showing values for inelastic p+p interactions and central Be+Be, Ar+Sc (this study) and Pb+Pb. The system size is represented by the mean number of wounded nucleons ($\langle W \rangle$). Statistical errors are shown as bars and systematic uncertainties are denoted with square braces. The shaded band shows the total uncertainty of the p+p result.

Figure 40: System size dependence of the inverse slope parameter T of K^- transverse momentum spectra at mid-rapidity measured at $19A$-$150A$ GeV/c, showing values for inelastic p+p interactions and central Be+Be, Ar+Sc (this study) and Pb+Pb. The system size is represented by the mean number of wounded nucleons ($\langle W \rangle$). Statistical errors are shown as bars and systematic uncertainties are denoted with square braces. The shaded band shows the total uncertainty of the p+p result.

5.5 Comparison with models

This subsection compares experimental results expected to be sensitive to the onset of deconfinement with corresponding model predictions. The EPOS 1.99 [73], PHSD 4.1 [20, 21] and SMASH 2.1.4 [74, 75] models were chosen for this study. In EPOS, the reaction proceeds from the excitation of strings according to Gribov-Regge's theory to string fragmentation into hadrons. PHSD is a microscopic off-shell transport approach that describes the evolution of a relativistic heavy-ion collision from the initial hard scatterings and string formation through the dynamical deconfinement phase transition to the quark-gluon plasma as well as hadronization and the subsequent interactions in the hadronic phase. SMASH uses the hadronic transport approach where the free parameters of the string excitation and decay are tuned to match the experimental measurements in inelastic $p+p$ collisions. The selection of events in all model calculations follows the procedure for *central* collisions to which experimental results correspond, see Sec. 3.1. This is particularly important when comparisons of yields with measurements are to be performed.

5.5.1 Charged pion spectra and multiplicities

Both the shape and the magnitude of π^+ and π^- rapidity spectra in *central* Ar+Sc collisions (Figs. 41 and 42) are relatively well-described by all analyzed models at higher collision energies. The EPOS model overestimates the charged pion yield at $p_{\text{beam}} \leq 40A\,\text{GeV}/c$ and the $\pi^{\pm}$ rapidity spectrum in the SMASH model is narrower than observed in data.

Figure 43 also displays the mean multiplicities confronted with the model predictions, which are typically within a 5–10% spread relative to measured data. The yields calculated with the SMASH model are systematically lower than the experimental points at each collision energy.

A detailed analysis of charged pion production in *central* Ar+Sc collisions in the context of the onset of deconfinement is published in Ref. [17].

5.5.2 Charged kaon spectra and multiplicities

Comparisons of the p_T spectra at mid-rapidity of K^+, K^- mesons in 10% most *central* Ar+Sc collisions at all analyzed beam momenta are shown in Figs. 44 and 45. The peaks in the transverse momentum spectra are at lower p_T values in EPOS and SMASH models relative to the data, which is also reflected in underestimated inverse slope parameter T displayed in Fig. 46. The charged kaon transverse momentum spectra are relatively well described with the PHSD model.

Figure 47 displays the charged kaon dn/dy yields measured at mid-rapidity. None of the models reproduces accurately the collision energy dependence in the whole studied range, however a good agreement is observed between the measured data and the PHSD model in the case of K^+ mesons. The EPOS model agrees well with the data on K^- yields only at $p_{\text{beam}} \leq 40A\,\text{GeV}/c$. The SMASH model underestimates charged hadron yields at all studied collision energies.

The model predictions of the rapidity spectra are shown in Figs. 48 and 49. Similar to previous observations, the SMASH model gives largely lower yields than both data and other investigated models. A relatively good agreement with the measured data is seen for EPOS and PHSD at lower collision energies, however the discrepancies become substantial at 75A and 150A GeV/c, exceeding 15%. Described trends propagate into the collision energy dependence of mean multiplicities, which is displayed in Fig. 50.
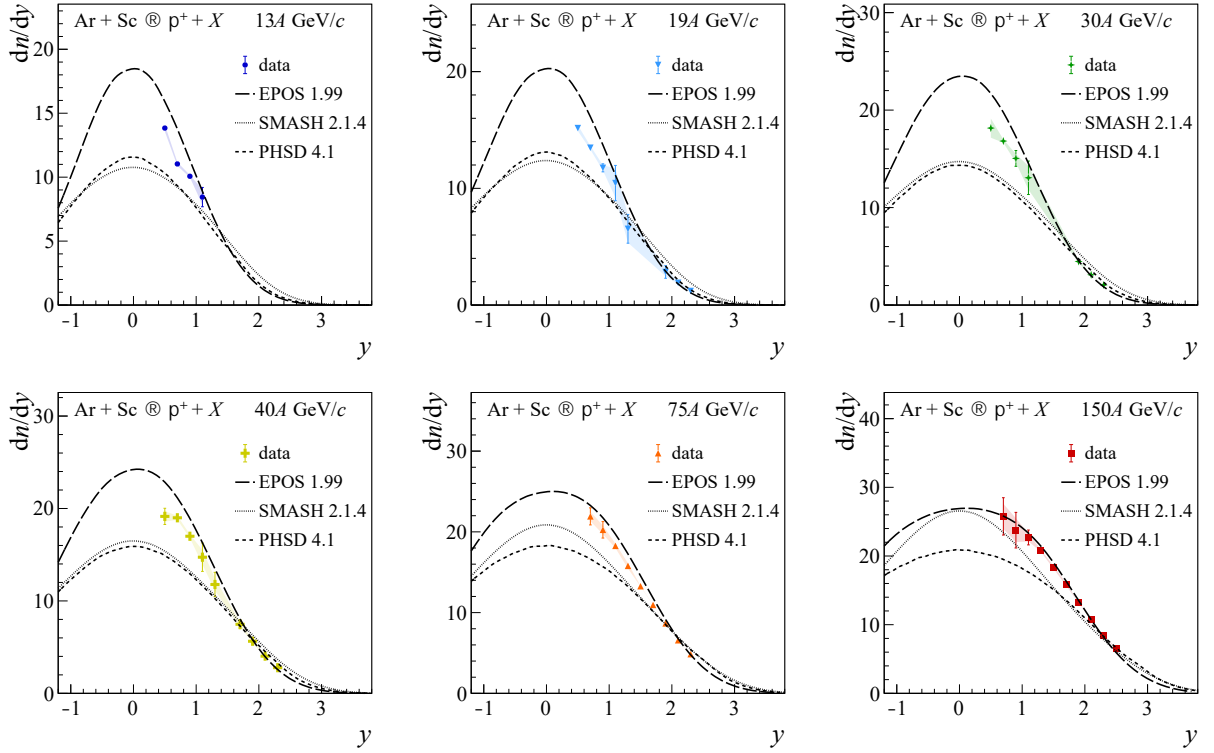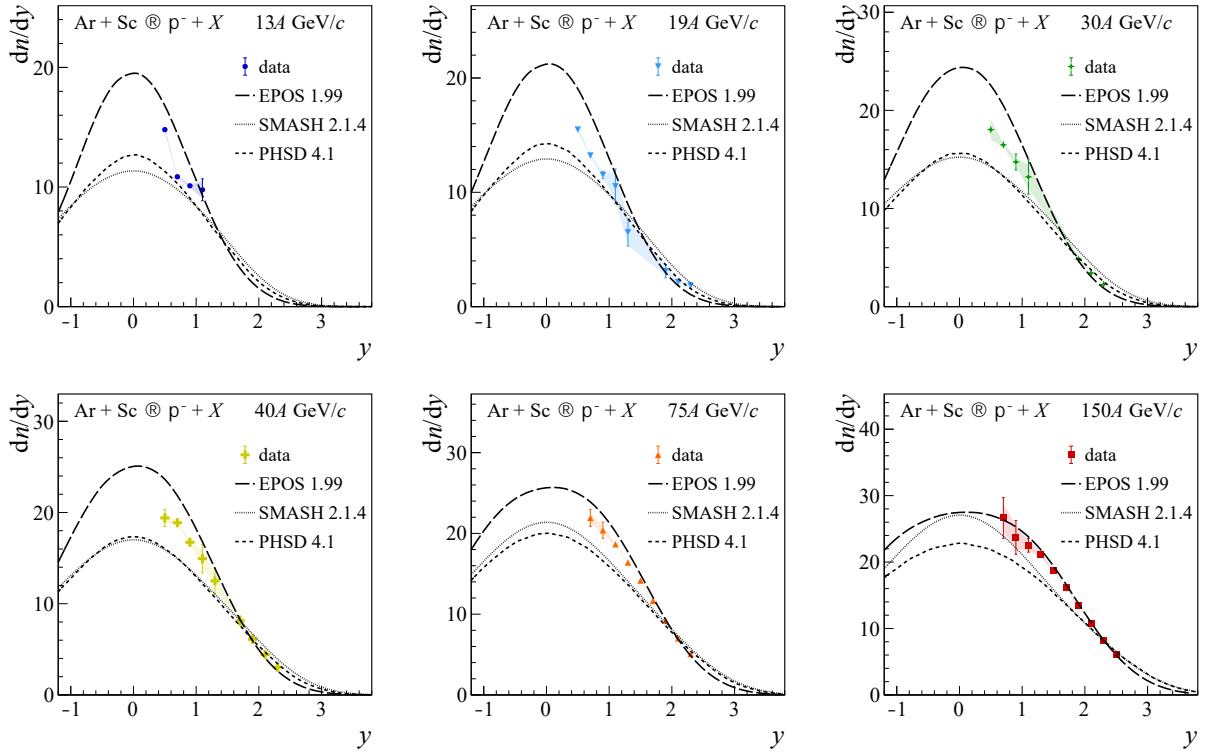
Figure 41: Rapidity spectra of π^+ mesons produced in 10% most *central* Ar+Sc interactions at 13A, 19A, 30A, 40A, 75A and 150A GeV/c in comparison with models: EPOS 1.99 [73], PHSD 4.1 [20, 21] and SMASH 2.1.4 [74, 75].

Finally, the energy dependence of the ratio of kaon and pion yields is compared to model predictions. Figure 51 shows the mid-rapidity results for K^+/π^+, K^-/π^- and K^+/K^- and Fig. 52 displays the corresponding results obtained for the full phase space. Unlike particle yields, particle ratios are not sensitive to the details of the event selection assuming that the shapes of the spectra do not change significantly in the studied centrality range. None of the analyzed models provide a good description of observed K^+/π^+, K^-/π^- ratios in terms of absolute values. With the exception of the PHSD model predictions on K^+/π^+ values, the collision energy dependence is generally well reproduced.

Figure 42: Rapidity spectra of π^- mesons produced in 10% most *central* Ar+Sc interactions at 13A, 19A, 30A, 40A, 75A and 150A GeV/c in comparison with models: EPOS 1.99 [73], PHSD 4.1 [20, 21] and SMASH 2.1.4 [74, 75].
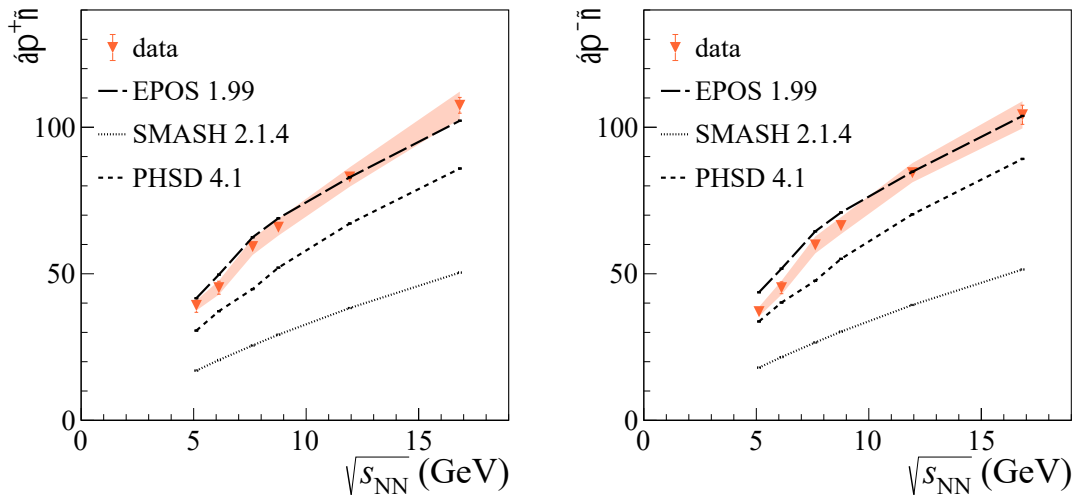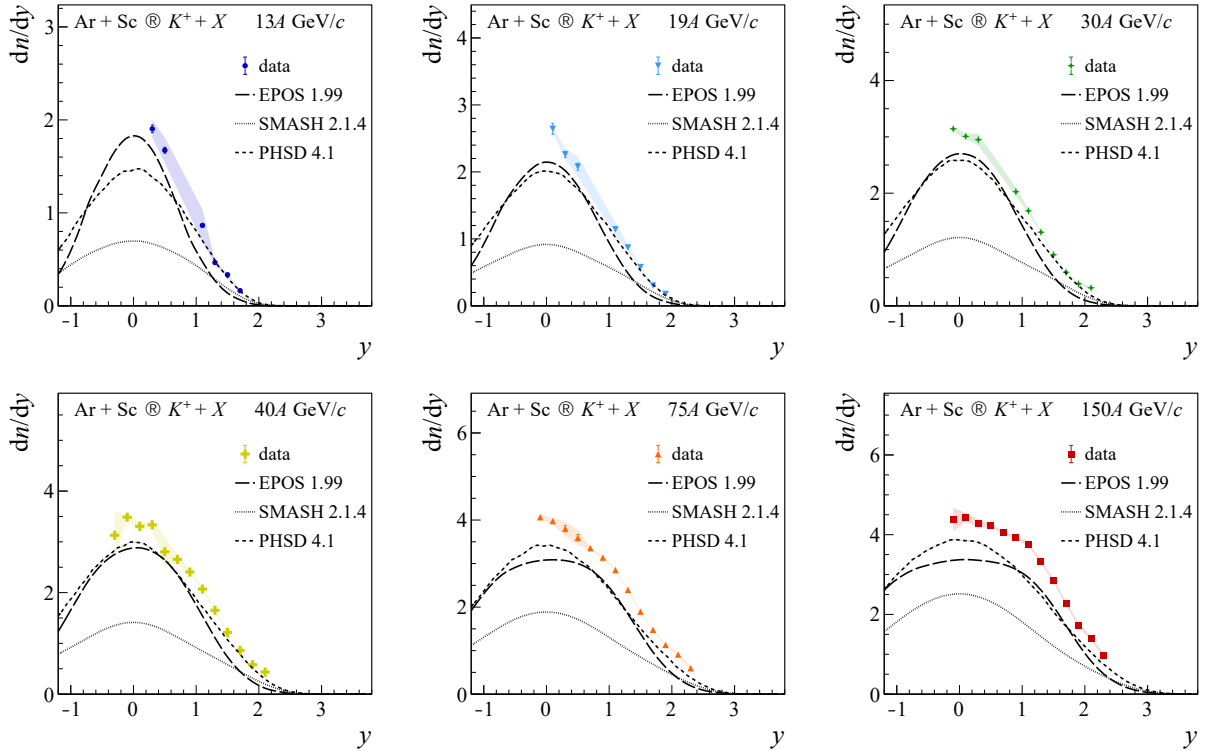

Figure 43: Mean multiplicities of π^+ and π^- mesons produced in 10% most *central* Ar+Sc interactions at 13A, 19A, 30A, 40A, 75A and 150A GeV/c in comparison with models: EPOS 1.99 [73], PHSD 4.1 [20, 21] and SMASH 2.1.4 [74, 75].
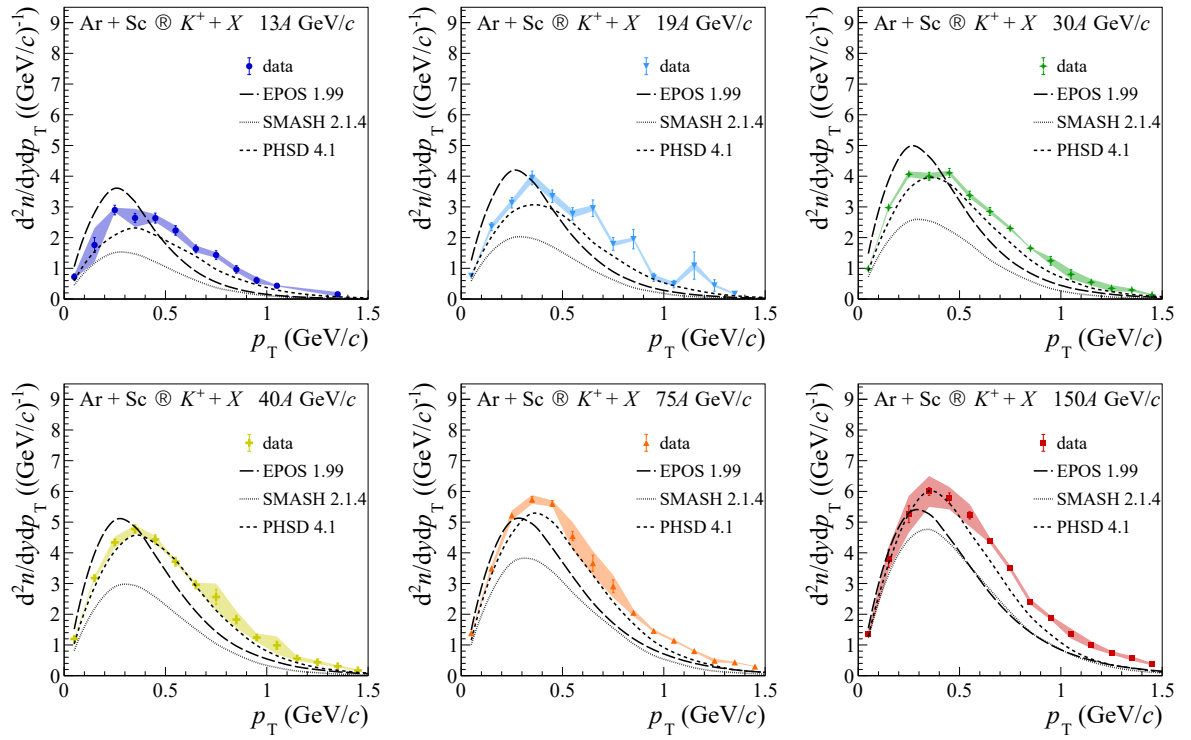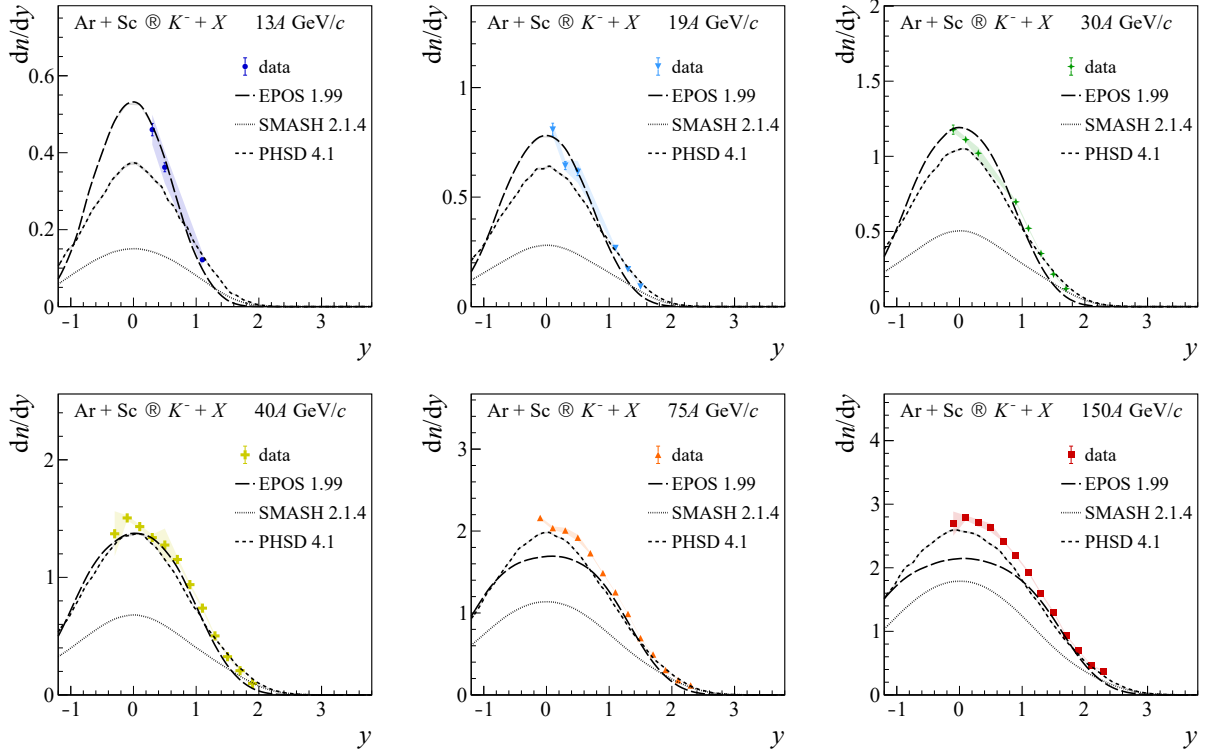
Figure 44: Mid-rapidity transverse momentum spectra of K^+ mesons produced in 10% most *central* Ar+Sc interactions at 13*A*, 19*A*, 30*A*, 40*A*, 75*A* and 150*A* GeV/*c* in comparison with models: EPOS 1.99 [73], PHSD 4.1 [20, 21] and SMASH 2.1.4 [74, 75].
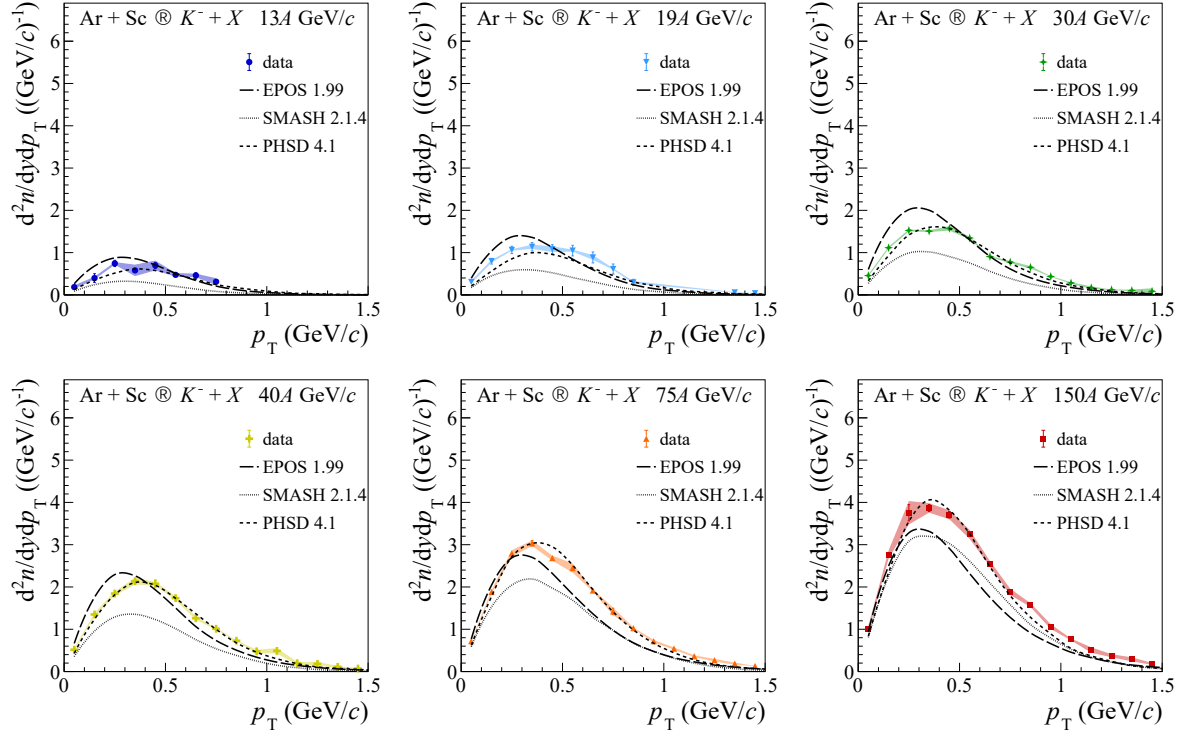
Figure 45: Mid-rapidity transverse momentum spectra of K^+ mesons produced in 10% most *central* Ar+Sc interactions at 13*A*, 19*A*, 30*A*, 40*A*, 75*A* and 150*A* GeV/*c* in comparison with models: EPOS 1.99 [73], PHSD 4.1 [20, 21] and SMASH 2.1.4 [74, 75].
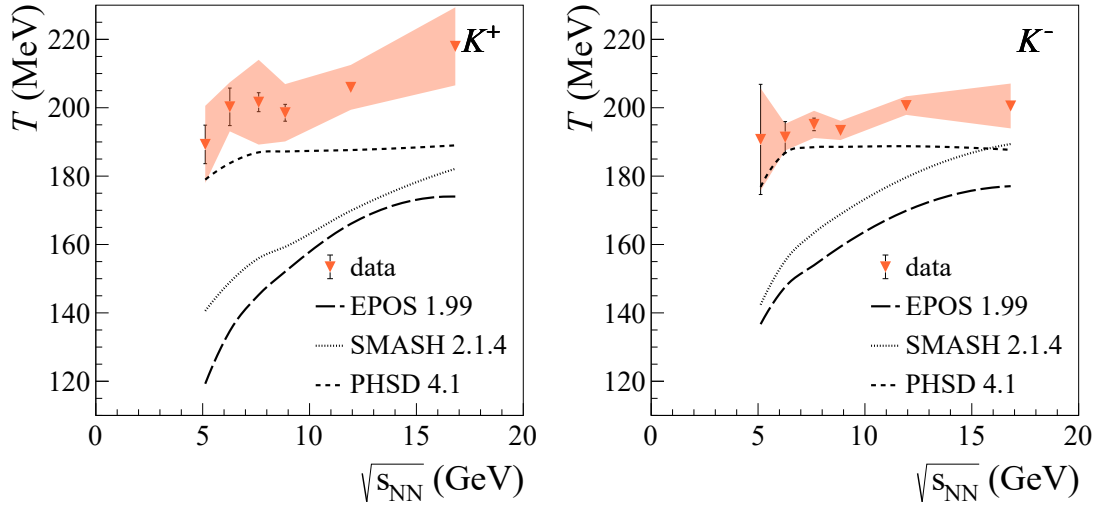
Figure 46: Inverse slope parameter of mid-rapidity transverse momentum spectra of K^+ and K^- produced in 10% most *central* Ar+Sc interactions at 13*A*, 19*A*, 30*A*, 40*A*, 75*A* and 150*A* GeV/*c* in comparison with models: EPOS 1.99 [73], PHSD 4.1 [20, 21] and SMASH 2.1.4 [74, 75].
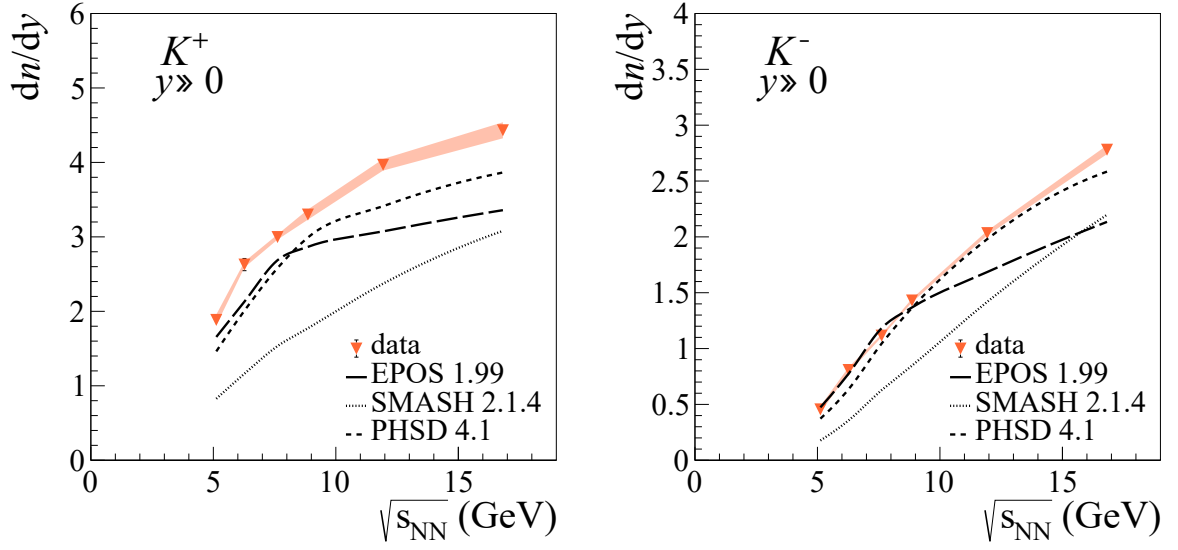
Figure 47: Mid-rapidity dn/dy yields of K^+ and K^- mesons produced in 10% most *central* Ar+Sc interactions at $13A$, $19A$, $30A$, $40A$, $75A$ and $150A$ GeV/c in comparison with models: EPOS 1.99 [73], PHSD 4.1 [20, 21] and SMASH 2.1.4 [74, 75].

Figure 48: Rapidity spectra of K^+ mesons produced in 10% most *central* Ar+Sc interactions at $13A$, $19A$, $30A$, $40A$, $75A$ and $150A$ GeV/c in comparison with models: EPOS 1.99 [73], PHSD 4.1 [20, 21] and SMASH 2.1.4 [74, 75].

Figure 49: Rapidity spectra of K^- mesons produced in 10% most *central* Ar+Sc interactions at 13A, 19A, 30A, 40A, 75A and 150A GeV/c in comparison with models: EPOS 1.99 [73], PHSD 4.1 [20, 21] and SMASH 2.1.4 [74, 75].
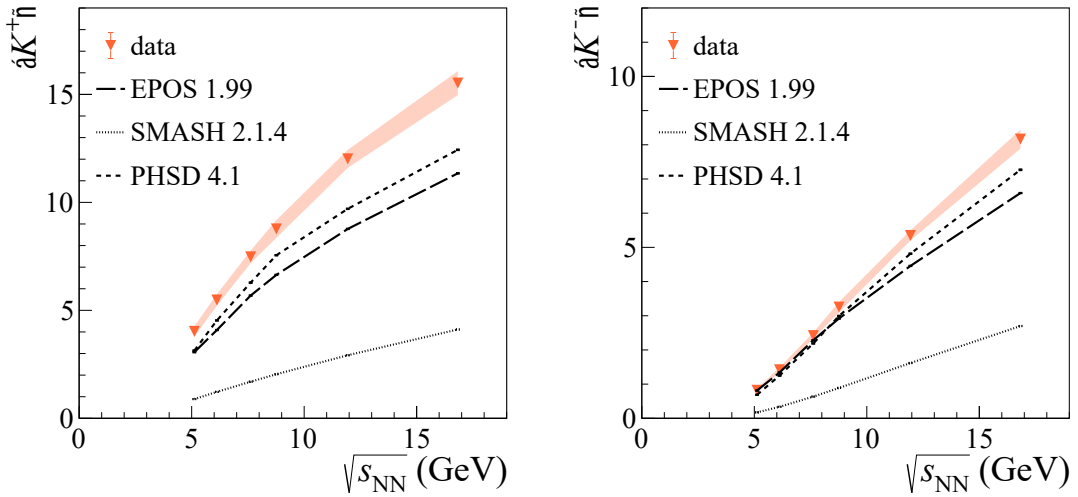
Figure 50: Mean multiplicities of charged kaons ($\langle K^+ \rangle$ and $\langle K^- \rangle$) produced in 10% most *central* Ar+Sc interactions at 13A, 19A, 30A, 40A, 75A and 150A GeV/c plotted in dependence on collision energy compared with models: EPOS 1.99 [73], PHSD 4.1 [20, 21] and SMASH 2.1.4 [74, 75].

54
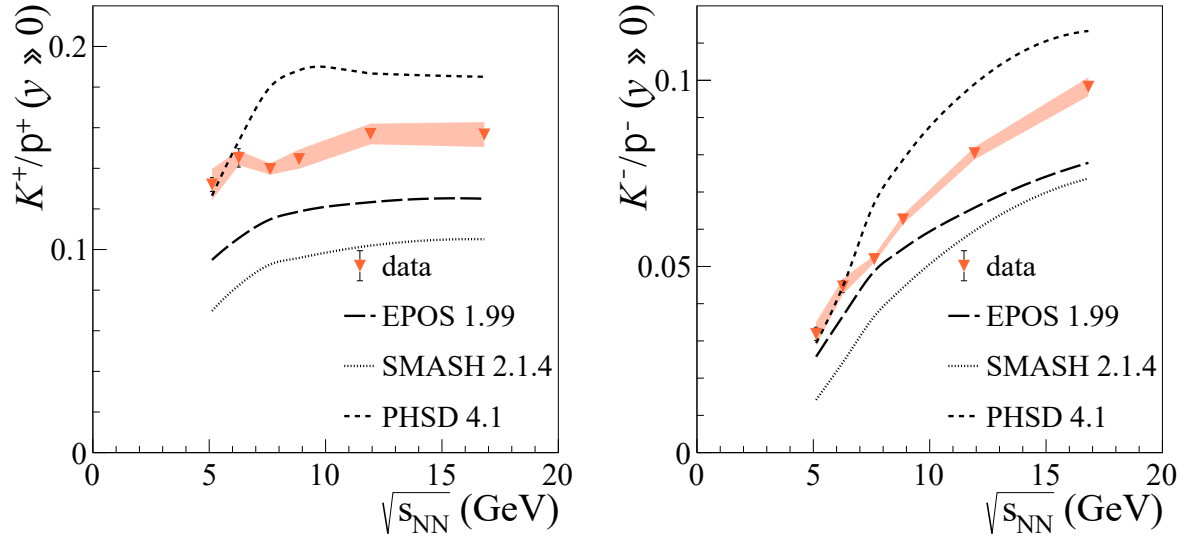
Figure 51: The ratios of dn/dy yields at mid-rapidity K^+/π^+ and K^-/π^- produced in 10% most *central* Ar+Sc interactions at 13A, 19A, 30A, 40A, 75A and 150A GeV/c plotted in dependence on collision energy compared with models: EPOS 1.99 [73], PHSD 4.1 [20, 21] and SMASH 2.1.4 [74, 75].
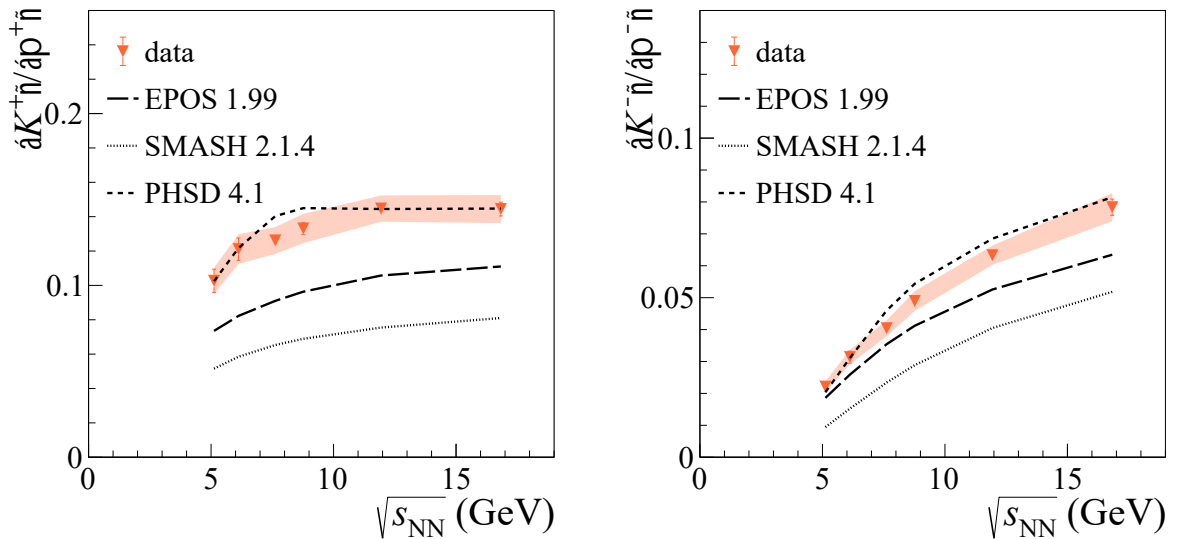
Figure 52: The ratios of mean multiplicity $\langle K^+ \rangle / \langle \pi^+ \rangle$ and $\langle K^- \rangle / \langle \pi^- \rangle$ produced in 10% most *central* Ar+Sc interactions at 13A, 19A, 30A, 40A, 75A and 150A GeV/c in dependence on collision energy compared with models: EPOS 1.99 [73], PHSD 4.1 [20, 21] and SMASH 2.1.4 [74, 75].

5.5.3 Proton and antiproton spectra

Figures 53 and 54 display a comparison with model predictions of p and $\bar{p}$ transverse momentum distributions at mid-rapidity. The general trend observed for all beam momenta is a maximum at higher p_T values than expected from Epos and Smash models, while Phsd describes the measured spectra shape much better.

Figures 55 and 56 show p and $\bar{p}$ rapidity distributions compared with model predictions. Note that the discussed measurements of proton spectra do not cover the so-called "diffractive region", which features a characteristic peak structure, observed experimentally in p+p reactions [76]. The Phsd model provides the best description of proton and antiproton rapidity spectra, in particular at lower collision energies. At $75A$ and $150A$ GeV/c, the antiproton yield is significantly underestimated and the proton rapidity spectrum aligns with data only close to mid-rapidity. The Epos model generally underestimates the yields of protons and overestimates the yield of antiprotons, while the Smash model's relation to measured data is exactly the opposite.

The properties of proton rapidity distributions may be sensitive to the changes in the equation of state. In particular, a scenario of first-order phase transition features a characteristic concave-convex interchange ("peaks" and "dips") in the central part of the proton rapidity spectrum in dependence on collision energy [77].

With the data presented here, we observe that at the beam momenta of $13A$ and $19A$ GeV/c the proton rapidity spectrum features a global maximum at mid-rapidity, while starting from $30A$–$40A$ GeV/c a local minimum appears at $y = 0$. Such observations are not consistent with either the hadronic or double-phase equation of state within the framework presented in Ref. [77].

Notably, the Epos and Phsd models describe well the concave shape of the spectra at $13A$, the flattening at $19A$ and $30A$ GeV/c, as well as the convex characteristic of the distributions at higher beam momenta.

5.5.4 System size dependence of the K^+/π^+ ratio

Figure 57 presents the K^+/π^+ multiplicity ratio as a function of the system size for the highest SPS energy ($\sqrt{s_{NN}} \approx 17$ GeV, $150A$ GeV/c beam momentum). System size is quantified by the mean number of wounded nucleons in collisions $\langle W \rangle$. Dynamical models (Epos [73], UrQMD [78,79] and Smash [74,75]) successfully describe the K^+/π^+ ratio for light systems (p+p and Be+Be) but fail for heavier ones (Ar+Sc, Pb+Pb). On the other hand, PHSD, the model with phase transition, reproduces the data for heavy systems but overestimates the K^+/π^+ ratio for lighter ones. The statistical hadron resonance gas model (HRG, [19]) significantly overestimates the ratio for light systems. The overestimation for heavier systems is still present but is less pronounced.

5.5.5 Summary on model predictions

The comparison of measured data on Ar+Sc collisions at $p_{beam} = 13A - 150A$ GeV/c with the dynamical models of heavy-ion collisions (Epos, Smash, Phsd) provides interesting insights into the challenges of understanding the dynamics of intermediate-size system collisions. The charged-pion rapidity spectra are relatively well described by all analyzed models at high beam momenta ($75A$, $150A$ GeV/c), where overall deviations do not exceed 10%. Larger discrepancies appear at lower collision energies. The dn/dy
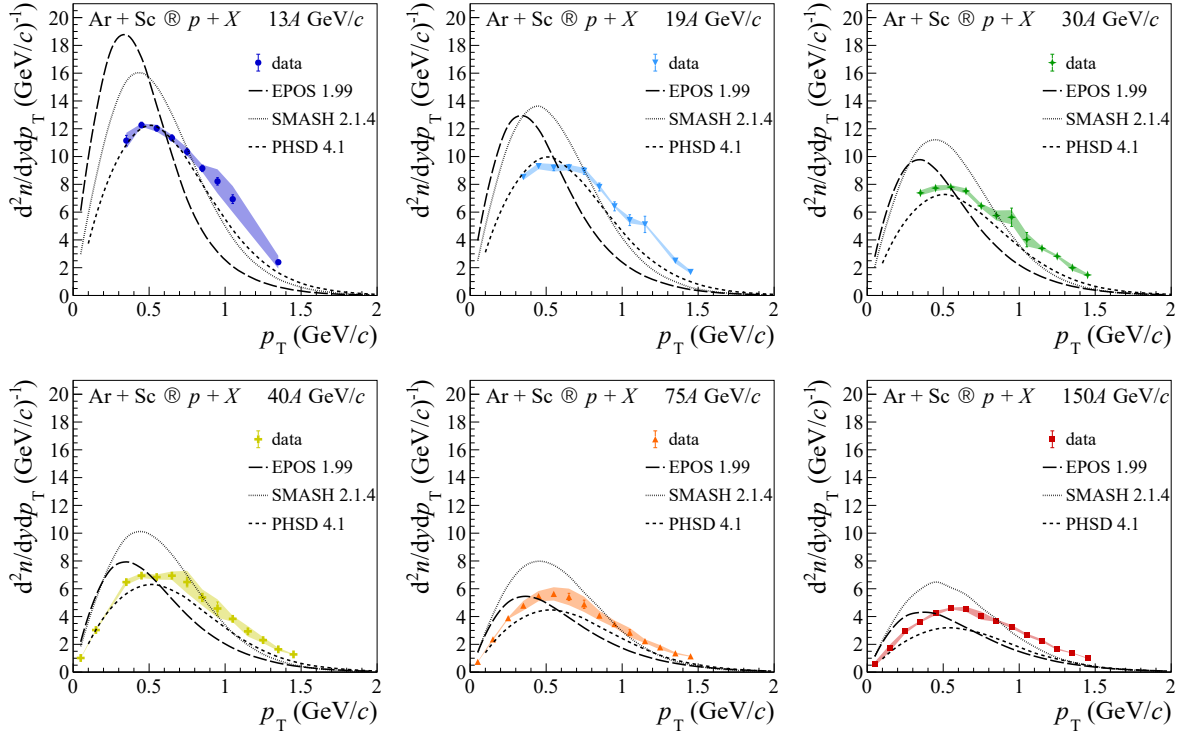
Figure 53: Transverse momentum distributions of protons at mid-rapidity produced in 10% most *central* Ar+Sc interactions at 13*A*, 19*A*, 30*A*, 40*A*, 75*A* and 150*A* GeV/*c* compared with models: EPOS 1.99 [73], PHSD 4.1 [20, 21] and SMASH 2.1.4 [74, 75].

yields of charged kaons are, in general, poorly described by the models. However, a good description of the K^+ yields is observed in the case of PHSD. Particularly interesting are the rapidity spectra of protons, which feature an inflection point at mid-rapidity—from convex to concave shape—with increasing collision energy. Both EPOS and PHSD display similar behavior, while the spectra shapes in SMASH are qualitatively different at 13*A* and 19*A* GeV/*c*. The PHSD model predictions concerning charged kaon, proton, and antiproton transverse momentum spectra are in good agreement with measured data. It is in contrast to EPOS and SMASH models, which feature a shift of transverse momentum distribution peaks towards lower values of p_T, which may be attributed to unimplemented effects of radial flow. The collision energy dependence of K^+/π^+ ratio is not well reproduced by any of the analyzed models and a similar statement is true in the case of K^-/π^- ratio.

The most interesting observable, in the context of this article, is the system size dependence of the K^+/π^+ ratio. For the comparison with the models, data on $p+p$, Be+Be, Ar+Sc and Pb+Pb collisions at $\sqrt{s_{NN}} \approx 17$ GeV are selected. Neither the dynamical nor statistical models describe a rapid change of the K^+/π^+ ratio between *central* Be+Be and Ar+Sc collisions at the highest SPS energy, as it can be seen in Fig. 57.

It is apparent that the influence of the system size on particle production and strangeness production, in particular, is not well understood and requires more theoretical and phenomenological studies. The models analyzed in this work implement different particle creation mechanisms. The widely used approach is modeling collisions via the formation and fragmentation of parton-strings. Such a mechanism is utilized in all three discussed dynamical models, however, at low collision energies, the applicability of this
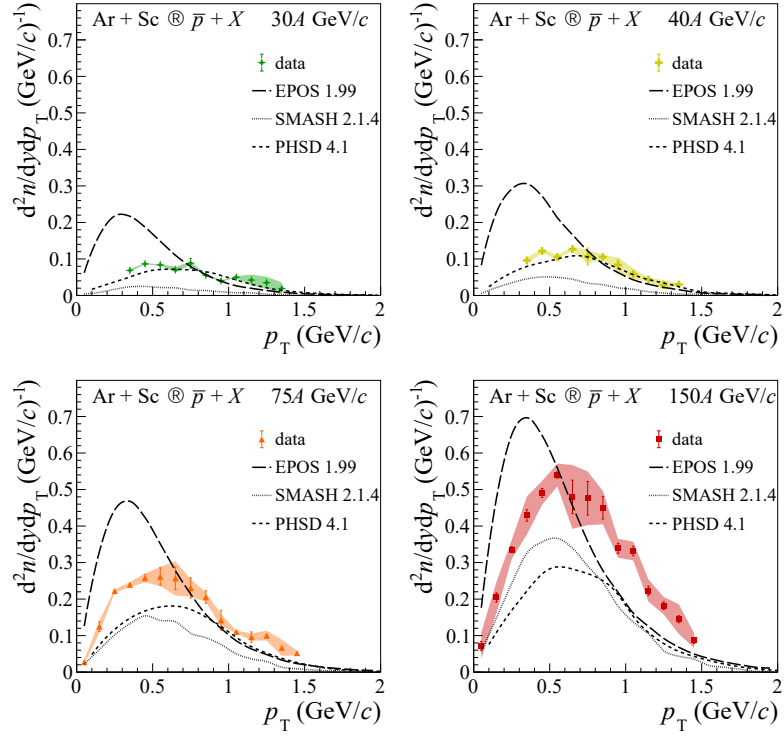
Figure 54: Transverse momentum distributions of antiprotons at mid-rapidity produced in 10% most *central* Ar+Sc interactions at 13*A*, 19*A*, 30*A*, 40*A*, 75*A* and 150*A* GeV/c compared with models: EPOS 1.99 [73], PHSD 4.1 [20, 21] and SMASH 2.1.4 [74, 75].

approach is no longer valid — in both PHSD and SMASH, the string approach is replaced with the creation of resonances and their decay. Additionally, the PHSD also features a chiral symmetry restoration with increasing energy followed by the creation of the QGP. The best overall agreement with the data is observed in the case of PHSD.
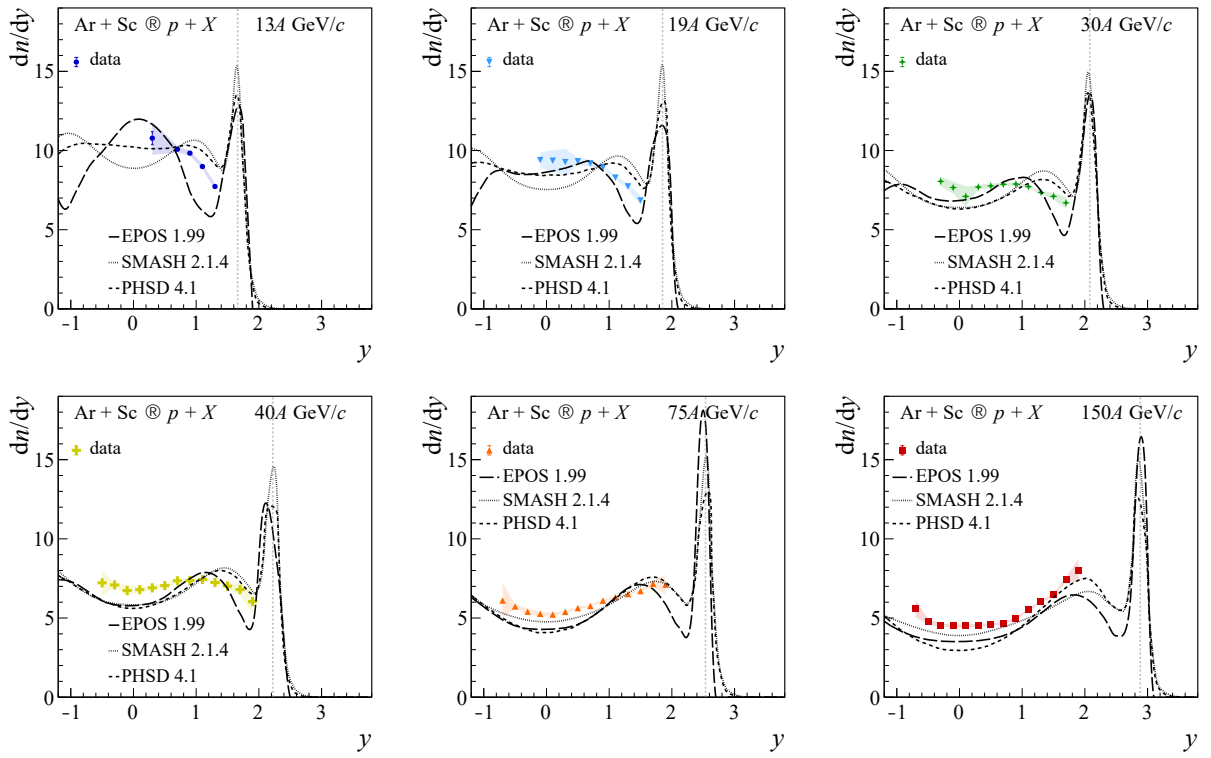
Figure 55: Rapidity spectra of protons produced in 10% most *central* Ar+Sc interactions at 13*A*, 19*A*, 30*A*, 40*A*, 75*A* and 150*A* GeV/*c* in comparison with models: EPOS 1.99 [73], PHSD 4.1 [20, 21] and SMASH 2.1.4 [74, 75].
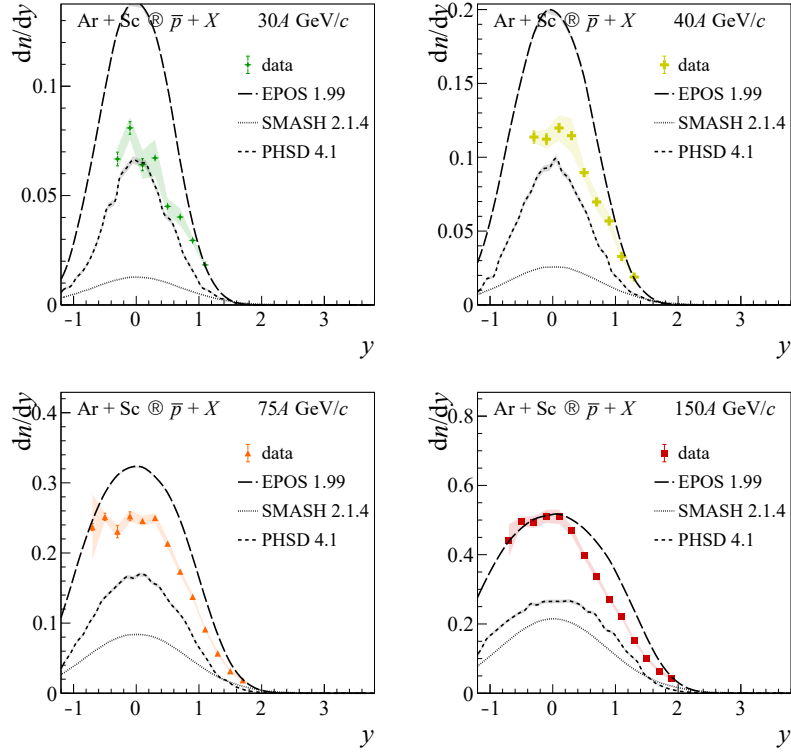
Figure 56: Rapidity spectra of antiprotons produced in 10% most *central* Ar+Sc interactions at 13*A*, 19*A*, 30*A*, 40*A*, 75*A* and 150*A* GeV/*c* in comparison with models: EPOS 1.99 [73], PHSD 4.1 [20, 21] and SMASH 2.1.4 [74, 75].
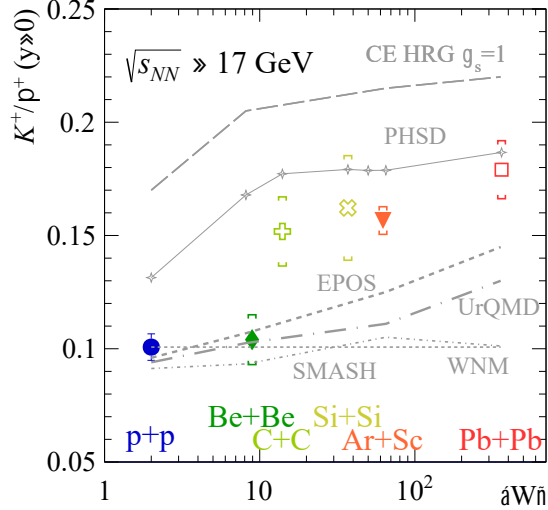
Figure 57: System size dependence of the K^+/π^+ ratio (at $y \approx 0$) in *central* nucleus-nucleus and inelastic *p+p* interactions obtained at beam momenta of 150*A* GeV/*c* ($\sqrt{s_{NN}} \approx 17$ GeV) compared with dynamical (EPOS 1.99 [73], PHSD 4.1 [20, 21] and UrQMD [78, 79]) and statistical (HRG [19]) models.

60

6 Summary and conclusions

This paper reports measurements by the NA61/SHINE experiment at the CERN SPS of spectra and mean multiplicities of $\pi^\pm, K^\pm, p$ and $\bar{p}$ produced in the 10% most central Ar+Sc collisions at beam momenta of 13A, 19A, 30A, 40A, 75A and 150A GeV/c. This is an intermediate-size nucleus-nucleus system investigated in the system size scan of NA61/SHINE. In this program, data were also recorded for p+p, Be+Be, Xe+La and Pb+Pb collisions. While the analysis for the two largest systems is still ongoing, an emerging system size dependence already shows interesting features.

Ar+Sc system appears to be the smallest for which a significant enhancement of the K^+/π^+ ratio with respect to p+p collisions is observed. Similarly, the measured charged-kaon transverse momentum spectra are characterized by significantly larger values of the inverse slope parameter (T) than in the case of small systems (p+p, Be+Be). The similarity between intermediate and heavy systems becomes more evident towards higher collision energies. At the same time, the measurements presented in this article show no indications of a horn structure at SPS energies for intermediate-size collision systems in contrast to the results from central Pb+Pb interactions.

The third property that distincts the Ar+Sc system from the small systems is the qualitatively different shape of the proton rapidity spectra. Similarly as in the collisions of Pb+Pb, the spectra measured in Ar+Sc reaction at 19A GeV/c are characterized by a convex shape near midrapidity, in contrast to the concave structure present for p+p and Be+Be systems.

The experimental results were compared with predictions of the models: EPOS 1.99, PHSD, and SMASH. None of the models reproduces all features of the presented results. We also highlight the failure of analyzed models in the description of the K^+/π^+ ratio in terms of both collision energy and system size dependence.

Acknowledgments

References

[1] N. Antoniou *et al.*, [NA61/SHINE Collab.], "Study of hadron production in hadron nucleus and nucleus nucleus collisions at the CERN SPS," tech. rep., CERN, 2006. CERN-SPSC-2006-034.

[2] S. Afanasiev *et al.*, [NA49 Collab.], "Energy dependence of pion and kaon production in central Pb + Pb collisions," *Phys. Rev.* **C66** (2002) 054902.

[3] C. Alt *et al.*, [NA49 Collab.], "Pion and kaon production in central Pb + Pb collisions at 20-A and 30-A-GeV: Evidence for the onset of deconfinement," *Phys. Rev.* **C77** (2008) 024903.

[4] L. Adamczyk *et al.*, "Bulk Properties of the Medium Produced in Relativistic Heavy-Ion Collisions from the Beam Energy Scan Program," *Phys.Rev.* **C96** (2017) 044904, `arXiv:1701.07065 [nucl-ex]`.

[5] A. Rustamov, "The Horn, Kink and Step, Dale: from few GeV to few TeV," *Central Eur.J.Phys.* **10** (2012) 1267–1270, `arXiv:1201.4520 [nucl-ex]`.

[6] F. Becattini, J. Manninen, and M. Gazdzicki, "Energy and system size dependence of chemical freeze-out in relativistic nuclear collisions," *Phys.Rev.* **C73** (2006) 044905, `arXiv:hep-ph/0511092 [hep-ph]`.

[7] C. Alt *et al.*, [NA49 Collab.], "Bose-Einstein correlations of pi-pi- pairs in central Pb+Pb collisions at A-20, A-30, A-40, A-80, and A-158 GeV," *Phys. Rev. C* **77** (2008) 064908, `arXiv:0709.4507 [nucl-ex]`.

[8] M. Gazdzicki, M. Gorenstein, and P. Seyboth, "Recent Developments in the Study of Deconfinement in Nucleus-Nucleus Collisions," *Int.J.Mod.Phys.* **E23** (2014) 1430008, `arXiv:1404.3567 [nucl-ex]`.

[9] V. Vovchenko, V. V. Begun, and M. I. Gorenstein, "Hadron multiplicities and chemical freeze-out conditions in proton-proton and nucleus-nucleus collisions," *Phys. Rev. C* **93** no. 6, (2016) 064906, `arXiv:1512.08025 [nucl-th]`.

[10] A. Aduszkiewicz, [NA61/SHINE Collab.], "Beam momentum scan with Pb+Pb collisions," Tech. Rep. CERN-SPSC-2015-038. SPSC-P-330-ADD-8, CERN, Geneva, Oct, 2015. `https://cds.cern.ch/record/2059811`.

[11] M. Gazdzicki and S. Kowalski, [NA61/SHINE Collaboration Collab.], "Open Charm Measurements: Pb-beam schedule and detector upgrade ," tech. rep., CERN, Geneva, Jan, 2022. `https://cds.cern.ch/record/2799311`.

[12] N. Abgrall *et al.*, [NA61/SHINE Collab.], "Measurement of negatively charged pion spectra in inelastic p+p interactions at p_{lab} = 20, 31, 40, 80 and 158 GeV/c," *Eur.Phys.J.* **C74** (2014) 2794, `arXiv:1310.2417 [hep-ex]`.

[13] A. Aduszkiewicz *et al.*, [NA61/SHINE Collab.], "Measurements of $\pi^{\pm}$, $K^{\pm}$, p and $\bar{p}$ spectra in proton-proton interactions at 20, 31, 40, 80 and 158 GeV/c with the NA61/SHINE spectrometer at the CERN SPS," *Eur. Phys. J.* **C77** no. 10, (2017) 671, `arXiv:1705.02467 [nucl-ex]`.

[14] A. Aduszkiewicz *et al.*, [NA61/SHINE Collab.], "Proton-Proton Interactions and Onset of Deconfinement," *Phys. Rev. C* **102** (2020) 011901, `arXiv:1912.10871 [hep-ex]`.

[15] A. Acharya *et al.*, [NA61/SHINE Collab.], "Measurements of π^- production in ^{7}Be+^{9}Be collisions at beam momenta from 19A to 150AGeV/c in the NA61/SHINE experiment at the CERN SPS," *Eur. Phys. J. C* **80** no. 10, (2020) 961, `arXiv:2008.06277 [nucl-ex]`. [Erratum: Eur.Phys.J.C 81, 144 (2021)].

[16] A. Acharya *et al.*, [NA61/SHINE Collab.], "Measurements of $\pi^{\pm}$, $K^{\pm}$, p and $\bar{p}$ spectra in ^{7}Be+^{9}Be collisions at beam momenta from 19A to 150A GeV/c with the NA61/SHINE spectrometer at the CERN SPS," *Eur. Phys. J. C* **81** no. 1, (2021) 73, `arXiv:2010.01864 [hep-ex]`.

[17] A. Acharya *et al.*, [NA61/SHINE Collab.], "Spectra and mean multiplicities of π^- in central^{40}Ar+^{45}Sc collisions at 13A, 19A, 30A, 40A, 75A and 150A Ge V /c beam momenta measured by the NA61/SHINE spectrometer at the CERN SPS," *Eur. Phys. J. C* **81** no. 5, (2021) 397, `arXiv:2101.08494 [hep-ex]`.

[18] R. Poberezhnyuk, M. Gazdzicki, and M. Gorenstein, "Statistical Model of the Early Stage of nucleus-nucleus collisions with exact strangeness conservation," *Acta Phys. Polon. B* **46** no. 10, (2015) 1991, `arXiv:1502.05650 [nucl-th]`.

[19] A. Motornenko, V. Begun, V. Vovchenko, M. Gorenstein, and H. Stoecker, "Hadron yields and fluctuations at energies available at the CERN Super Proton Synchrotron: System-size dependence from Pb + Pb to $p+p$ collisions," *Phys. Rev. C* **99** no. 3, (2019) 034909, `arXiv:1811.10645 [nucl-th]`.

[20] W. Cassing and E. L. Bratkovskaya, "Parton transport and hadronization from the dynamical quasiparticle point of view," *Phys. Rev. C* **78** (Sep, 2008) 034919. `https://link.aps.org/doi/10.1103/PhysRevC.78.034919`.

[21] W. Cassing and E. Bratkovskaya, "Parton–hadron–string dynamics: An off-shell transport approach for relativistic energies," *Nuclear Physics A* **831** no. 3, (2009) 215 – 242. `http://www.sciencedirect.com/science/article/pii/S0375947409005995`.

[22] N. Abgrall *et al.*, [NA61 Collab.], "NA61/SHINE facility at the CERN SPS: beams and detector system," *JINST* **9** (2014) P06005, `arXiv:1401.4699 [physics.ins-det]`.

[23] D. Banas, A. Kubala-Kukus, M. Rybczynski, I. Stabrawa, and G. Stefanek, "Influence of target material impurities on physical results in relativistic heavy-ion collisions," *Eur. Phys. J. Plus* **134** no. 1, (2019) 44, `arXiv:1808.10377 [nucl-ex]`.

[24] K. Werner, F.-M. Liu, and T. Pierog, "Parton ladder splitting and the rapidity dependence of transverse momentum spectra in deuteron-gold collisions at RHIC," *Phys.Rev.* **C74** (2006) 044902.

[25] C. F. Brun R., "Geant detector description and simulation tool, cern program library long writeup w5013," 1993. `http://wwwasdoc.web.cern.ch/wwwasdoc/geant/geantall.html`.

[26] A. Acharya *et al.*, [NA61/SHINE Collab.], "Measurements of π^- production in ^{7}Be+^{9}Be collisions at beam momenta from 19A to 150AGeV/c in the NA61/SHINE experiment at the CERN SPS," `arXiv:2008.06277 [nucl-ex]`.

[27] E. Kaptur, [NA61/SHINE Collab.], "PHD thesis: Analysis of collision centrality and negative pion spectra in ^{7}Be+^{9}Be interactions at CERN SPS energy range," 2017. `https://edms.cern.ch/document/2004086/1`.

[28] A. Seryakov, [NA61/SHINE Collab.], "PSD acceptance maps for event selection." `https://edms.cern.ch/document/1867336/1`, 2017. CERN EDMS.

[29] A. Bialas, M. Bleszynski, and W. Czyz, "Multiplicity Distributions in Nucleus-Nucleus Collisions at High-Energies," *Nucl. Phys.* **B111** (1976) 461.

[30] T. Pierog, R. Ulrich, and private communication, "EPOS 1.99 version CRMC." See `https://web.ikp.kit.edu/rulrich/crmc/html`, 2018.

[31] T. Pierog and K. Werner, "EPOS Model and Ultra High Energy Cosmic Rays," *Nucl. Phys. B Proc. Suppl.* **196** (2009) 102–105, `arXiv:0905.1198 [hep-ph]`.

[32] T. Anticic *et al.*, [NA49 Collab.], "Antideuteron and deuteron production in mid-central Pb+Pb collisions at 158A GeV," *Phys. Rev.* **C85** (2012) 044913, `arXiv:1111.2588 [nucl-ex]`.

[33] P. Podlaski, [NA61/SHINE Collab.], "PHD thesis: Study of charged hadron production with tof-dE/dx identification method in central Ar+Sc collisions in NA61/SHINE experiment at CERN." 2022. `https://cds.cern.ch/record/2799198`.

[34] M. van Leeuwen, [NA49 Collab.], "Energy dependence of particle production in nucleus nucleus collisions at the CERN SPS," in *Proceedings, 38th Rencontres de Moriond on QCD and High-Energy Hadronic Interactions.* 2003. `arXiv:nucl-ex/0306004 [nucl-ex]`.

[35] M. van Leeuwen, "A practical guide to de/dx analysis in na49," 2008.

[36] M. P. Lewicki, [NA61/SHINE Collab.], "Charged hadron production in central Ar+Sc collisions at the CERN SPS." 2020. `https://cds.cern.ch/record/2772291`.

[37] K. A. Olive *et al.*, [Particle Data Group Collab.], "Review of Particle Physics," *Chin. Phys.* **C38** (2014) 090001.

[38] A. Rustamov and M. Gorenstein, "Identity Method for Moments of Multiplicity Distribution," *Phys.Rev.* **C86** (2012) 044906, `arXiv:1204.6632 [nucl-th]`.

[39] C. Blume, M. Gazdzicki, B. Lungwitz, M. Mitrovski, P. Seyboth, and H. Ströbele, [NA49 Collab.], "Compilation of NA49 numerical results," 2013. `https://edms.cern.ch/document/1075059/4`.

[40] M. Van Leeuwen, "Kaon en open charm productie in centrale lood-lood botsingen aan het SPS te CERN," 2003. `http://cds.cern.ch/record/624231`. Presented on 19 May 2003.

[41] E. Schnedermann, J. Sollfrank, and U. W. Heinz, "Thermal phenomenology of hadrons from 200-A/GeV S+S collisions," *Phys.Rev.* **C48** (1993) 2462–2475, `arXiv:nucl-th/9307020 [nucl-th]`.

[42] M. Gazdzicki and O. Hansen, "Hadron production in nucleon-nucleon collisions at 200-GeV/c: A Compilation," *Nucl.Phys.* **A528** (1991) 754–770.

[43] F. Siklér *et al.*, [NA49 Collab.], "Hadron production in nuclear collisions from the NA49 experiment at 158-GeV/c/A," *Nucl. Phys. A* **661** (1999) 45–54.

[44] F. Verbeure *et al.*, [LEBC-EHS Collab.], "Inclusive production of particles and resonances in p p interactions at 400-GeV/c," *Sov. J. Nucl. Phys.* **54** (1991) 585–611.

[45] A. M. Rossi, G. Vannini, A. Bussiere, E. Albini, D. D'Alessandro, and G. Giacomelli, "Experimental Study of the Energy Dependence in Proton Proton Inclusive Reactions," *Nucl. Phys. B* **84** (1975) 269–305.

[46] A. I. Golokhvastov, "Koba-Nielsen-Olesen scaling in isospin-coupled reactions," *Phys. Atom. Nucl.* **64** (2001) 1841–1855.

[47] F. Becattini and U. W. Heinz, "Thermal hadron production in p p and p anti-p collisions," *Z. Phys. C* **76** (1997) 269–286, `arXiv:hep-ph/9702274`. [Erratum: Z.Phys.C 76, 578 (1997)].

[48] B. B. Back *et al.*, [PHOBOS Collab.], "Comparison of the total charged particle multiplicity in high-energy heavy ion collisions with e+ e- and p p / anti-p p data," `arXiv:nucl-ex/0301017`.

[49] V. Blobel, H. Fesefeldt, P. Freund, D. Gall, K. von Holt, U. Idschok, D. Luers, W. Schrankel, and B. M. Schwarzschild, [Bonn-Hamburg-Munich Collab.], "Higher Moments of the Pion Multiplicity Distribution in Proton Proton Interactions at 12-GeV/c and 24-GeV/c," *Nucl. Phys. B* **103** (1976) 221–233.

[50] M. Aguilar-Benitez *et al.*, "Inclusive particle production in 400-GeV/c p p interactions," *Z. Phys. C* **50** (1991) 405–426.

[51] A. C. Melissinos, T. Yamanouchi, G. G. Fazio, S. J. Lindenbaum, and L. C. L. Yuan, "pi-Meson Production in 2.9-BeV p-p Collisions," *Phys. Rev.* **128** (1962) 2373–2381.

[52] G. Alexander, O. Benary, G. Czapek, B. Haber, N. Kidron, B. Reuter, A. Shapira, E. Simopoulou, and G. Yekutieli, "Proton-Proton Interactions at 5.5 GeV/c," *Phys. Rev.* **154** (1967) 1284–1304.

[53] H. J. Mueck *et al.*, "Pionization in p p interactions at 12 and 24 gev/c," *Phys. Lett. B* **39** (1972) 303–306.

[54] C. W. Akerlof, D. G. Crabb, J. L. Day, N. P. Johnson, P. Kalbaci, A. D. Krisch, M. T. Lin, M. L. Marshak, J. K. Randolph, P. Schmueser, A. L. Read, K. W. Edwards, J. G. Asbury, G. J. Marmer, and L. G. Ratner, "Inelastic high-energy proton-proton collisions," *Phys. Rev. D* **3** (Feb, 1971) 645–663. `https://link.aps.org/doi/10.1103/PhysRevD.3.645`.

[55] M. Antinucci, A. Bertin, P. Capiluppi, M. D'Agostino-Bruno, A. M. Rossi, G. Vannini, G. Giacomelli, and A. Bussiere, "Multiplicities of charged particles up to ISR energies," *Lett. Nuovo Cim.* **6** (1973) 121–128.

[56] V. V. Ammosov *et al.*, [French-Soviet Collab.], "pi+- Meson and Proton Production in Inclusive and Semiinclusive Processes in p p Interactions at 69-GeV/c. 2.," *Nuovo Cim. A* **40** (1977) 237.

[57] T. Anticic *et al.*, [NA49 Collab.], "System-size and centrality dependence of charged kaon and pion production in nucleus-nucleus collisions at 40A GeV and158A GeV beam energy," *Phys. Rev.* **C86** (2012) 054903.

[58] B. Abelev *et al.*, [ALICE Collab.], "Pion, Kaon, and Proton Production in Central Pb–Pb Collisions at $\sqrt{s_{NN}} = 2.76$ TeV," *Phys. Rev. Lett.* **109** (2012) 252301, `arXiv:1208.1974 [hep-ex]`.

[59] B. B. Abelev *et al.*, [ALICE Collab.], "Production of charged pions, kaons and protons at large transverse momenta in pp and Pb–Pb collisions at $\sqrt{s_{NN}}$ =2.76 TeV," *Phys. Lett. B* **736** (2014) 196–207, `arXiv:1401.1250 [nucl-ex]`.

[60] J. Adams *et al.*, [STAR Collab.], "Identified particle distributions in pp and Au+Au collisions at s(NN)**(1/2) = 200 GeV," *Phys. Rev. Lett.* **92** (2004) 112301.

[61] K. Adcox *et al.*, [PHENIX Collab.], "Single identified hadron spectra from s(NN)**(1/2) = 130-GeV Au+Au collisions," *Phys. Rev.* **C69** (2004) 024904.

[62] S. Adler *et al.*, [PHENIX Collab.], "Identified charged particle spectra and yields in Au+Au collisions at S(NN)**1/2 = 200-GeV," *Phys.Rev.* **C69** (2004) 034909.

[63] I. Arsene *et al.*, [BRAHMS Collab.], "Centrality dependent particle production at y=0 and y ~ 1 in Au + Au collisions at s(NN)**(1/2) = 200-GeV," *Phys. Rev. C* **72** (2005) 014908, `arXiv:nucl-ex/0503010`.

[64] L. Ahle *et al.*, [E-802, E-866 Collab.], "Centrality dependence of kaon yields in Si + A and Au + Au collisions at the AGS," *Phys. Rev. C* **60** (1999) 044904, `arXiv:nucl-ex/9903009`.

[65] H. Schuldes, [HADES Collab.], "Strangeness production in Au(1.23 A GeV)+Au collisions," *Nucl. Phys. A* **967** (2017) 804–807.

[66] B. I. Abelev *et al.*, [STAR Collab.], "Systematic Measurements of Identified Particle Spectra in pp, d^+ Au and Au+Au Collisions from STAR," *Phys. Rev. C* **79** (2009) 034909, `arXiv:0808.2041 [nucl-ex]`.

[67] M. Kliemant, B. Lungwitz, and M. Gazdzicki, "Energy dependence of transverse mass spectra of kaons produced in p + p and p + anti-p interactions: A Compilation," *Phys.Rev.* **C69** (2004) 044903, `arXiv:hep-ex/0308002 [hep-ex]`.

[68] K. Aamodt *et al.*, [ALICE Collab.], "Production of pions, kaons and protons in pp collisions at $\sqrt{s} = 900$ GeV with ALICE at the LHC," *Eur. Phys. J. C* **71** (2011) 1655, `arXiv:1101.4110 [hep-ex]`.

[69] M. Gazdzicki and M. I. Gorenstein, "On the early stage of nucleus-nucleus collisions," *Acta Phys.Polon.* **B30** (1999) 2705, `arXiv:hep-ph/9803462 [hep-ph]`.

[70] W. Busza and A. S. Goldhaber, "NUCLEAR STOPPING POWER," *Phys. Lett. B* **139** (1984) 235.

[71] M. Gazdzicki and A. Rybicki, [NA61/SHINE Collab.], "Overview of Results from NA61/SHINE: Uncovering Critical Structures," *Acta Phys. Polon. B* **50** (2019) 1057–1070.

[72] E. Andronov, M. Kuich, and M. Gaździcki, "Diagram of High-Energy Nuclear Collisions," *Universe* **9** no. 2, (2023) 106.

[73] K. Werner, "The hadronic interaction model EPOS," *Nucl. Phys. Proc. Suppl.* **175-176** (2008) 81–87.

[74] J. Mohs, S. Ryu, and H. Elfner, "Particle Production via Strings and Baryon Stopping within a Hadronic Transport Approach," *J. Phys. G* **47** no. 6, (2020) 065101, `arXiv:1909.05586 [nucl-th]`.

[75] J. Weil, V. Steinberg, J. Staudenmaier, L. G. Pang, D. Oliinychenko, J. Mohs, M. Kretz, T. Kehrenberg, A. Goldschmidt, B. Bäuchle, J. Auvinen, M. Attems, and H. Petersen, "Particle production and equilibrium properties within a new hadron transport approach for heavy-ion collisions," *Phys. Rev. C* **94** (Nov, 2016) 054905. https://link.aps.org/doi/10.1103/PhysRevC.94.054905.

[76] T. Anticic *et al.*, [NA49 Collab.], "Inclusive production of protons, anti-protons and neutrons in p+p collisions at 158-GeV/c beam momentum," *Eur. Phys. J. C* **65** (2010) 9–63, `arXiv:0904.2708 [hep-ex]`.

[77] Y. B. Ivanov and D. Blaschke, "Baryon stopping in heavy-ion collisions at $E_{lab} = 2A$-200A GeV," *Eur. Phys. J. A* **52** no. 8, (2016) 237.

[78] S. Bass *et al.*, "Microscopic models for ultrarelativistic heavy ion collisions," *Prog.Part.Nucl.Phys.* **41** (1998) 255–369, `arXiv:nucl-th/9803035 [nucl-th]`.

[79] M. Bleicher *et al.*, "Relativistic hadron hadron collisions in the ultrarelativistic quantum molecular dynamics model," *J.Phys.* **G25** (1999) 1859–1896, `arXiv:hep-ph/9909407 [hep-ph]`.